US Army Corps
of Engineers

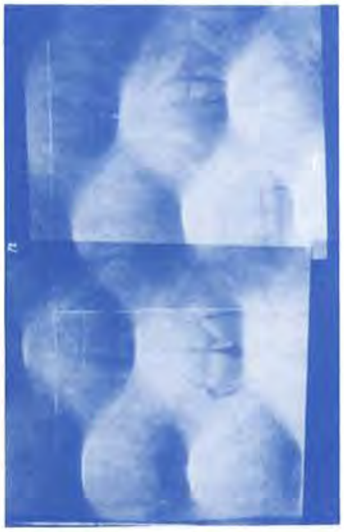

MISCELLANEOUS PAPER CERC-88-4

STABLE THREE-DIMENSIONAL BIPERIODIC WAVES IN SHALLOW WATER

by

Norman W. Scheffner

Coastal Engineering Research Center

DEPARTMENT OF THE ARMY
Waterways Experiment Station, Corps of Engineers
PO Box 631, Vicksburg, Mississippi 39180-0631

February 1988
Final Report

Approved For Public Release; Distribution Unlimited

Prepared for DEPARTMENT OF THE ARMY
Assistant Secretary of the Army (R&D)
Washington, DC 20315-1000

Unclassified
SECURITY CLASSIFICATION OF THIS PAGE

REPORT DOCUMENTATION PAGE

Form Approved
OMB No 0704-0188
Exp. Date Jun 30, 1986

1a. REPORT SECURITY CLASSIFICATION
Unclassified

1b. RESTRICTIVE MARKINGS

2a. SECURITY CLASSIFICATION AUTHORITY

2b. DECLASSIFICATION / DOWNGRADING SCHEDULE

3. DISTRIBUTION / AVAILABILITY OF REPORT
Approved for public release; distribution unlimited.

4. PERFORMING ORGANIZATION REPORT NUMBER(S)
Miscellaneous Paper CERC-88-4

5. MONITORING ORGANIZATION REPORT NUMBER(S)

6a. NAME OF PERFORMING ORGANIZATION
USAEWES, Coastal Engineering Research Center

6b. OFFICE SYMBOL (*If applicable*)

7a. NAME OF MONITORING ORGANIZATION

6c. ADDRESS (*City, State, and ZIP Code*)
PO Box 631
Vicksburg, MS 39180-0631

7b. ADDRESS (*City, State, and ZIP Code*)

8a. NAME OF FUNDING / SPONSORING ORGANIZATION
See reverse.

8b. OFFICE SYMBOL (*If applicable*)

9. PROCUREMENT INSTRUMENT IDENTIFICATION NUMBER

8c. ADDRESS (*City, State, and ZIP Code*)
Washington, DC 20315-1000

10. SOURCE OF FUNDING NUMBERS

PROGRAM ELEMENT NO.	PROJECT NO.	TASK NO.	WORK UNIT ACCESSION NO

11. TITLE (*Include Security Classification*)
Stable Three-Dimensional Biperiodic Waves in Shallow Water

12. PERSONAL AUTHOR(S)
Scheffner, Norman W.

13a. TYPE OF REPORT
Final report

13b. TIME COVERED
FROM Jan 85 TO Sep 85

14. DATE OF REPORT (*Year, Month, Day*)
February 1988

15. PAGE COUNT
200

16. SUPPLEMENTARY NOTATION
Available from National Technical Information Service, 5285 Port Royal Road, Springfield, VA 22161.

17. COSATI CODES

FIELD	GROUP	SUB-GROUP

18. SUBJECT TERMS (*Continue on reverse if necessary and identify by block number*)
Kadomtsev-Petviashvili equation
Nonlinear
Water waves

19. ABSTRACT (*Continue on reverse if necessary and identify by block number*)

Waves in shallow water are inherently three-dimensional and nonlinear. Experiments are presented herein which demonstrate the existence of a new class of long water waves which are genuinely three-dimensional, nonlinear, and of (quasi-) permanent form. These waves are referred to as biperiodic in that they have two real periods, both temporal and spatial. The waves are produced in the laboratory by the simultaneous generation of two cnoidal wave trains which intersect at angles to one another. The resulting surface pattern is represented by a tiling of hexagonal patterns, each of which is bounded by wave crests of spatially variable amplitude. Experiments are conducted over a wide range of generation parameters in order to fully document the waves in the vertical and two horizontal directions. The hexagonal-shaped waves are remarkably robust, retaining their integrity for maximum wave heights up to and including breaking and for widely varying horizontal length scales.

(Continued)

20. DISTRIBUTION / AVAILABILITY OF ABSTRACT
☒ UNCLASSIFIED/UNLIMITED ☐ SAME AS RPT ☐ DTIC USERS

21. ABSTRACT SECURITY CLASSIFICATION
Unclassified

22a. NAME OF RESPONSIBLE INDIVIDUAL

22b. TELEPHONE (*Include Area Code*)

22c. OFFICE SYMBOL

DD FORM 1473, 84 MAR

83 APR edition may be used until exhausted.
All other editions are obsolete.

SECURITY CLASSIFICATION OF THIS PAGE
Unclassified

8a. NAME OF FUNDING/SPONSORING ORGANIZATION (Continued).

DEPARTMENT OF THE ARMY
Assistant Secretary of the Army (R&D)

19. ABSTRACT (Continued).

The Kadomtsev-Petviashvili (KP) equation is tested as a model for these biperiodic waves. This equation is the direct three-dimensional generalization of the famous Korteweg-deVries (KdV) equation for weakly nonlinear waves in two dimensions. It is known that the KP equation admits an infinite dimensional family of periodic solutions which are defined in terms of Riemann theta functions of genus N. Genus 2 solutions have two real periods and are similar in structure to the hexagonally shaped waves observed in the experiments. A methodology is developed which relates the free parameters of the genus 2 solution to the temporal and spatial data of the experimentally generated waves. Comparisons of exact genus 2 solutions with measured data show excellent agreement over the entire range of experiments. Even though near-breaking waves and highly three-dimensional wave forms are encountered, the total rms error between experiment and KP theory never exeeds 20 percent, although known sources of error are introduced. Hence, the KP equation appears to be a very robust model of nonlinear three-dimensional waves propagating in shallow water, reminiscent of the KdV equation in two dimensions.

PREFACE

The investigation described herein was authorized and funded by the Department of the Army through the In-House Laboratory Independent Research (ILIR) program offered at the US Army Engineer Waterways Experiment Station (CEWES). The work was performed at the Coastal Engineering Research Center (CERC) of CEWES.

The study was conducted during the period of 1 January 1985 through 30 September 1987 by Dr. Norman W. Scheffner of the Coastal Processes Branch, Research Division, CERC. This report essentially represents the dissertation of the same title submitted by Dr. Scheffner to the University of Florida in partial fulfillment of the requirements for the degree of Doctor of Philosophy in Engineering Mechanics. Dr. Joseph L. Hammack, University of Florida, served as committee chairman and dissertation advisor, and Dr. Harvey Segur, Aerospace Research Associates (ARAP), Princeton, N. J., provided the guidance necessary for the successful completion of this project. Additional support by Dr. Robert W. Whalin, Dr. James R. Houston, and Mr. H. Lee Butler of CEWES is acknowledged and appreciated by the author as essential to the completion of both the report and the degree. The study was conducted under general supervision of Dr. Houston, Chief, CERC; Mr. Butler, Chief, Research Division, CERC; and Dr. Steven A. Hughes, Chief, Coastal Processes Branch, Research Division, CERC.

In addition to the above individuals, the assistance and dedication of the following CEWES personnel is greatly appreciated by the author: Messrs. Larry A. Barnes, Michael J. Briggs, Kent A. Turner, and Ms. Mary L. (Dean) Hampton of the Wave Dynamics Division, CERC; Messrs. Lonnie L. Frier, Homer C. Greer III, and Barry W. McCleave of the Operations Branch, Instrumentation Services Division; and Mr. Charles E. Ray of the Photography Branch and Mrs. Jewell B. Rook of the Reports Branch, Information Products Division.

COL Dwayne G. Lee, CE, was Commander and Director and Dr. Whalin was Technical Director of CEWES during publication of this report.

ACKNOWLEDGEMENTS

The author wishes to gratefully acknowledge his committee chairman and advisor, Professor Joseph L. Hammack, for his guidance, assistance, and enthusiasm during the entirety of this project. Without this untiring dedication, the successful completion of this investigation would not have been possible. The following members of the author's supervisory committee are gratefully acknowledged for their advice and support: Professors Ashish J. Mehta, Robert G. Dean, Chen-Chi Hsu, Tom I-P. Shih, and Thomas T. Bowman. Professor James T. Kirby is also thanked for his comments on the final manuscript.

The writer would also like to thank Dr. Harvey Segur for his profound knowledge of the KP equation and his genuine interest in the success of this project. He not only provided the software used to compute and generate exact KP solutions graphically, but also provided invaluable assistance and guidance during the data analysis phase of the project. This assistance is greatly appreciated.

The author would especially like to thank those who assisted in the experimental phase of this investigation. This assistance and advice extended from the initial stages of attempting to generate waves through the collection and storage of data. Hardware malfunctions, software bugs, logistical difficulties, and other seemingly insurmountable problems were almost routinely overcome with the help of the following dedicated personnel of the US Army Engineer Waterways Experiment Station at

Vicksburg, Mississippi: Larry A. Barnes, Michael J. Briggs, Mary L. (Dean) Hampton, and Kent A. Turner of the Wave Processes Branch, Wave Dynamics Division, Coastal Engineering Research Center; Lonnie L. Frier, Homer C. Greer III, and Barry W. McCleave of the Operations Branch, Instrumentation Services Division; and Charles E. Ray of the Photography Branch, Information Products Division.

This research investigation was funded through a Department of the Army In-House Laboratory Independent Research (ILIR) program. The author would like to thank the Department of the Army and the members of the ILIR selection committee for funding this project.

Last, but certainly not least, I would like to thank Gail A. Bird for her continuous support of this educational endeavor.

TABLE OF CONTENTS

Page

LIST OF TABLES

LIST OF FIGURES

Abstract of Dissertation Presented to the
Graduate School of the University of Florida
in Partial Fulfillment of the Requirements
for the Degree of Doctor of Philosophy

STABLE, THREE-DIMENSIONAL, BIPERIODIC WAVES IN SHALLOW WATER

By

Norman Wahl Scheffner

May 1987

Chairman: Joseph L. Hammack, Jr.
Cochairman: Ashish J. Mehta
Major Department: Engineering Sciences

Waves in shallow water are inherently three-dimensional and nonlinear. Experiments are presented herein which demonstrate the existence of a new class of long water waves which are genuinely three-dimensional, nonlinear, and of (quasi-) permanent form. These waves are referred to as biperiodic in that they have two real periods, both temporally and spatially. The waves are produced in the laboratory by the simultaneous generation of two cnoidal wave trains which intersect at angles to one another. The resulting surface pattern is represented by a tiling of hexagonal patterns, each of which is bounded by wave crests of spatially variable amplitude. Experiments are conducted over a wide range of generation parameters in order to fully document the waves in the vertical and two horizontal directions. The hexagonal-shaped waves are remarkably robust, retaining their integrity for maximum wave heights up to and including breaking and for widely varying horizontal length scales.

The Kadomtsev-Petviashvili (KP) equation is tested as a model for these biperiodic waves. This equation is the direct three-dimensional generalization of the famous Korteweg-deVries (KdV) equation for weakly nonlinear waves in two dimensions. It is known that the KP equation admits an infinite dimensional family of periodic solutions which are defined in terms of Riemann theta functions of genus N. Genus 2 solutions have two real periods and are similar in structure to the hexagonally-shaped waves observed in the experiments. A methodology is developed which relates the free parameters of the genus 2 solution to the temporal and spatial data of the experimentally generated waves. Comparisons of exact genus 2 solutions with measured data show excellent agreement over the entire range of experiments. Even though near-breaking waves and highly three-dimensional wave forms are encountered, the total rms error between experiment and KP theory never exceeds 20% although known sources of error are introduced. Hence, the KP equation appears to be a very robust model of nonlinear, three-dimensional waves propagating in shallow water, reminiscent of the KdV equation in two dimensions.

CHAPTER 1

INTRODUCTION

The propagation of waves in shallow water is a phenomenon of significant practical importance. Shallow water waves are especially important to the field of coastal engineering where their effects on beaches, harbors, inlets, coastal structures, etc. are both economical and aesthetic concerns. The ability to model realistic wave characteristics such as their vertical height distribution, surface pattern, fluid velocities, and wave speed is essential for developing engineering solutions to problems in the coastal zone. Difficulties in making such predictions arise from the fact that the equations governing the physics of flow, i.e. the conservation laws of Newtonian physics and the appropriate boundary conditions, cannot be solved exactly. The inability to solve these equations in closed form is due to the nonlinear terms contained in the governing equations. In order to circumvent these difficulties, a variety of simplifying approximations is made. For example, the nonlinear terms are often neglected, giving rise to a linear wave theory. Both the omission of nonlinear terms and three-dimensionality are especially severe restrictions for nearshore problems and result in solutions which do not realistically model many situations.

Natural waves experience dramatic changes in their appearance as they propagate from deep water into shallow water regions. In the shallow areas, the waves become steep with high crests and long shallow troughs. This transformation in shape can be attributed primarily to the decrease in water depth. Additional boundary conditions, such as irregular shoreline features, nonuniform variations in bathymetry, and the presence of coastal structures result in the refraction, diffraction and reflection of the incident wave; hence, the resulting wave field is not only nonlinear in shape but also spatially three-dimensional. For wave fields which can be reasonably approximated in two dimensions, cnoidal wave theory, first published by Korteweg and deVries (KdV) in 1895, has been found to be descriptive of the nonlinear features observed in shallow water. The linear wave approximation, most commonly used for three-dimensional coastal engineering applications, assumes that the nonlinear terms in the governing equations are negligible. Unfortunately, this theory does not predict the nonlinear three-dimensional features which are often of importance in shallow water regions. Therefore, a realistic analytical model which describes both nonlinear and three-dimensional waves in shallow water is not available currently.

A recent advance in the theoretical description of three-dimensional, nonlinear waves in shallow water is presented by Segur and Finkel (SF, 1985). They present an explicit, analytical solution for three-dimensional, weakly nonlinear wave forms. These solutions are biperiodic in that the waves have two independent spatial and temporal periods. Biperiodic waves are an exact solution of the Kadomtsev-Petviashvili equation (KP, 1970) and represent a natural three-dimensional generalization of the two-dimensional cnoidal waves of the KdV equation.

The analytical solution of the KP equation described by Segur and Finkel represents a somewhat abstract mathematical formulation which has never been applied to actual wavefields. If, in fact, these solutions model nonlinear waves accurately, they will represent a significant advancement in the field of nonlinear wave mechanics and a powerful new tool for the coastal engineer. Herein are presented laboratory experiments which document the existence of a new class of long water waves which are truly three-dimensional, biperiodic and nonlinear. The experimentally generated waves are used to test the validity of the KP solutions presented by SF. In order to verify these solutions as a model for the experimental wave fields, the mathematical parameters of the exact solution first must be related to the physical characteristics of the waves measured in the laboratory. Secondly, an experimental program must be developed that provides a reasonably comprehensive test of KP theory. Additionally, parameter limits are sought in order to establish the stability and range of applicability of the biperiodic solutions.

An experimental test of the KP equation as a viable model for three-dimensional, periodic, and nonlinear waves requires the successful completion of several tasks. For example, even though the qualitative features of the surface pattern for biperiodic waves are documented by Segur and Finkel, procedures are not available which would provide a formal basis for applying KP theory to practical situations. Instead, SF present a series of conjectures which suggest a methodology for inferring the free mathematical parameters of the exact solution from certain physical measurements of an observed three-dimensional wave field. An initial task of this study is to utilize the conjectures of SF and develop a technique for calculating exact KP solutions from measured wave characteristics. Secondly, an experimental laboratory program is developed for generating three-dimensional waves (with two-dimensional surface patterns) which are qualitatively similar to those presented by Segur and Finkel. Following the generation of the proper wave patterns, a methodology is developed for measuring the spatial and temporal characteristics of the wave field necessary for determining the solution parameters. Finally, a comparison of measured data and best-fit theoretical solutions is made in order to establish the stability and range of validity of KP theory over a wide parameter range.

A brief review of two-dimensional nonlinear wave theory in shallow water is presented in Chapter 2 in order to provide a proper perspective for the extension of the theory into three dimensions. This chapter begins with a discussion of the first experimental documentation of permanent form shallow water waves by John Scott Russell in 1844. The formal derivation of the KP equation is presented in Chapter 3. The exact biperiodic solutions presented by Segur and Finkel (1985) are also described in this chapter. Chapter 4 describes the laboratory facilities and the experimental procedures developed in order to accomplish the goals of this study. The experimental procedures include the method used to generate three-dimensional wave patterns and the data acquisition techniques employed to quantify the resulting wave fields. A methodology for relating KP theory to wave measurements is presented in Chapter 5. This chapter includes an investigation of the parameters in the KP solution and their relationship to experimental wave characteristics. Conclusions of this study are presented in Chapter 6. A presentation of the elliptic functions used for the generation of waves in the laboratory is shown in Appendix A. All of the spatial and temporal data used in this study are presented in Appendix B.

CHAPTER 2

LITERATURE REVIEW

In the middle 1800s, a controversy arose as to whether or not a single, localized wave of elevation could propagate at constant velocity with permanent form, neither steepening nor dispersing. The argument was prompted by the observation in 1834 and subsequent laboratory verification in 1844 of a permanent-form wave by John Scott Russell. This wave has since been termed the "solitary wave" and, more recently, a "soliton." At that time, no known mathematical solutions for the equations of fluid motion existed which adequately described the solitary wave. Linear (inviscid) theory described a wave form which dispersed into sinusoidal spectral components because of the dependence of the computed phase speed on the wave length. Although these waves were of permanent form, they were not of the shape observed by Russell. The existing theory advocated by Airy did account for nonlinearity but did not account for dispersion of the wave. This theory described waves of elevation which steepened in time but did not disperse; i.e., they were not of permanent form and contradicted Russell's observations. Even though Russell meticulously documented the existence of the solitary wave, his findings were essentially ignored by Airy. In fact, a certain amount of contemptuousness and jealousy appears to have existed between the two scientists because in 1845, just one year after Russell's laboratory verification, Airy published a theory of long waves in which he specifically addressed the propagation of small-but-finite amplitude waves. Airy's interest in the subject was somewhat biased in that his wave theory did not admit permanent form solutions. His attitude was reflected in the published theory in which he concluded that solitary waves of permanent form, such as those reported by Russell, do not exist!

Fortunately, mathematicians and fluid mechanicians other than Airy were interested in the solitary wave which seemed to contradict all previously existing theories of fluid motion. Subsequently, intense efforts were directed at deriving an approximate governing equation which would successfully model the waves observed by Russell. During this time, several theories were advanced which explained the existence of solitary waves. Boussinesq in 1871 and, independently, Rayleigh in 1876 first derived theories which admitted solitary waves as solutions. The most concise mathematical treatment for the solitary wave was presented in 1895 by Korteweg and deVries. They derived an approximate evolution equation for a wave field which admits both solitary and periodic solutions. This remarkable equation is now known as the Korteweg-deVries (KdV) equation and has the form

$$f_{\hat{t}} + 6\, f f_{\hat{x}} + f_{\hat{x}\hat{x}\hat{x}} = 0 \; . \qquad 2.1$$

The KdV equation was derived as a model for the propagation of a wave which is both weakly nonlinear and weakly dispersive. In the nondimensionalized equation 2.1, f represents a suitably scaled wave amplitude, $\hat{t}$ is time and $\hat{x}$ is the direction of wave propagation. The periodic solutions of the KdV equation were termed "cnoidal waves" (in analogy with sinusoidal waves) by Korteweg and deVries. These periodic solutions can be written in the following form:

$$f(\hat{x},\hat{t}) = 2\sigma^2 m^2 \; \mathrm{cn}^2 \; (\gamma,m) - 2\sigma \left[\frac{E(m)}{K(m)} - 1 + m\right] \qquad 2.2$$

where cn is the Jacobian elliptic cosine function and γ is a phase argument (to be described at a later point). The functions $K(m)$ and $E(m)$ represent the complete elliptical integrals of the first and second kind. The argument m is the Jacobian elliptical parameter with a modulus of the form $0 \leq m \leq 1$. The amplitude parameter σ is the following function of the nondimensionalized wavelength λ :

$$\sigma = \frac{2K(m)}{\lambda} .$$

(A presentation of the complete cnoidal wave solution in an alternate, but equivalent, form of Equation 2.2 is made in Appendix A.) The above solution recovers sinusoidal waves as m approaches zero. As the wavelength becomes infinitely large, m approaches unity and the solitary wave solution is recovered with the form

$$f(\hat{x},\hat{t}) = \mathrm{sech}^2(\gamma) . \qquad 2.3$$

The specific point of interest here is that the exact periodic solution is written completely in terms of well-known analytic functions and can therefore be used for analyzing the characteristics of naturally occurring two-dimensional waves. The practical application of cnoidal wave theory was recognized by Wiegel (1960) who developed a set of figures which made the calculation of cnoidal wave solutions in terms of measurable wave quantities an easy task. This development was a significant contribution to the field of coastal and oceanographic engineering since it provided design engineers with the first usable two-dimensional, nonlinear, shallow water wave model. Until this time, linear wave theory was used primarily for the majority of coastal applications, regardless of its applicability to the problem. Even though cnoidal wave theory is only two-dimensional, descriptive of one-dimensional or long-crested waves, a marked improvement over linear solutions was made possible for the practicing engineer.

The development of an adequate understanding of solitary (aperiodic) and cnoidal (periodic) waves required about 50 years, extending from Russell's observations to the publication of KdV theory. The explanation given by KdV for the existence of the soliton wave was then apparently overlooked by most subsequent researchers. This lack of understanding is evidenced in the literature as manifest by the references to the "long wave paradox" which questions the theoretical basis for the propagation of a nonlinear wave that neither steepens nor disperses. Ursell (1953), apparently unaware of the results of Korteweg and deVries, provided a clear explanation of this paradox in terms of the parameter (now referred to as the Ursell parameter),

$$U = \frac{aL^2}{h^3} . \qquad 2.4$$

In equation 2.4, a is a dimensional measure of wave amplitude, L is the dimensional wavelength, and h is the depth of water. Ursell demonstrated that this parameter represented a ratio of weakly nonlinear effects (measured by a/h) to weakly dispersive effects (measured by h^2/L^2) which can be used to distinguish between flow regimes. Interpretive examples of the relative magnitude of this parameter are common. For example, when the wave in question has a Ursell parameter of order unity, $U = O(1)$, then the effects of nonlinearity and dispersion are comparable and a balance is possible between the two effects. A permanent form wave can result when these weak effects are balanced. When the parameter is small, $U << 1$, nonlinearity is negligible and the waves are essentially linear. The wave then disperses into sinusoidal components, each of which is a permanent-form solution of linear theory. When the parameter becomes large, $U >> 1$, the governing equation is of the type advocated by Airy (1845) which does not admit permanent form solutions. These nonlinear waves experience steepening and stretching due to the effect of the wave amplitude on the wave speed. (This effect is known as amplitude dispersion.) Since the Ursell parameter does successfully predict the flow regime for a wave with given dimensions, it is commonly used in engineering practice.

It is interesting to note that Ursell was not the first to use the parameter of Equation 2.4. In fact, the first reference to the Ursell parameter was much earlier in a paper by Stokes (1847). Stokes demonstrated that a second-order, permanent-form solution could be derived for the fluid motion if an approximation method was used in which this parameter is taken to be small. Unfortunately, Stokes apparently did not recognize the significance of his observation for explaining that the existence of a permanent-form nonlinear wave in shallow water was due to the balance of opposing steepening and dispersion effects. For example, in the same paper, he agreed with Airy's conclusion by making the statement that "a solitary wave can not be propagated." Although Stokes later recognized that this conclusion was erroneous, he never again referred to the parameter. The next reference to the Ursell parameter was made by Korteweg and deVries (1895) who demonstrated that their cnoidal wave solutions reduced to Stokes' second-order solution when the elliptic modulus became small. Furthermore, KdV related the elliptic modulus of their solution to the Ursell parameter and showed that a correspondingly small value resulted in a sinusoidal solution. This differentiation between wave regimes; i.e., cnoidal or sinusoidal, based on the relative size of the Ursell parameter demonstrated that Korteweg and deVries were certainly cognizant of the impact of the parameter on the resulting wave solution.

Following the introduction of the KdV equation with its solitary and cnoidal solutions, no new applications appear to have been reported until 1960, at which time the equation re-emerged in a study of collision-free hydromagnetic waves (Gardner and Morikawa, 1960). Related studies by Kruskal and Zabusky (1963) again resulted in the derivation of the equation. It was in this new research context that physicists and mathematicians began to discover applications of the KdV equation which would significantly impact the scientific community. These discoveries led to the formulation and development of the Inverse Scattering Transform (IST) by Gardner, Green, Kruskal and Miura (1967).

Their landmark paper outlined a revolutionary solution technique which can be used to predict the exact number of solitary waves, or "solitons," which emerge from arbitrary aperiodic initial conditions. In fact, solutions that describe any finite number of interaction solitons can also be expressed in closed form.

The significance of the IST was far more profound than was initially realized. Zakharov and Shabat (1972), using a technique introduced by Lax (1968), demonstrated that the IST provided an exact solution for the nonlinear Schrödinger equation, which describes nonlinear waves in deep water. Their work demonstrated that the solution technique was not an accident which was only applicable to the KdV equation. Soon, many physically significant nonlinear partial differential equations (PDEs) were found to be solvable by the IST, firmly demonstrating the power and versatility of the solution technique. Ablowitz, Kaup, Newell, and Segur (1973,1974) extended the applicability of the transform by employing Lax's (1968) approach to develop criteria which made it possible to derive equations which could be solved by the IST. An enormous amount of theoretical interest had been generated by the introduction of the transform, so much so, that specialized research applications were beginning to emerge. One area of particular importance to the study herein relates to the case of periodic boundary conditions and solutions.

An important contribution to the theory of nonlinear equations with periodic boundary conditions was made by McKean and van Moerbeke (1975) and Marchenko (1977). Their work established a connection between the spectral theory of operators with periodic coefficients and algebraic geometry, the theory of finite-dimensional completely integrable

Hamiltonian systems and the theory of nonlinear equations of the KdV type (Dubrovin, 1981). They showed that the KdV equation admitted an infinitely dimensional family of solutions which could be written in terms of Riemann theta functions of the form

$$f(\hat{x},\hat{t}) = 2 \frac{\partial^2}{\partial \hat{x}^2} \ln \theta(\psi_1, \psi_2, \ldots, \psi_N; B) \qquad 2.5$$

where θ is a theta function of genus N. The theta function contains N one-dimensional (in the horizontal plane) phase variables and a scalar parameter B. They showed that the genus 1 solution was equivalent to the cnoidal solution shown in Equation 2.2 and was the only permanent form solution of the KdV equation.

The generalization and extension of this theory to three-dimensional systems was made by Krichever (1976). He developed a methodology for solving the three-dimensional generalization of the KdV equation, the Kadomtsev-Petviashvili (KP) equation. This equation, which was first proposed by KP (1970) and is formally derived in Chapter 3, can be written in the scaled form:

$$(f_{\hat{t}} + 6ff_{\hat{x}} + f_{\hat{x}\hat{x}\hat{x}})_{\hat{x}} + 3f_{\hat{y}\hat{y}} = 0 \qquad 2.6$$

where $(\hat{x},\hat{y})$ are orthogonal coordinates in the plane of the quiescent water surface with $\hat{x}$ representing the primary direction of wave propagation. The equation is based on the assumptions of weak nonlinearity and weak dispersion, as in the derivation of the KdV equation, and on weak three-dimensionality. Each effect is assumed to be of an equal order of magnitude. The previous statement that the KP equation is a direct three-dimensional generalization of the KdV equation can be seen. The equation reverts to the KdV equation when no crest-wise or variations in the $\hat{y}$-direction occur.

Krichever (1976) showed that the KP equation admits an infinitely dimensional family of exact periodic (or quasi-periodic) solutions. The concepts employed by Krichever in his solution methodology were adapted and further extended by Dubrovin (1981) in order to express these periodic solutions in the following form:

$$f(\hat{x},\hat{y},\hat{t}) = 2 \frac{\partial^2}{\partial \hat{x}^2} \ln \theta(\psi_1, \psi_2, \ldots, \psi_N; B) \qquad 2.7$$

where θ is a Riemann theta function of genus N, composed of N two-dimensional phase variables ψ and an $N \times N$ symmetric Riemann matrix B. Genus 1 solutions are exactly equivalent to cnoidal waves; i.e., they are singly periodic, two-dimensional, nonlinear waves which propagate at some angle to the $\hat{x}$-direction. Genus 2 solutions are the subject of the investigation herein. These solutions are biperiodic, truly three-dimensional, nonlinear waves which propagate with permanent form at a constant velocity. The resulting two-dimensional surface pattern therefore appears stationary to an observer translating with the waves at the correct velocity. Genus 3 and higher order solutions are multiperiodic solutions which cannot be characterized as permanent form since no translating coordinate system exists that allows the solutions to become stationary.

Dubrovin's detailed treatment of the subject culminated, for our purposes, in an analysis of the genus 1, 2, and 3 solutions to the KP equation. He presented a series of theorems, lemmas, and corollaries which proved the existence and uniqueness of solutions to the KP equation. He also developed the basic guidelines which are required for actually constructing genus 1 and genus 2 solutions although he presented no explicit examples for doing so. Dubrovin's paper laid the theoretical foundation for extending the theory from a highly abstract mathematical proof into a computationally effective tool. The formidable task of utilizing Dubrovin's theory in the development of an analytical wave model capable of yielding exact, truly three-dimensional, biperiodic genus 2 solutions of the KP equation was successfully accomplished by Segur and Finkel (1985). A detailed description of the mathematical machinery developed by SF for genus 2 KP solutions is presented in Chapter 3.

Although exact biperiodic wave solutions for shallow water have only recently been presented, three-dimensional approximations have been studied and reported in the literature. Solutions for interacting waves have been reported by Miles (1977), Bryant (1982), Melville (1980), and Roberts and Schwartz (1983). Each of these investigations show nonlinear coupling of two intersecting waves which are in qualitative agreement with the exact solutions and with the observed behavior of interacting waves. Since each of these results is produced by approximation methods, they are not relatable to the observed characteristics of intersecting waves. The exact solutions presented by Segur and

Finkel described herein represent the first exact biperiodic solution which can be quantitatively compared to observed waves.

CHAPTER 3

THE KADOMTSEV-PETVIASHVILI (KP) EQUATION

This chapter is intended to provide a background for the study of genus 2 solutions of the KP equation. It begins with a formal derivation of the KP equation in order to document the procedures used and the assumptions underlying this approximate model equation. Following the derivation, a complete presentation of the analytical genus 2 solution, as derived by Segur and Finkel (1985), is presented. The potential relevancy of this solution as a wave model is made through the presentation of several graphical examples demonstrating the three-dimensional nonlinear structure of these exact solutions. The following sections provide the background for developing the experimental portion of the study and the determination of the correspondence between exact solutions and measured waves.

3.1 Derivation of the KP Equation

The KP equation was first proposed, but not formally derived, by Kadomtsev and Petviashvili (1970). Their interest in the equation was a consequence of their study on the stability of solitary waves to transverse (crest-wise) perturbations. The formal derivation of the KP equation, which closely parallels that of the KdV equation, begins by defining the fluid and its boundaries. Consider for example a three-dimensional, inviscid, incompressible, flow domain as shown in Figure 3.1.

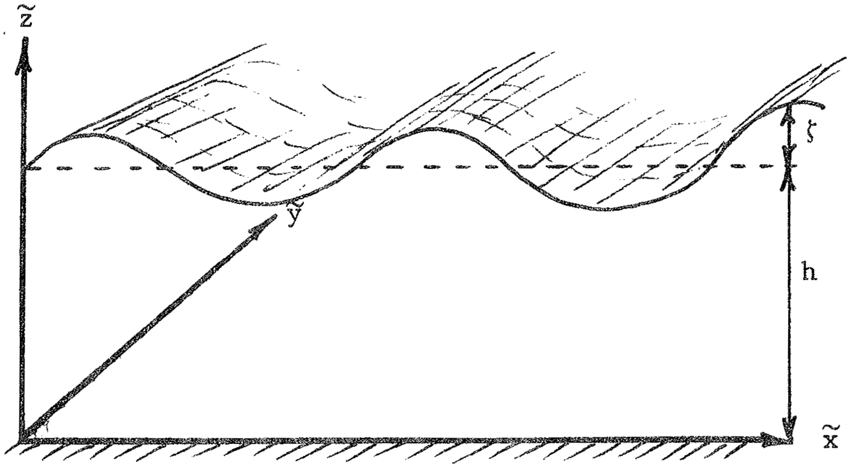

Figure 3.1 Schematic diagram of flow domain

The equations governing this flow are Euler's equations for the conservation of linear momentum

$$\frac{\partial u}{\partial \tilde{t}} + u\,\frac{\partial u}{\partial \tilde{x}} + v\,\frac{\partial u}{\partial \tilde{y}} + w\,\frac{\partial u}{\partial \tilde{z}} = -\,\frac{1}{\rho}\,\frac{\partial p}{\partial \tilde{x}}$$

$$\frac{\partial v}{\partial \tilde{t}} + u\,\frac{\partial v}{\partial \tilde{x}} + v\,\frac{\partial v}{\partial \tilde{y}} + w\,\frac{\partial v}{\partial \tilde{z}} = -\,\frac{1}{\rho}\,\frac{\partial p}{\partial \tilde{y}}$$

$$\frac{\partial w}{\partial \tilde{t}} + u\,\frac{\partial w}{\partial \tilde{x}} + v\,\frac{\partial w}{\partial \tilde{y}} + w\,\frac{\partial w}{\partial \tilde{z}} = -\,\frac{1}{\rho}\,\frac{\partial p}{\partial \tilde{z}} - g \qquad 3.1$$

and the continuity equation for the conservation of mass

$$\frac{\partial u}{\partial \tilde{x}} + \frac{\partial v}{\partial \tilde{y}} + \frac{\partial w}{\partial \tilde{z}} = 0 \ . \qquad 3.2$$

In addition, the assumption of irrotational motion yields the following equalities:

$$\frac{\partial w}{\partial \tilde{y}} - \frac{\partial v}{\partial \tilde{z}} = \frac{\partial w}{\partial \tilde{x}} - \frac{\partial u}{\partial \tilde{z}} = \frac{\partial v}{\partial \tilde{x}} - \frac{\partial u}{\partial \tilde{y}} = 0 \ . \qquad 3.3$$

In the above dimensional equations, $\tilde{t}$ represents time and u, v, and w represent the Eulerian velocity components in the orthogonal $\tilde{x}$, $\tilde{y}$, and $\tilde{z}$ directions. Additional terms include the fluid density ρ, the fluid pressure p, and the acceleration of gravity g. It follows from Equation 3.3 that the velocity field is derivable from a potential ϕ which can be written in the following form:

$$\frac{\partial \phi}{\partial \tilde{x}} = u \ , \quad \frac{\partial \phi}{\partial \tilde{y}} = v \ , \quad \frac{\partial \phi}{\partial \tilde{z}} = w \ . \qquad 3.4$$

A kinematic boundary conditions for the free surface of the flow regime shown in Figure 3.1 can be written as

$$\frac{\partial \zeta}{\partial \tilde{t}} + u \frac{\partial \zeta}{\partial \tilde{x}} + v \frac{\partial \zeta}{\partial \tilde{y}} - w = 0 \qquad \text{on } (\tilde{x},\tilde{y},h+\zeta,\tilde{t}) \qquad 3.5$$

whereas the corresponding boundary condition for a horizontal bottom is written as

$$w = 0 \qquad \text{on } (\tilde{x},\tilde{y},0,\tilde{t}) \qquad 3.6$$

where ζ represents the elevation of the free surface measured from the quiesent fluid level. A dynamic condition for the free surface boundary can be written by combining Equations 3.1 through 3.4 to find

$$\frac{\partial \phi}{\partial \tilde{t}} + \frac{1}{2}\,|\nabla\phi|^2 + g\zeta = 0 \qquad \text{on } (\tilde{x},\tilde{y},h+\zeta,\tilde{t}) \qquad 3.7$$

where the linear operator $\nabla = (\partial_{\tilde{x}}, \partial_{\tilde{y}}, \partial_{\tilde{z}})$ is used and the pressure on the free surface is assumed constant. (Since this constant value can be absorbed into the velocity potential, the pressure is conveniently set to zero in the above derivation.)

The equations can now be consolidated to define a boundary value problem for the motion of the fluid domain shown in Figure 3.1 subject to the defined boundary conditions. For example, equations 3.2 and 3.4 are combined to yield Laplace's equation for the velocity potential which determines the three-dimensional velocity distribution of the fluid domain; i.e.,

$$\nabla^2\phi = 0 \ . \qquad 3.8$$

The fluid motion defined by the velocity potential is not only required to satisfy equation 3.8 at all points in the flow domain but also to satisisfy the boundary conditions defined by Equations 3.5, 3.6, and 3.7 on the upper and lower boundaries. These conditions are rewritten in terms of the velocity potential and surface elevation to yield the kinematic free surface boundary condition

$$-\zeta_{\tilde{t}} - \phi_{\tilde{x}}\,\zeta_{\tilde{x}} - \phi_{\tilde{y}}\,\zeta_{\tilde{y}} + \phi_{\tilde{z}} = 0 \text{ on } (\tilde{x},\tilde{y},h+\zeta,\tilde{t}) \qquad 3.9$$

the kinematic bottom boundary condition

$$\phi_{\tilde{z}} = 0 \qquad \text{on } (\tilde{x},\tilde{y},0,\tilde{t}) \qquad 3.10$$

and the dynamic free surface boundary condition

$$\phi_{\tilde{t}} + \frac{1}{2}\,|\nabla\phi|^2 + g\zeta = 0\ . \qquad \text{on } (\tilde{x},\tilde{y},h+\zeta,\tilde{t}) \qquad 3.11$$

The governing equations and associated boundary conditions represented by Equations 3.8 through 3.11 cannot be solved analytically in their present form; however, a solution can be obtained if certain simplifying assumptions are made. For example, if all of the nonlinear terms in the governing equations and boundary condition equations are assumed negligible, the resulting linear system of equations becomes solvable. Of course, this results in linear wave theory in which velocities and surface elevations are constructed in terms of the normal-mode solutions; i.e., sine and cosine functions.

The derivation of the nonlinear KdV and KP equations requires a more systematic approach since the nonlinear subtleties of these solutions are lost in the linear approximation. The decision as to which terms are retained and which are omitted is made through a systematic study of the relative magnitude of each term in the equation based on the existence and subsequent ordering of certain small parameters. This approximation is accomplished through the use of power series expansions in terms of the small parameters.

The formal derivation of the KP equation first requires the scaling of all dimensional quantities by introducing the following "scales." A global length scale for the wave, usually considered to be the wavelength, is defined as L, for which a corresponding wavenumber $k = 2\pi/L$ is defined. For three-dimensional flow, k represents a vector wavenumber with $\tilde{x}$ and $\tilde{y}$ components. The magnitude of this wavenumber is defined by the relationship $|k| = (l^2 + m^2)^{1/2}$ where l represents the $\tilde{x}$-direction wavenumber and m represents that in the $\tilde{y}$-direction. An amplitude scale, descriptive of the wave crest height, is defined as a. A vertical scale h is defined as the depth of flow in which the wave is propagating.

These three representative scales (k, a, and h) are similar to those used by Stokes (1847), Korteweg and deVries (1895), and Ursell (1953). One additional scale is introduced in order to define a reference speed of propagation for the wave. This scale is simply defined as the celerity of a shallow water wave, as found in linear wave theory; i.e.,

$$C = \sqrt{gh} \ .$$

The purpose of defining representative scales for a given flow regime is to enable one to characterize the wave behavior in a systematic manner similar to the approach described by Ursell (1953). This characterization is made by analyzing the relative magnitude of selected combinations of the representative scales for that wave. Three of these combinations are used for defining the characteristics of the KP equation. Each of these resulting "scaled parameters" will be used in the formal derivation in order to insure that the derived evolution equation will describe a wave field which will behave in a manner consistent with the defined relative magnitudes of the scaling parameters. The first of these parameters, given below,

$$\alpha = \frac{a}{h}$$

defines a wave amplitude to depth parameter which provides an indication of the degree of nonlinearity of the wave. Smallness of this parameter implies weak nonlinearity and, in the limit $\alpha \to 0$, linear wave theory is recovered. The second parameter

$$\beta = (kh)^2$$

provides a measure of the length of the wave with respect to the depth of flow in which the wave is propagating. Smallness of this parameter implies shallow-water conditions so that dispersion is weak. The third parameter provides a measure of the three-dimensionality of the wave. This parameter, shown below,

$$\varepsilon = \left(\frac{m}{l}\right)^2$$

indicates the direction of propagation of the wave field with respect to a defined orthogonal coordinate system. Smallness of the parameter, for example, indicates that the primary direction of propagation is in the $\tilde{x}$-direction and that the wave is weakly three-dimensional. When the parameter vanishes, the flow becomes the two-dimensional flow field governed by the KdV equation.

The formal derivation of the KP equation is based on the assumption that each of the defined parameters are small (i.e. $<< 1$) which implies a weakly nonlinear, weakly dispersive, and weakly three-dimensional flow. The relative magnitudes of each of these parameters will be chosen in a subsequent analysis. The derivation begins with the scaling of the governing equation and associated boundary conditions. This is accomplished by introducing the following non-dimensional quantities:

$$x = k\tilde{x} \qquad 3.12$$

$$y = k\tilde{y} \qquad 3.13$$

$$z = \frac{\tilde{z}}{h} \qquad 3.14$$

$$\eta = \frac{\zeta}{a} \qquad 3.15$$

$$t = Ck\tilde{t} \qquad 3.16$$

$$\Phi = \frac{Ck}{ga}\,\phi\ . \qquad 3.17$$

Substitution into Laplace's equation (Equation 3.8) results in the following relationship:

$$\beta\,(\Phi_{xx} + \Phi_{yy}) + \Phi_{zz} = 0\ . \qquad 3.18$$

In a similar manner, the kinematic free surface boundary condition of Equation 3.9 is written

$$\eta_t + \alpha\,\Phi_x\,\eta_x + \alpha\,\Phi_y\eta_y - \frac{1}{\beta}\,\Phi_z = 0 \qquad 3.19$$

and the corresponding kinematic bottom boundary condition of Equation 3.10 takes the form

$$\Phi_z = 0\ . \qquad 3.20$$

The dynamic free surface boundary condition of Equation 3.11 becomes

$$\Phi_t + \frac{1}{2}\,\alpha\,\Phi_x^2 + \frac{1}{2}\,\alpha\,\Phi_y^2 + \frac{1}{2}\,\frac{\alpha}{\beta}\,\Phi_z^2 + \eta = 0\ . \qquad 3.21$$

Equations 3.18-3.21 now represent the complete nondimensional equations governing the flow.

Next, each of the dependent variables is represented in a power series expansion in terms of a small parameter. For the velocity potential, we assume the following form

$$\Phi(x,y,z,t;\beta) = \sum_{m=0}^{\infty} \beta^{m} \Phi_{m} (x,y,z,t) \qquad 3.22$$

which is substituted into Equation 3.18. Collecting all terms with multipliers of like order of powers of β yields the form below.

$$\begin{aligned} \beta^{0} (\Phi_{0zz}) + \beta^{1}(\Phi_{0xx} + \Phi_{0yy} + \Phi_{1zz}) & \\ + \beta^{2}(\Phi_{1xx} + \Phi_{1yy} + \Phi_{2zz}) + \ldots = 0 & \end{aligned} \qquad 3.23$$

Since each sum of terms in Equation 3.23 is ordered by powers of the small parameter β, the overall equation is satisfied if, and only if, each sum of terms is zero. Hence, the original single equation in terms of Φ is replaced by an infinite set of equations for Φ_m. The equations resulting from Equation 3.23 are shown below.

$$O(\beta^{0}) \text{ effects:} \quad \Phi_{0zz} = 0 \qquad 3.24$$

$$O(\beta^{1}) \text{ effects:} \quad \Phi_{0xx} + \Phi_{0yy} + \Phi_{1zz} = 0 \qquad 3.25$$

$$O(\beta^{2}) \text{ effects:} \quad \Phi_{1xx} + \Phi_{1yy} + \Phi_{2zz} = 0 \qquad 3.26$$

Integration of Equation 3.24 with respect to z yields

$$\Phi_0 = G(x,y,t)z + \phi_0(x,y,t)$$

where $G(x,y,t)$ and $\phi_0(x,y,t)$ are integration constants. Application of the bottom boundary condition of Equation 3.20 (i.e. $\Phi_z = 0$) requires

$$G(x,y,t) = 0$$

so that

$$\Phi_0(x,y,z,t) = \phi_0(x,y,t) \ . \qquad 3.27$$

Similar integrations of Equations 3.25 and 3.26 and application of the bottom boundary condition result in the following two relationships:

$$\Phi_1 \ (x,y,z,t) = -\frac{1}{2} \left(\phi_{0xx} + \phi_{0yy}\right) z^2 + \phi_1 \qquad 3.28$$

and

$$\begin{aligned} \Phi_2(x,y,z,t) = {} & \frac{1}{4!} \left(\phi_{0xxxx} + 2\phi_{0xxyy} + \phi_{0yyyy}\right) z^4 \\ & - \frac{1}{2!} \left(\phi_{1xx} + \phi_{1yy}\right) z^2 + \phi_2 \ . \end{aligned} \qquad 3.29$$

Substitution of these results into equation 3.22 yields the following expansion for Φ, the velocity potential, correct to the third order.

$$\Phi = \phi_0 + \beta\left[-\frac{1}{2}\left(\phi_{0xx} + \phi_{0yy}\right)z^2 + \phi_1\right] + \beta^2\left[\phi_2 - \frac{1}{2}\left(\phi_{1xx} + \phi_{1yy}\right)z^2 + \frac{1}{24}\left(\phi_{0xxxx} + 2\phi_{0xxyy} + \phi_{0yyyy}\right)z^4\right] + O(\beta^3). \quad 3.30$$

The further analysis requires the introduction of a slow time scale. This new time scale will permit the suppression of secular terms that arise in the analysis of the dynamic free surface boundary condition. Define

$$T = \varepsilon t \quad 3.31$$

where ε represents the small parameter defined previously. In addition, we will make a Galilean transformation to a uniformly translating coordinate system by letting

$$X = x - t \ . \quad 3.32$$

Differentiation between the different length scales in the x-, y- and z-directions will also be made by explicitly defining the following:

$$Y = \varepsilon^{1/2} y \qquad 3.33$$

$$Z = z \ . \qquad 3.34$$

The new scales of Equations 3.31 through 3.34 are substituted into Equation 3.30 to obtain the following slow time representation for the second order correct velocity potential.

$$\begin{aligned} \Phi(X,Y,Z,T;\ \beta) = \phi_0 &+ \beta \left[- \frac{1}{2} \left(\phi_{OXX} + \varepsilon^2 \phi_{OYY} \right) Z^2 + \phi_1 \right] \\ &+ \beta^2 \left[\phi_2 - \frac{1}{2} \left(\phi_{1XX} + \varepsilon^2 \phi_{1YY} \right) Z^2 \right. \\ &\left. + \frac{1}{24} \left(\phi_{OXXXX} + \varepsilon^2 \, 2\phi_{OXXYY} + \varepsilon^4 \, \phi^4_{OYYYY} \right) Z^4 \right] + O(\beta^3) \qquad 3.35 \end{aligned}$$

We now introduce the following power series expansion representation of the free surface displacement in terms of the new slow time scale parameter.

$$\eta(X,Y,Z,T;\varepsilon) = \sum_{m=0}^{\infty} \varepsilon^m \, \eta_m(X,Y,Z,T) \qquad 3.36$$

The kinematic and dynamic free surface boundary conditions of Equations 3.19 and 3.21 respectively can now be written in terms of the slow time scale. This substitution results in the following two equations for the velocity potential and surface displacement:

$$-\eta_X + \varepsilon\eta_T + \alpha\Phi_X\eta_X + \alpha\varepsilon\Phi_Y\eta_Y - \frac{1}{\beta}\Phi_Z = 0 \qquad 3.37$$

and

$$-\Phi_X + \varepsilon\Phi_T + \frac{1}{2}\alpha\Phi_X^2 + \frac{1}{2}\alpha\varepsilon\Phi_Y^2 + \frac{1}{2}\frac{\alpha}{\beta}\Phi_Z^2 + \eta = 0 \ . \qquad 3.38$$

Note that the new governing equations now contain all three small parameters (α, β, and ε) which have been introduced to allow for the specific ordering of the final wave solution. The key to the derivation of the KP equation is the assumption that each of the parameters are of an equivalent order of magnitude. This assumption is made by letting

$$O(\alpha) = O(\beta) = O(\varepsilon) \ . \qquad 3.39$$

Substitution of the series expansions for the velocity potential and the free surface displacement (Equations 3.35 and 3.36) into the boundary equations 3.37 and 3.38, expansion, and consolidation of ordered terms in ε yields the following two relationships:

$$\varepsilon^0\left(-\phi_{0X} + \eta_0\right) + \varepsilon^1\left(\frac{1}{2}\phi_{0XXX} - \phi_{1X} + \frac{1}{2}\phi_{0X}^2 + \phi_{0T} + \eta_1\right) + O(\varepsilon^2) = 0 \qquad 3.40$$

and

$$\varepsilon^0\left(-\eta_{0X} + \phi_{0XX}\right) + \varepsilon^1\left(-\eta_{1X} - \eta_{0T} + \phi_{0X}\eta_{0X} + \phi_{0YY}\right.$$

$$\left. + \phi_{1XX} - \frac{1}{6}\phi_{0XXXX} + \phi_{0XX}\eta_0\right) + O(\varepsilon^2) = 0 \, . \qquad 3.41$$

Analysis of the $O(\varepsilon^0)$ terms show that

$$\eta_0 = \phi_{0X} \, . \qquad 3.42$$

A similar analysis of the $O(\varepsilon^1)$ terms yields

$$\eta_1 - \phi_{1X} = -\phi_{0T} - \frac{1}{2}\phi_{0XXX} - \frac{1}{2}\phi_{0X}^2 \qquad 3.43$$

and

$$\eta_{1X} - \phi_{1XX} = \eta_{0X}\phi_{0X} + \eta_0\phi_{0XX} - \frac{1}{6}\phi_{0XXXX} + \phi_{0YY} + \eta_{0T} \, . \qquad 3.44$$

Now equating the partial derivative (with respect to X) of Equation 3.43 with Equation 3.44, again taking the X partial derivative of the entire result, and consolidating terms yields

$$\left(-\phi_{0TX} - \frac{1}{3}\phi_{0XXXX} - \phi_{0X}\phi_{0XX} - \eta_{0X}\phi_{0X} - \eta_0\phi_{0XX} - \eta_{0T}\right)_X - \phi_{0YYX} = 0. \quad 3.45$$

Substitution of Equations 3.4, and 3.42 into Equation 3.45 results in the Kadomtsev-Petviashvili equation,

$$\left(2u_{0T} + 3u_0u_{0X} + \frac{1}{3}u_{0XXX}\right)_X + u_{0YY} = 0 \;. \qquad 3.46$$

where $u_0 = \phi_{0X} = \eta_0$. A final transformation of variables is now required in order to write Equation 3.46 in the form used by Segur and Finkel (1984). Let

$$\hat{x} = X$$

$$\hat{y} = Y$$

$$\hat{t} = \frac{1}{6}T$$

$$f = \frac{3}{2}u_0 \;.$$

The substitution of these variables into Equation 3.45 results in the following form of the KP equation which will be used extensively in the remainder of this study.

$$(f_{\hat{t}} + 6ff_{\hat{x}} + f_{\hat{x}\hat{x}\hat{x}})_{\hat{x}} + 3f_{\hat{y}\hat{y}} = 0 \qquad 3.47$$

3.2 Solutions of the KP Equation in terms of Riemann Theta Functions of Genus 2

Krichever (1976) showed that the KP equation admitted an infinitely dimensional family of exact quasi-periodic solutions which could be written in terms of Riemann theta functions of genus N. The techniques employed by Krichever were extended by Dubrovin (1981) to specifically address the genus 1, 2, and 3 solutions. The solutions relevant to this study are the biperiodic genus 2 solutions which are truly three-dimensional and have two real periods, both spatially and temporally. Dubrovin provided the necessary existence and uniqueness criteria required for computing these solutions. The task of actually applying Dubrovin's criteria and solution approach to compute an exact genus 2 solution of the KP equation was first completed by Segur and Finkel in 1985. This, of course, required the development of a considerable amount of mathematical machinery to implement Dubrovin's outline. The purpose of this section is to present, and describe, the machinery which was presented by SF to compute these genus 2 solutions.

Genus 2 solutions of the KP equation can be written as

$$f(\hat{x},\hat{y},\hat{t}) = 2\,\frac{\partial^2}{\partial \hat{x}^2} \ln \theta\,(\psi_1,\ \psi_2,\ B) \qquad 3.48$$

where θ is the genus 2 Riemann theta function, composed of a 2-component phase variable $\vec{\psi}$ and a (2 X 2) real-valued Riemann matrix B.

The construction of this solution begins with the introduction of the two phase variables

$$\psi_1 = \mu_1\hat{x} + \nu_1\hat{y} + \omega_1\hat{t} + \psi_{10}$$

and 3.49

$$\psi_2 = \mu_2\hat{x} + \nu_2\hat{y} + \omega_2\hat{t} + \psi_{20} \ .$$

The parameters μ_1, μ_2 and ν_1, ν_2 are wave numbers in the $\hat{x}$- and $\hat{y}$-directions, respectively, while ω_1, ω_2 represents the angular frequencies of the wave with respect to the translating coordinate system in which the KP equation operates. The constants ψ_{10}, ψ_{20} represent a constant shift in phase and are of no dynamical significance. A much more thorough description of these coefficients will be presented later. The second ingredient involves the specification of a symmetric, real-valued, negative definite 2 X 2 Riemann matrix of the form shown below.

$$B = \begin{vmatrix} b_{11} & b_{12} \\ b_{12} & b_{22} \end{vmatrix} \qquad 3.50$$

Negative definiteness is assured by requiring

$$b_{11} < 0, \quad b_{22} < 0, \quad b_{11}\, b_{22} - b_{12}^2 > 0 \ . \qquad 3.51$$

The role of the phase variables and the Riemann matrix in the specification of the theta function can now be shown. A genus 2 Riemann theta function can be defined by a double Fourier series (Segur and Finkel, 1985)

$$\Theta\,(\psi_1, \psi_2, B) = \sum_{m_1=-\infty}^{\infty} \sum_{m_2=-\infty}^{\infty} \exp\left\{\frac{1}{2}\,\vec{m}\cdot B\cdot\vec{m} + i\vec{m}\cdot\vec{\psi}\right\} \qquad 3.52$$

where $\vec{m} = (m_1, m_2)$ and the products are defined by

$$\vec{m}\cdot B\cdot\vec{m} = m_1^2 b_{11} + 2m_1 m_2 b_{12} + m_2^2 b_{22}$$

and

$$\vec{m}\cdot\vec{\psi} = m_1\psi_1 + m_2\psi_2 \ .$$

The theta function requires two additional refinements in order to assure a unique genus 2 solution. For example, SF (1985) showed that two different Riemann matrices could result in identical theta functions. These two matrices are therefore equivalent and can be related to each other by the appropriate transformation. The existence of equivalent matrices which produce identical solutions introduces a question as to whether or not the solution is unique. In order to resolve this ambiguity, SF (1985) introduced the concept of a basic Riemann matrix. They chose the following parameters to be natural representations for a basic Riemann matrix:

$$b = \max (b_{11}, b_{22})$$

$$\lambda = b_{12}/b$$

$$d = \det B/b \qquad 3.53$$

where both b and d are negative and λ is real. Segur and Finkel (1984) chose the basic Riemann matrix to be of the form

$$B = \begin{vmatrix} b & b\lambda \\ b\lambda & b\lambda^2 + d \end{vmatrix} \qquad 3.54$$

where the requirement that the matrix is basic and negative definite is satisified by

$$b < 0, \quad \lambda^2 \le \frac{1}{4}, \; d \le b\,(1 - \lambda^2) \; . \qquad 3.55$$

Under these conditions, a basic Riemann matrix generates one and only one theta function. Another difficulty with the general definition of the theta function as given by Equation 3.52 results when the off diagonal terms of the matrix become zero. Diagonal matrices are referred to as decomposable, otherwise, they are indecomposable. Dubrovin (1981) proved that nontrivial genus 2 solutions of the KP equation only result from indecomposable matrices. Although Dubrovin (1981) gave an explicit test for decomposability, Segur and Finkel (1985) provided a simpler test in terms of their parameters for a basic Riemann matrix. A basic Riemann matrix is decomposable if, and only if, $\lambda = 0$.

A real-valued, negative definite, indecomposable theta function has been associated with its corresponding basic Riemann matrix of the form given by Equation 3.54. The requirements imposed on that matrix, are that the parameters b, d, and λ are real, and that λ is non-zero. The basic definition of a genus 2 Riemann theta function can now be written in terms of these new parameters.

$$\theta(\psi_1, \psi_2, B) = \sum_{m_2=-\infty}^{\infty} \exp\left\{\frac{1}{2}\, dm_2^2\right\} \sum_{m_1=-\infty}^{\infty} \exp\left\{\frac{1}{2}\, b\left(m_1 + \lambda m_2\right)^2\right\} \times \cos\left(m_1\psi_1 + m_2\psi_2\right) \qquad 3.56$$

The above definition assures the existence of a real valued, indecomposible theta function, but it does not assure that the resulting theta function will provide a solution to the KP equation. This assurance requires the development of two additional concepts as noted by Dubrovin (1981). The new ingredients are theta-constants and two additional phase variables.

The concept of theta-constants begins with the definition of a two component vector $\vec{p}$ which can assume any one of the following four values:

$$\vec{p} = \begin{pmatrix} p_1 \\ p_2 \end{pmatrix} = \begin{pmatrix} 0 \\ 0 \end{pmatrix}, \begin{pmatrix} 1/2 \\ 0 \end{pmatrix}, \begin{pmatrix} 0 \\ 1/2 \end{pmatrix}, \begin{pmatrix} 1/2 \\ 1/2 \end{pmatrix}. \qquad 3.57$$

These values correspond to the four half-periods of a theta function (Dubrovin, 1981). Every Riemann matrix generates a four-component theta-constant (SF, 1985) which can be written in the following form

$$\hat{\Theta}\left[\vec{p}\right] = \sum_{m_1=-\infty}^{\infty} \sum_{m_2=-\infty}^{\infty} \exp\left\{\left(\vec{m} + \vec{p}\right)\cdot B\cdot\left(\vec{m} + \vec{p}\right)\right\} \qquad 3.58$$

where $\vec{m} = (m_1, m_2)$. Equation 3.58 can be written in terms of the basic parameters as

$$\hat{\Theta}[\vec{p}] = \sum_{m_2=-\infty}^{\infty} \exp\left\{d\left(m_2 + p_2\right)^2\right\} \sum_{m_1=-\infty}^{\infty} \exp\left\{b\left[m_1 + p_1 + \lambda\left(m_2 + p_2\right)\right]^2\right\} \qquad 3.59$$

where each theta-constant is differentiable with respect to the parameters b, d, and λ.

Secondly, two new phase variables ψ_3 and ψ_4 are defined in terms of the previous phase variables according to

$$\psi_4 = \psi_2 - \lambda\psi_1, \quad \psi_3 = \psi_1 - \tilde{\lambda}\,\psi_2 \qquad 3.60$$

where

$$\tilde{\lambda} = \frac{b_{12}}{b_{22}} = \frac{b\lambda}{b\lambda^2 + d} . \qquad 3.61$$

Wavenumbers and angular frequencies for these new phase variables can be written analogous to Equations 3.60 as

$$\mu_4 = \mu_2 - \lambda\mu_1 \quad , \quad \mu_3 = \mu_1 - \tilde{\lambda}\mu_2$$

$$\nu_4 = \nu_2 - \lambda\nu_1 \ , \quad \nu_3 = \nu_1 - \tilde{\lambda}\nu_2$$

$$\omega_4 = \omega_2 - \lambda\omega_1 \quad , \quad \omega_3 = \omega_1 - \tilde{\lambda}\omega_2 . \qquad 3.62$$

All of the components needed to state Dubrovin's main theorem have now been established. The theorem requires that a function in the form of Equation 3.48 is a solution to the KP equation if, and only if, the following matrix equation is satisified:

$$MX = 4SV \qquad 3.63$$

where the components of this matrix notation are

$$X = \begin{pmatrix} \mu_1\omega_1 + 3\nu_1^2 \\ \mu_1\omega_4 + \mu_4\omega_1 + 6\nu_1\nu_4 \\ \mu_4\omega_4 + 3\nu_4^2 \\ D \end{pmatrix} \qquad V = \begin{pmatrix} \mu_1^4 \\ 4\mu_1^3\mu_4 \\ 6\mu_1^2\mu_4^2 \\ 4\mu_1\mu_4^3 \\ \mu_4^4 \end{pmatrix} \tag{3.64}$$

and

$$M = \left(\frac{\partial}{\partial b}\hat{\theta}(p) \ , \ \frac{1}{2b}\frac{\partial}{\partial \lambda}\hat{\theta}(p) \ , \ \frac{\partial}{\partial d}\hat{\theta}(p) \ , \ \hat{\theta}(p)\right)$$

$$S = \left(\frac{\partial^2}{\partial b^2}\hat{\theta}(p) \ , \ \frac{\partial}{\partial b}\left(\frac{1}{2b}\frac{\partial}{\partial \lambda}\right)\hat{\theta}(p) \ , \ \frac{\partial}{\partial b}\frac{\partial}{\partial d}\hat{\theta}(p) \ , \right.$$

$$\left. \frac{\partial}{\partial d}\left(\frac{1}{2b}\frac{\partial}{\partial \lambda}\right)\hat{\theta}(p) \ , \ \frac{\partial^2}{\partial d^2}\hat{\theta}(p)\right) . \tag{3.65}$$

The parameter D shown in Equations 3.64 represents a constant of integration with no physical significance. The system of four equations represented by Equation 3.63 can always be solved if the Riemann matrix is indecomposable. The matrix equations of Equation 3.63 can be inverted to yield the following four relationships corresponding to the four possible values of the two component vector $\vec{p}$. The resulting relationships are

$$\left(\mu_1\omega_1 + 3\nu_1^2\right)\Big/\mu_1^4 = P_1\left(\frac{\mu_4}{\mu_1}, 4\right)$$

$$\left(\mu_1\omega_4 + \mu_4\omega_1 + 6\nu_1\nu_4\right)\Big/\mu_1^4 = P_2\left(\frac{\mu_4}{\mu_1}, 4\right) \qquad 3.66$$

$$\left(\mu_4\omega_4 + 3\nu_4^2\right)\Big/\mu_1^4 = P_3\left(\frac{\mu_4}{\mu_1}, 4\right)$$

$$D\Big/\mu_4^4 = P_4\left(\frac{\mu_4}{\mu_1}, 4\right)$$

where the parameters on the right hand side (P_1, P_2, P_3, P_4) represent well-defined fourth order polynomials in the variable μ_4/μ_1. (The polynomials in Equations 3.66 are obtained by inverting M.) .The constant of integration D is arbitrary so that its equation can be ignored. The two angular frequencies, ω_1 and ω_4, can be eliminated from Equations 3.66 to yield the following single relationship:

$$\left(\mu_1\nu_4 - \mu_4\nu_1\right)^2 = \frac{4}{3}\mu_1^6 P_6\left(\frac{\mu_4}{\mu_1}, 6\right) \qquad 3.67$$

where P_6 is a well-defined polynomial of degree 6. The left hand side of Equation 3.67 is real-valued; therefore, in order for Equation 3.67 to be satisified, the polynomial must be positive or zero; i.e.,

$$P_6\left(\frac{\mu_4}{\mu_1}, 6\right) \geq 0 \qquad 3.68$$

All existence and uniqueness criteria have now been presented for genus 2 solutions of the KP equation. The results are summarized as follows: Equation 3.48 represents a real-valued solution of the KP equation if,and only if, the associated Riemann theta function satisfies the criteria that 1) the phase variables, defined by Equations 3.49 are real-valued, 2) the associated Riemann matrix is basic and indecomposable, and 3) the polynomial relationships represented by Equations 3.63 are satisified. Provided these criteria are met, the following section demonstrates the computation of genus 2 solutions.

3.3 The Construction and Properties of Genus 2 Solutions

The construction of a genus 2 solution of the KP equation requires the specification of the following eleven parameters:

$$\mu_1, \quad \mu_2, \quad \nu_1, \nu_2, \quad \omega_1, \quad \omega_2, \quad \psi_{10}, \quad \psi_{20}, \; b, \quad d, \quad \lambda$$

The first eight of these parameters define the phase variables of Equations 3.49 while the remaining three are contained in the basic Riemann matrix defined by Equations 3.54. Dubrovin's theorem of Equation 3.63 provides three relationships among the eleven parameters; hence, there are only eight independent parameters required to specify a genus 2 solution. Of these, ψ_{10} and ψ_{20} serve only to determine the origin of the coordinate system and do not impact the dynamics of the solution. Thus, the most general genus 2 solution of the KP equation contains only six dynamical parameters which may be chosen freely. In order to provide insight into the structure of the genus 2 solutions and to be able to assess the effect of each parameter on the wave form, it is useful to specify the six dynamical parameters and calculate some typical solutions. In the experiments to follow, spatial and temporal symmetry will be exploited in order to expedite the measurement program. The symmetry of the generated waves provides three additional relationships among the six free parameters of the genus 2 solution; i.e.,

$$\mu_1 = \mu_2 \equiv \mu, \quad \nu_1 = -\nu_2 \equiv \nu, \quad \omega_1 = \omega_2 \equiv \omega$$

so that only three free parameters are available for specification. In addition, the experimental measurements make it convenient to choose b, μ, and λ for the free parameters. Making use of these additional constraints on the family of genus 2 solutions, two examples are calculated and presented in Figures 3.2 and 3.3. These figures show perspective views of the water surface at a fixed time when the parameter b is varied while μ and λ are held constant. (A more detailed examination of the solution sensitivity to each of the free parameters will be presented in Chapter 5.)

The exact solutions shown in Figures 3.2 and 3.3 are typical of all of the symmetric subfamily of genus 2 solutions. The surface wave pattern consists of a single, basic structure which repeats in a tiling of the entire water surface. A typical, basic structure can be isolated as in Figure 3.4 by the construction of a "period parallelogram." Inside the period parallelogram the wave crests form two V-shapes, pointing in

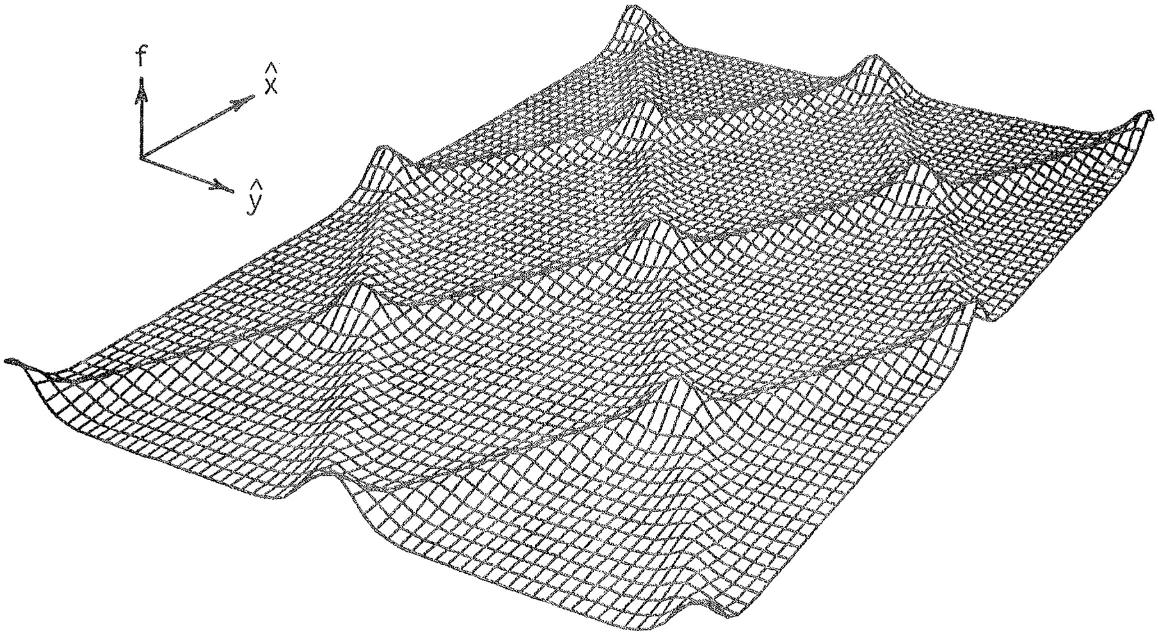

Figure 3.2 Example genus 2 solution ($b = -1.5$, $\mu = 0.5$, $\lambda = 0.1$)

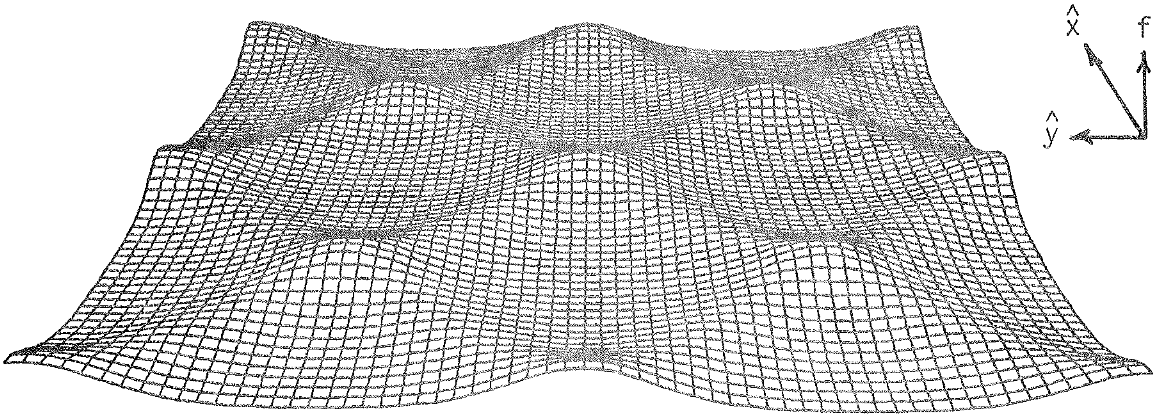

Figure 3.3 Example genus 2 solution ($b = -3.5$, $\mu = 0.5$, $\lambda = 0.1$)

opposite directions, and connected by a single, straight crest. Hereafter, the V-shaped region will be referred to as the "saddle region" while the straight crest between the V's will be termed the "stem." (The motivation for both names will become apparent shortly.) Note that crest amplitudes are largest in the stem region. The entire wave pattern propagates at a constant speed in a direction normal to the stem region. The sides of the period parallelogram coincide with lines of constant phase defined by the phase parameters noted in Figure 3.4. The periodicity in each of these two directions is increased by 2π across the period parallelogram. Specific relationships between other mathematical parameters and the wave structure inside the period parallelogram have not been established for the general case. However, SF examine the limit case of $b,d \to 0$ and prove that the actual wave crests of the saddle region coincide with lines of constant ψ_3 and ψ_4. The wave pattern in the limit $b,d \to 0$ is similar to that of Figure 3.2; mathematically, the solution appears as two KdV solitons, propagating at angles to one another and producing a third wave (the stem region) in a manner that is well known from other investigations (e.g. see Miles, 1977). In addition to the exact correspondence of ψ_3 and ψ_4 with individual wave crests in the saddle region, the interpretation of the genus 2 solutions as two intersecting wave trains is especially important to the experimental study and to the application of these solutions to actual ocean waves. (Interestingly, a stimulus for the interest by Segur in these waves was experiments on intersecting waves by Hammack, 1980.) The examination of the two-soliton limit solution also established that the two parameters λ and $\tilde{\lambda}$ are a measure of the rotation of the individual wave crests from the directions of periodicity; i.e.,

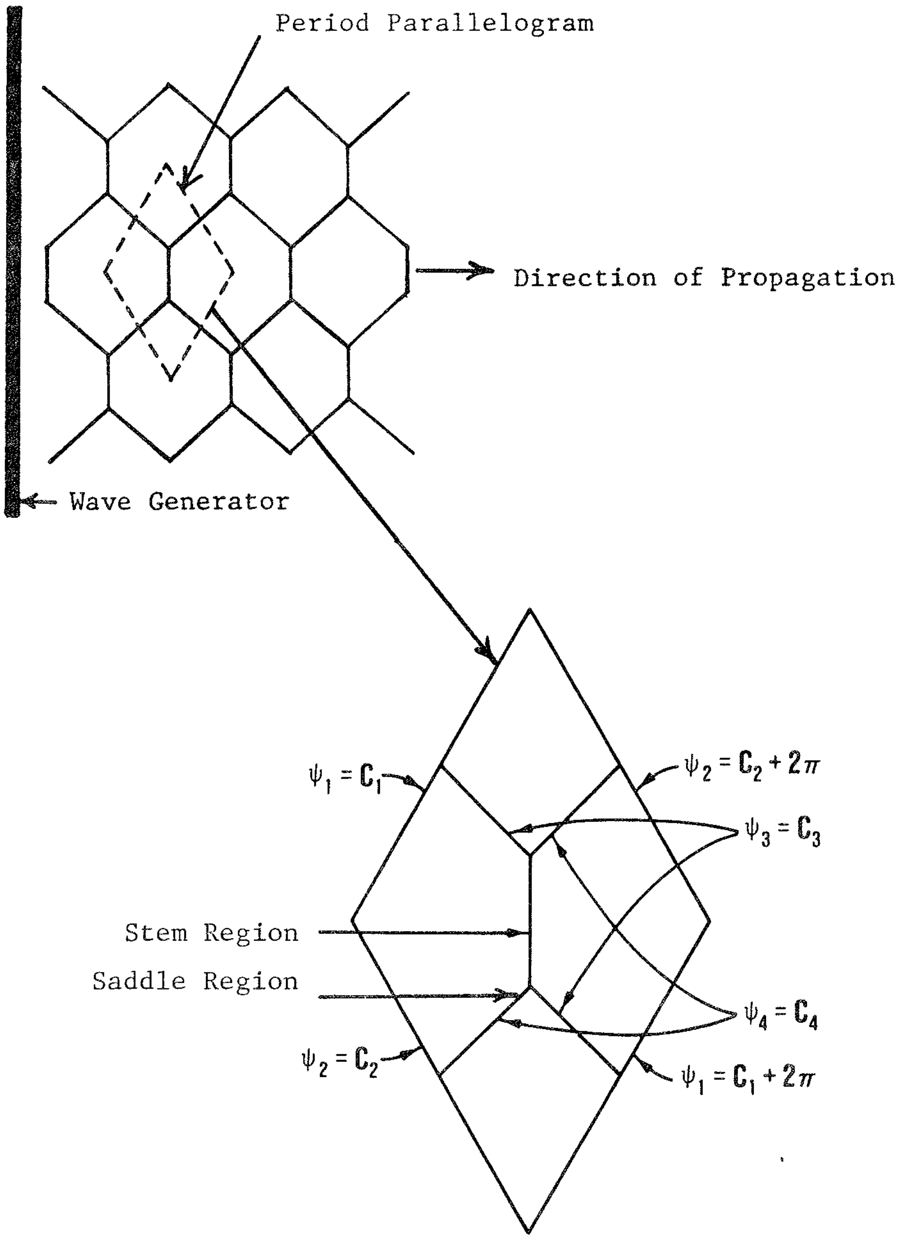

Figure 3.4 A basic period parallelogram

ψ_1 and ψ_2. Alternatively, this rotation is related to the amount of "phase shift" a wave experiences as a consequence of passing through a region of interaction with another wave. All of these aspects of the genus 2 solution will be made more explicit in Chapter 5.

CHAPTER 4

LABORATORY FACILITIES AND EXPERIMENTAL PROCEDURES

This chapter describes the laboratory facilities and experimental procedures used to generate the three-dimensional wave fields for comparison with exact genus 2 solutions of the KP equation. This chapter begins with a detailed description of the wave basin and wave generator. A basic knowledge of the wave making capability is essential to the formulation of an approach for generating candidate waves for comparison with genus 2 solutions. The wave-generation methodology follows the description of the physical facility. Due to the three-dimensional nature of the wave forms required for this study, considerable detail is presented for the data-gathering program to quantitatively measure the temporal and spatial structure of the wave field.

4.1 The Wave Basin

A wave basin measuring 98.0 ft wide, 184.0 ft long, and 2.5 ft deep is used for the experimental portion of the study. The walls of the basin are constructed of concrete filled, non-reinforced, cinder blocks resting on the concrete slab that forms the bottom of the basin. A schematic diagram of the wave basin is shown in Figure 4.1.

The concrete slab was poured by standard construction procedures to normally acceptable tolerances. The topography of the tank bottom is shown in Figure 4.2 and reveals a maximum variation of +/- 0.5 inch.

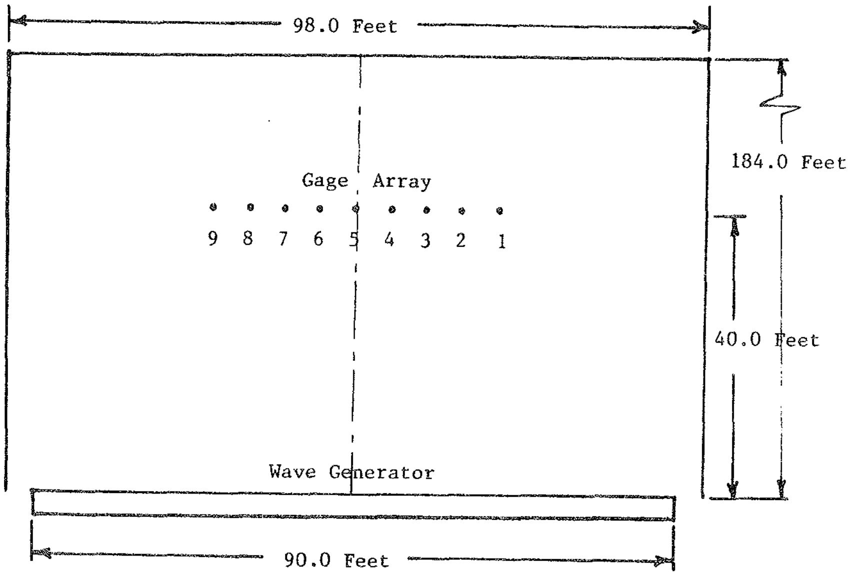

Figure 4.1 Schematic drawing of the wave basin

High and low areas resulted which can be identified in the figure. As will be discussed in a later section, the effects of these irregular zones were evidenced in the measured wave height patterns. The inset numbers shown in Figures 4.1 and 4.2 refer to the location of wave gages in the basin which will be described subsequently.

The downstream end of the wave basin, opposite the wave generator, is lined with rubberized horse-hair to a depth of approximately 2.0 ft, extending out a distance of approximately 6.0 ft from the wall. The purpose of this absorption material is to both reduce reflections from the rear wall of the basin during testing and to dissipate the oscillation of waves within the basin following testing. Sidewalls are not lined with the wave absorption material. The 90 ft wide wave generator,

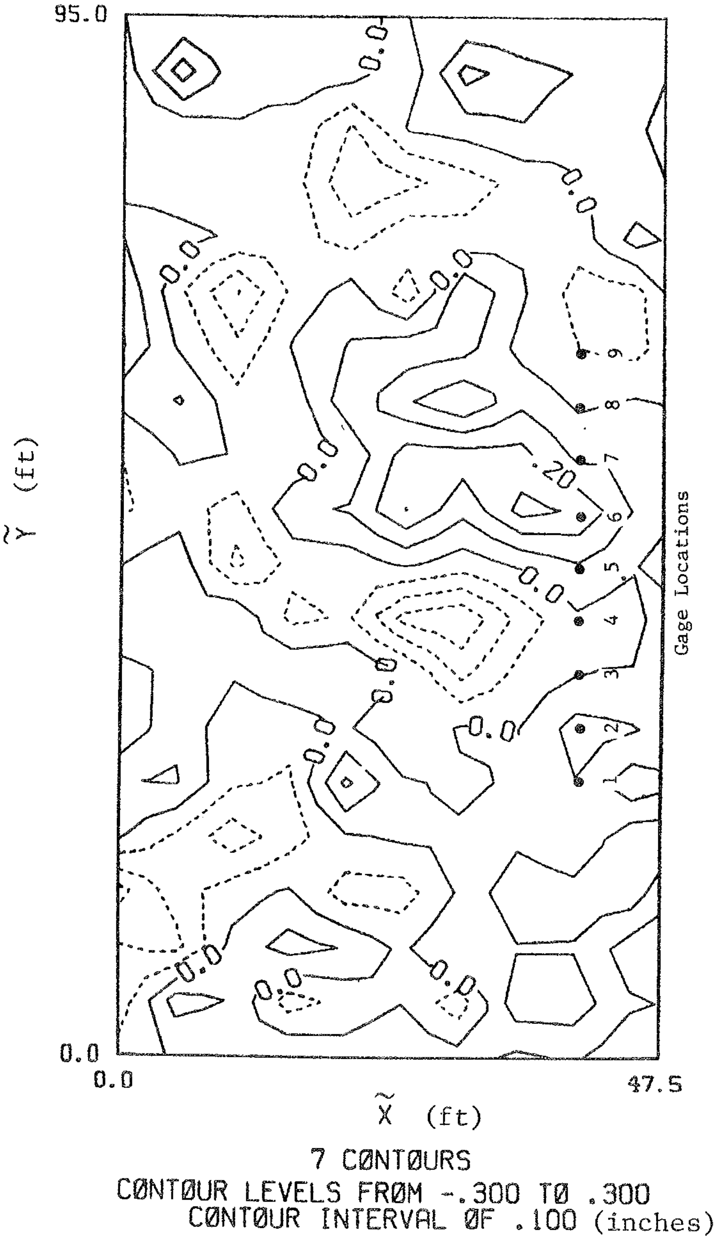

Figure 4.2 Bathymetry of the wave basin

which nearly spans the basin width, is located to the right of the gages in Figure 4.2.

4.2 The Directional Spectral Wave Generator

A wave generator capable of generating single or multiple wave forms of variable shape and direction is located at the US Army Engineer Waterways Experiment Station's Coastal Engineering Research Center (CERC) located in Vicksburg, Mississippi. This directional spectral wave generator is shown in Figure 4.3. It was designed and constructed for CERC by MTS Systems Corporation of Minneapolis, Minnesota, based on design specifications provided by CERC.

The directional spectral wave generator is composed of 60 individually programmable wave paddles. The generator was designed in a portable configuration of 4 separate, self contained modules (Chatham, 1984). Each of these modules is composed of 15 separate wave boards constructed on a steel frame as shown on the schematic drawing of Figure 4.4. Each module is equipped with six adjustable mounting pads for leveling purposes and can be moved by using four dollies at each of four lifting posts, two located in the front and two in the rear.

The wave boards, measuring 1.5 ft wide and 2.5 ft in height each, are individually driven in a piston-like motion by a 0.75 horsepower, direct-drive servo-motor located at the articulated joint between adjacent boards. The joint structure consists of a fixed and linked hinge as shown in Figure 4.5. Extremity points (left edge of paddle 1 and right edge of paddle 60) are driven by single fixed hinges. The connections between adjacent wave boards are smoothed by means of a flexible-plate seal which slides in slots located on each wave board.

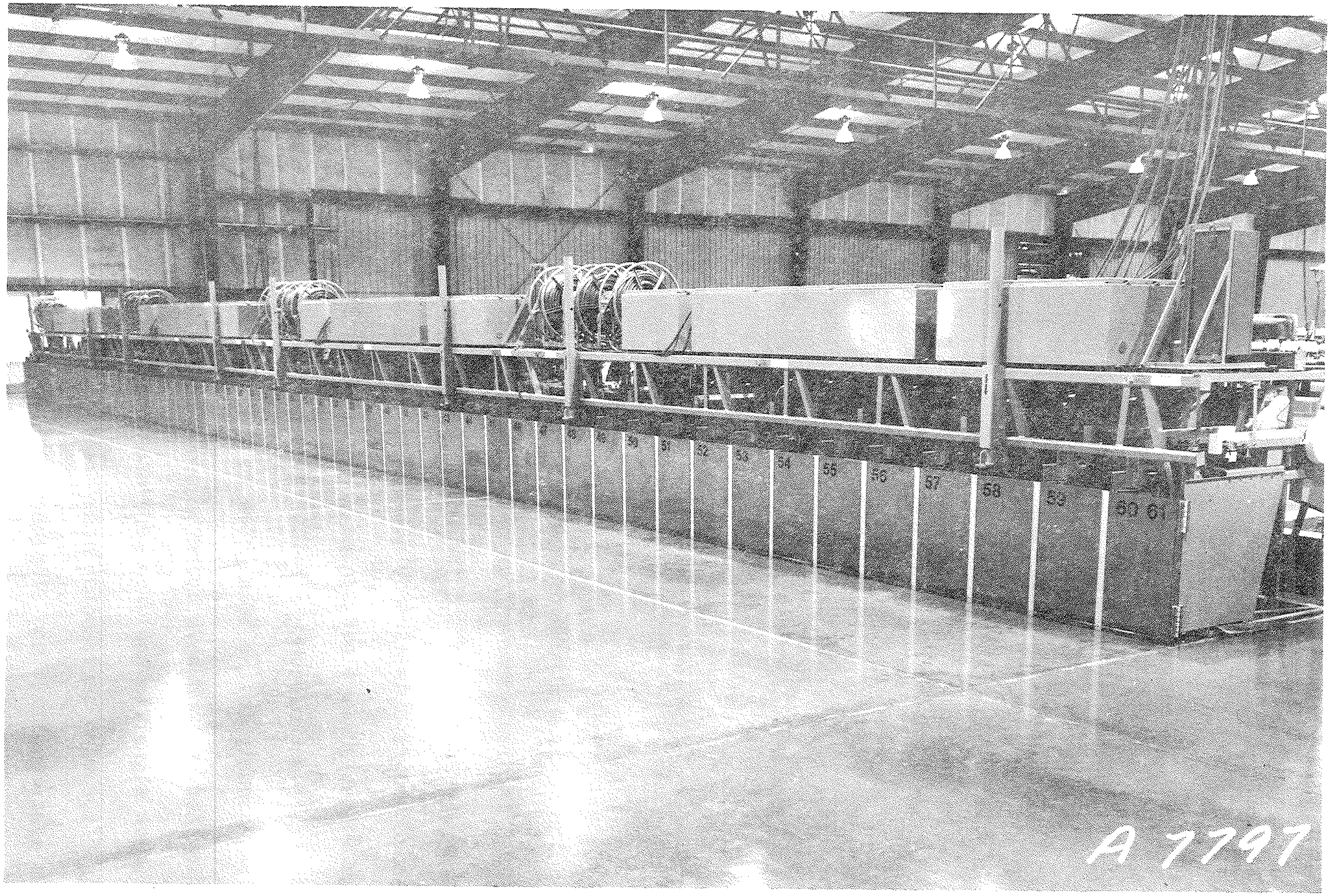

Figure 4.3 The directional spectral wave generator

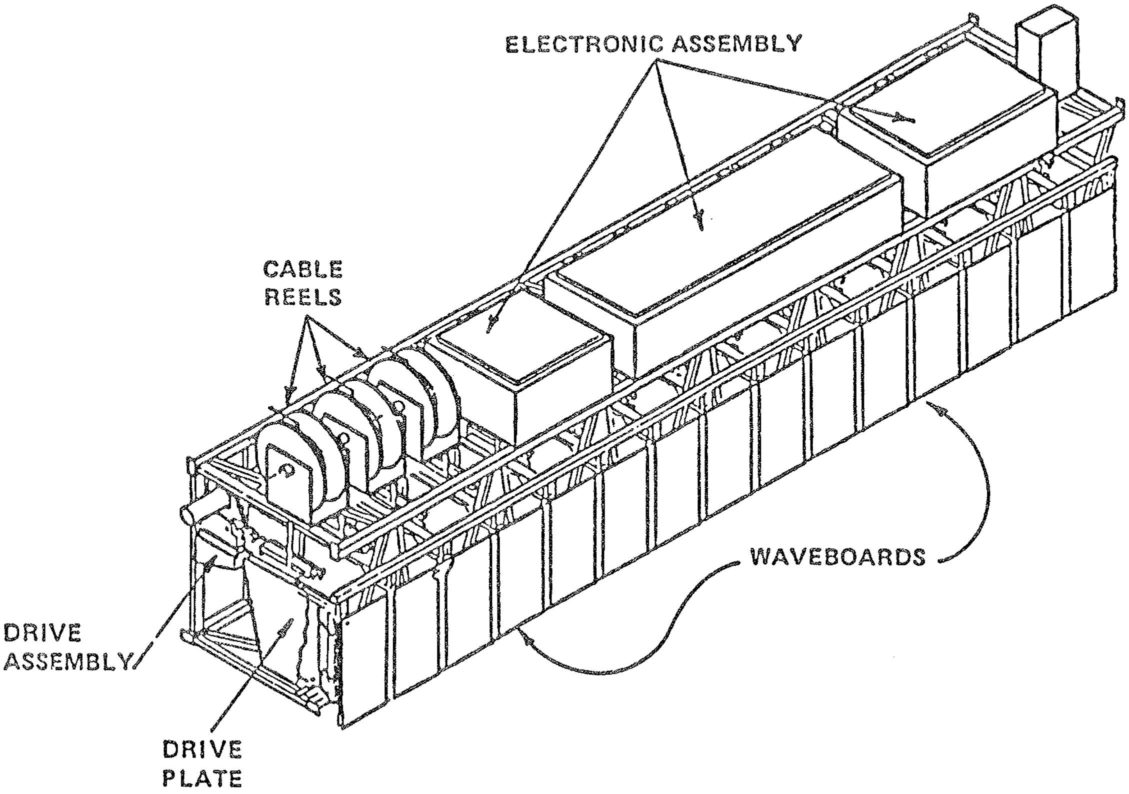

Figure 4.4 Schematic diagram of a wave generator module (Outlaw, 1984)

The maximum stroke of a wave board is 1.0 ft, corresponding to a +/- 0.5 ft displacement from the mid-point position. Each wave board can be operated up to and including 180 degrees out of phase with the adjacent board. As already noted, the boards are operated in a piston-like motion and are not sealed at the floor. The displacement of each paddle is controlled by a belt-driven carriage assembly connecting the drive assembly to the belt drive as shown in Figure 4.4. A transducer is located on each wave board to monitor displacement and provide a feedback signal to the wave generator console. The servo-controller module for each servo-motor monitors this position feedback and generates a stroke-limit and displacement-error detection signal which stops further displacement of the wave board if either limit is exceeded. The

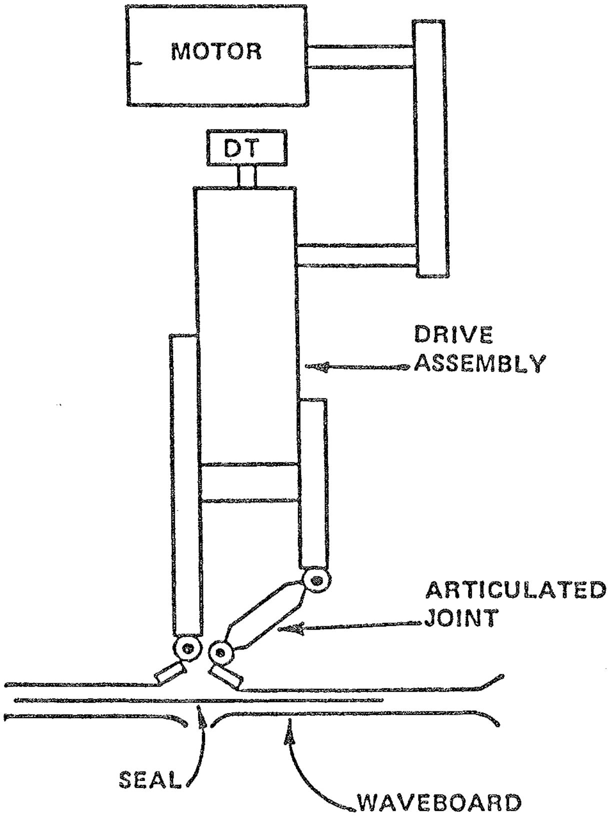

Figure 4.5 Schematic diagram of a wave board (Outlaw, 1984)

system console block diagram is shown in Figure 4.6 and the servo-controller block diagram is presented in Figure 4.7. Enclosures are mounted on the top of each module for containing the motor and transducer power and signal equipment. The cables required for the transmission of wave board displacement signals and the position transducer feedback signals are located on three cable reel assemblies adjacent to the equipment enclosures.

Each paddle of the four portable modules is electronically controlled and electromechanically operated according to the input command signal received from each associated control channel. This requires a total of 61 control channels corresponding to the push points

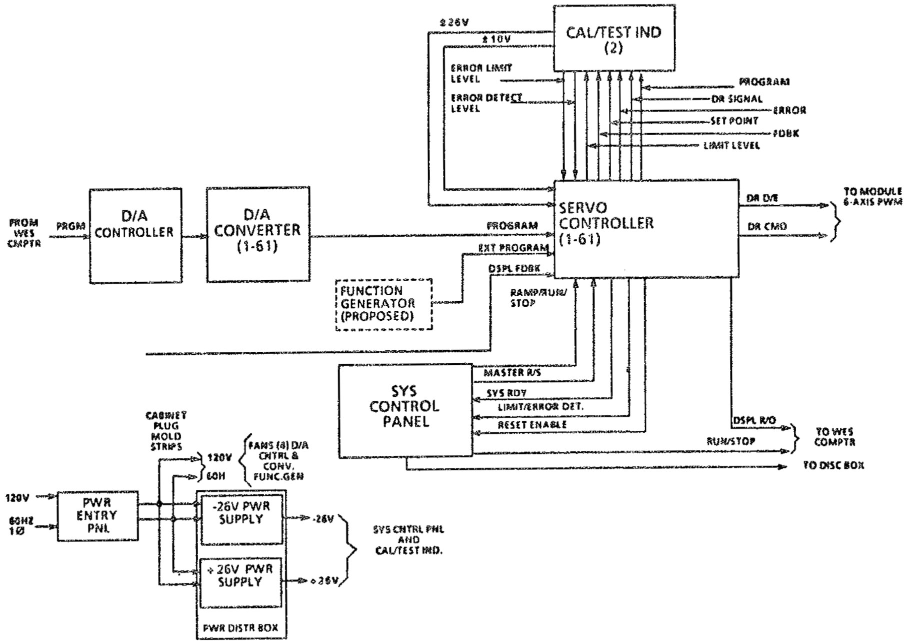

Figure 4.6 System console block diagram (Outlaw, 1984)

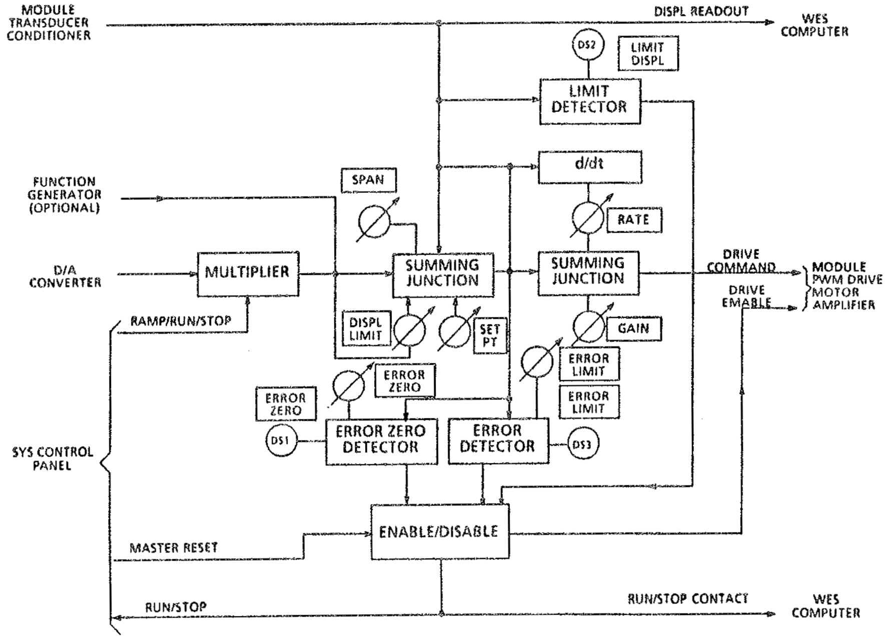

Figure 4.7 Servo-controller block diagram (Outlaw, 1984)

(articulated joints) for each of the 60 paddles (A single control channel provides the common signal for the joint between adjacent paddles). Independent control of each paddle in the system is provided by an Automated Data Acquisition and Control System (ADACS). The ADACS system was developed for the directional spectral generator through the modification of an existing control-feedback system (Whalin et al., 1974) reported by Durham and Greer (1976). This hardware/software interface allows the user a 20 update per second per wave board command control signal to the wave generator. This control capability is performed by the wave generator console which provides the digital to analog (D/A) conversion of the programmed signal such that 61 channels of control signal are simultaneously output to each of the 61 wave paddle servos. The sampling and storage of data at a rate of 50 samples per second per gage for up to 128 gages through multiplexed channels of analog to digital (A/D) conversion is provided by the system. The response of each wave board to the individual control signals is monitored so that when either the stroke or displacement limits have been exceeded, disable signals can be issued to the respective paddle. In addition, signals are provided to a calibration/test indicator located on the system console so that adjustments of the servo controllers can be made when necessary. Details of the system are reported by Turner and Durham (1984).

The computer system supporting the ADACS is a Digital Equipment Corporation (DEC) VAX 11/750 central processing unit (CPU). The system is equipped with an IEEE 448 interface for the D/A conversion of the user-supplied digital control signal. Peripherals to the basic CPU include 121 megabytes of fixed-disk mass storage, 10 megabytes of removable-disk mass storage, two 125 inch-per-second 800/1200 BPI magnetic tape drives, two line printers, a Versatec printer/plotter, and a Tektronix 4014 CRT unit equipped with hard-copy capabilities. The computer system is shown in Figure 4.8.

4.3 A Methodology for Generating Waves

Genus 2 solutions of the KP equation were shown in Chapter 3 to describe a three-dimensional, nonlinear wave pattern. The development of these solutions by Segur and Finkel was partially a consequence of experiments by Hammack (1980) which indicated qualitatively similar surface patterns resulting from the interaction of incident and reflected waves. A similar interpretation of genus 2 waves was presented in Chapter 3. The development of an experimental procedure which would result in the evolution of surface wave patterns qualitatively similar to genus 2 solutions was achieved by experimentally reproducing the conditions reported by Hammack, i.e. interacting waves. In view of this interpretation, the interacting wave trains used for the experiments were chosen to be cnoidal waves, since the periodic extension of a solitary wave is a cnoidal wave. This section will first describe the methodology used for generating cnoidal waves and then discuss the technique of evolving an appropriate wave form through the generation of simultaneously intersecting cnoidal wave trains. The indirect procedure of wave form evolution outlined here instead of the exact generation of genus 2 waves will be addressed at the end of this section.

4.3.1 The Generation of Cnoidal Waves

The generation of a cnoidal wave with the directional spectral wave generator is accomplished by utilizing the wave generation

Figure 4.8 The computer system

technique presented by Goring in 1978. Goring's method prescribes the displacement-time history required of a single piston wave generator to generate a long, permanent form wave. Because of the similarities in both the wave form and wave paddle motion, the generation approach is an ideal one for the present application. Therefore, the identical technique is used here to program the directional spectral wave generator with the added complexities of 60 paddles (with 61 push points) and provisions for phase lagging between adjacent paddles necessary for the subsequent generation of oblique waves. The basic theory is presented below.

Goring's wave generation methodology provides a means of relating the vertical displacement of the water surface profile of a known free wave to the horizontal wave paddle motion required to generate that wave. The principal idea is to equate the velocity of the paddle to the velocity beneath the wave surface at the location of the moving wave paddle. By knowing the time history of the desired free wave, the time history of the wave paddle motion necessary for generating that wave can be computed. Figure 4.9 was presented by Goring to demonstrate the way in which the generation equation is obtained.

The inset diagram (c) represents the desired water surface profile. In this example a linear sinusoidal surface displacement has been specified. The wave has an amplitude a and is propagating to the right with a wave celerity of c. The corresponding horizontal velocity time history is shown in the inset diagram (a). It can be seen that the velocity and surface time series are in phase, consistent with linear wave theory. Desired is the time history of the displacement of the wave paddle required to generate a sinusoidal wave. This desired

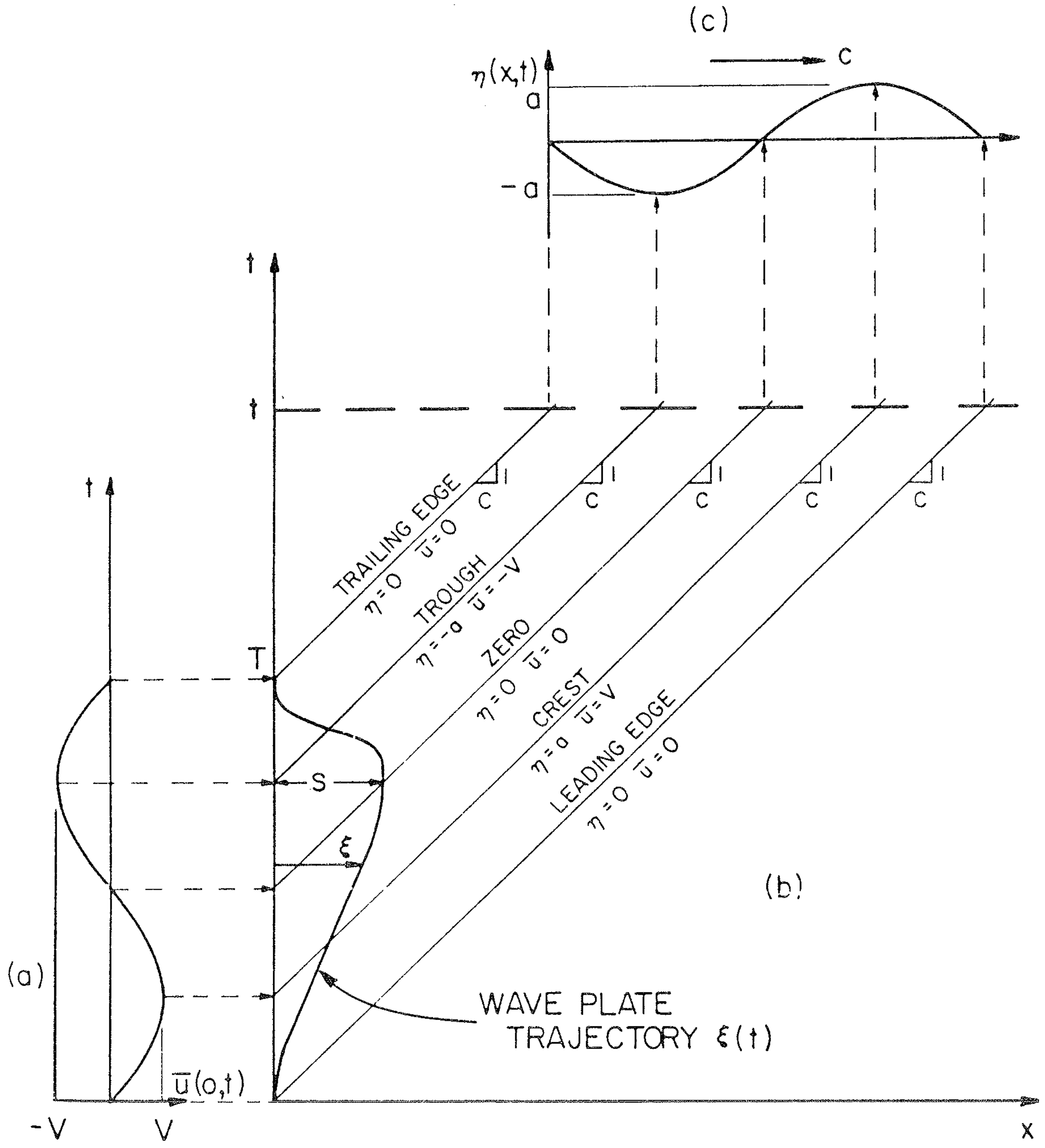

Figure 4.9 Wave generation phase plane (Goring, 1978)

displacement $\xi(t)$, termed the "trajectory" by Goring, is written in the following form,

$$\frac{d\xi(t)}{dt} = \bar{u}(\xi,t) \qquad 4.1$$

where $\bar{u}(\xi,t)$ represents the depth averaged velocity written as a function of the time varying trajectory of the wave board. Since we are dealing exclusively with long waves, the assumption is made that the particle velocity is constant throughout the water column.

The above representation for the velocity produces a distortion of the trajectory from what would be observed at a fixed location. For example, if $u(0,t)$ were used in Equation 4.1, the velocity would be only a function of time and the resulting trajectory would simply be sinusoidal in shape. The point of maximum trajectory, $\xi = S$, would occur at the time $t = T/2$. When the velocity representation of Equation 4.1 is used, the maximum trajectory is achieved at a time of $t = T/2 + S/c$. In Goring's words (1978) "Thus the time taken for the plate to travel forward to its full extent is time S/c longer than it would be if the trajectory were sinusoidal and consequently the time taken for the plate to travel back to its original is time S/c shorter than it would be if the trajectory were sinusoidal." Physically, if the wave paddle position is not considered, thereby ignoring the celerity of the wave, secondary waves will be produced at the wave generator paddle. This occurs because the crests and troughs, which are not traveling at the exact speed of the paddles, reflect off the paddles to produce the secondary wave effect.

For waves of permanent form it was shown (Svendsen, 1974) by continuity that the velocity averaged over the depth is

$$\bar{u}(x,t) = \frac{c\eta(x,t)}{h + \eta(x,t)} = \dot{\xi} \equiv \frac{d\xi}{dt} \qquad 4.2$$

where η represents the surface displacement. It is assumed that this displacement can be written in the following form:

$$\eta(\xi,t) = H\hat{f}(\hat{\theta}) \qquad 4.3$$

where H represents a wave amplitude and $\hat{f}(\hat{\theta})$ is the appropriate function (sinusoidal, cnoidal, etc.) of the phase variable

$$\hat{\theta} = k(ct - \xi) \ . \qquad 4.4$$

The total derivative of Equation 4.4 is written as

$$\frac{d\hat{\theta}}{dt} = k(c-\dot{\xi}) \ . \qquad 4.5$$

By using the chain rule, the time derivative on the right hand side can be written as follows:

$$\frac{d\xi}{dt} = \dot{\xi} = \frac{d\xi}{d\hat{\theta}} \cdot \frac{d\hat{\theta}}{dt} = \frac{d\xi}{d\hat{\theta}}\, k(c-\dot{\xi})$$

or

$$\frac{d\xi}{d\hat{\theta}} = \frac{\dot{\xi}}{k(c-\dot{\xi})} \quad . \tag{4.6}$$

By using the relationships of Equations 4.1, 4.2, and 4.3; Equation 4.6 can be simplified to the following

$$\frac{d\xi}{d\hat{\theta}} = \frac{H\hat{f}(\hat{\theta})}{kh} \quad .$$

Integration with respect to the phase variable yields

$$\xi(t) = \frac{H}{kh} \int_{o}^{\hat{\theta}} \hat{f}(w)dw \tag{4.7}$$

where w represents a dummy variable and the phase variable $\hat{\theta}$ is given by Equation 4.4. The resulting equation for the paddle trajectory is implicit in that the phase variable on the right hand side is also a function of the trajectory; therefore, the equation must be solved numerically. The solution technique selected by Goring was Newton's method, also referred to as the Newton-Raphson method. A general expression for this numerical procedure can be written for an arbitrary function F as a function of a phase variable $\hat{\theta}$ as

$$\hat{\theta}^{i+1} = \hat{\theta}^{i} - \frac{F(\hat{\theta}^{i})}{F_{\theta}(\hat{\theta}^{i})}$$

The superscript i represents the iteration number. The iterative procedure is to select an initial $\hat{\theta}^{i}$ and compute $\hat{\theta}^{i+1}$. This is repeated until the quantity $|\hat{\theta}^{i} - \hat{\theta}^{i+1}|$ is adequately small. The solution scheme is a rapidly convergent one for most well behaved functions and results in an accurate approximation for $\hat{\theta}$. The arbitrary function can be defined by writing the phase function of Equation 4.4 in the following identity.

$$F \equiv \hat{\theta} - k(ct - \xi) \equiv 0$$

Substitution of this identity into Equation 4.7 results in

$$F = \hat{\theta} - kct + \frac{H}{h} \int_{0}^{\hat{\theta}} \hat{f}(w)dw \ . \qquad 4.8$$

Now, the partial derivative with respect to the phase variable $\hat{\theta}$ yields the form

$$\frac{\partial F}{\partial \hat{\theta}} = F_{\hat{\theta}} = 1 + \frac{H}{h} \hat{f}(\hat{\theta}) \ . \tag{4.9}$$

Equations 4.8 and 4.9 are the precise form necessary for a Newton method solution for $\hat{\theta}$. Substitution yields the following solution for the phase variable at the $i+1$ iteration:

$$\hat{\theta}^{i+1} = \hat{\theta}^{i} - \frac{\hat{\theta}^{i} - kct + \frac{H}{h} \int_{0}^{\hat{\theta}} \hat{f}(w)dw}{1 + \frac{H}{h} \hat{f}(\hat{\theta})} \ . \tag{4.10}$$

The iteration of this relationship to the desired level of convergence will result in an accurate approximation for $\hat{\theta}$ at time t. Then, the paddle displacement can be determined by rewriting Equation 4.4 in the form

$$\xi = ct - \frac{\hat{\theta}}{k} \ .$$

Equation 4.10 represents an implicit solution method for the phase variable of an arbitrary wave form. We are now interested in the specific wave form of a cnoidal wave. The surface displacement function for a cnoidal wave can be written as

$$\hat{f}(\hat{\theta}) = \frac{y_t - h}{H} + cn^2(\hat{\theta}|m) \qquad 4.11$$

where h represents the depth of flow, y_t represents the distance from the wave trough to the bottom boundary, cn is the Jacobian elliptic function, m is the elliptic parameter, and

$$\hat{\theta} = 2k\left(\frac{t}{T} - \frac{\xi}{L}\right) \qquad 4.12$$

is the phase variable (the sign has been changed for convenience according to Goring's paper) written in terms of the first complete elliptic integral K(m), the wave period T, and the wavelength L. This form is exactly equivalent to that shown by Equation 2.2. The integral of this function, necessary for the evaluation of Equation 4.10, can be written in closed form (from Abramowitz and Stegun, 1970) as

$$\int_0^{\hat{\theta}} \hat{f}(w)dw = \frac{E(\hat{\theta}|m)}{m} - \frac{m_1\hat{\theta}}{m} \qquad 4.13$$

where $E(\hat{\theta}|m)$ is the second incomplete integral and m_1 is the complimentary elliptic parameter defined as

$$m_1 = 1 - m\ .$$

Substitution of Equations 4.11 and 4.13 into the Newton approximation results in the following relationship:

$$\hat{\theta}^{i+1} = \hat{\theta}^{i} - \frac{\frac{-2Kht}{T} + \left(y_t - \frac{Hm_1}{m}\right)\hat{\theta}^{i} + \frac{H}{m}E\left(\hat{\theta}^{i}\middle|m\right)}{y_t + H\,\mathrm{cn}^2\left(\hat{\theta}^{i}\middle|m\right)} \,. \qquad 4.14$$

Note that the negative sign in the first term of the numerator (-2Kht/T) was inadvertently omitted by Goring. A thorough description of the methods used to evaluate the various elliptic functions is provided in Appendix A. Upon completion of an adequate number of iterations to achieve the desired level of accuracy, the paddle displacement at time t can be written from Equation 4.12 as

$$\xi(t) = L\left(\frac{t}{T} - \frac{\hat{\theta}}{2K}\right) \,. \qquad 4.15$$

The programming of the wave generator to produce these displacements is accomplished in the following sequence of operations. Reference is now made to Figure A.1 in Appendix A. A wavelength and maximum water surface elevation is specified for each desired cnoidal wave. Based on this wavelength and wave elevation data, values for η_1, η_2, η_3, m_1, T, and the first K(m) and second E(m) complete and the second $E(\hat{\theta}|m)$ incomplete integrals are computed. The wave period is divided into 360 time segments corresponding to 361 discrete values (0-360). For each time value, the phase variable of Equation 4.12 is defined and used in the Newton iteration method to compute a displacement for the paddle corresponding to each of the 360 degree representations of the period. This procedure is repeated for each of the 61 push points of the 60 wave generator paddles. A magnetic tape is generated which contains the control signal for the displacement of each push point for the time series corresponding to a control signal update of 20 updates per second per paddle. The wave generator control software program is executed and the waves are produced on the wave generator corresponding to the input signal on the magnetic tape.

An example of the generated cnoidal waves can be seen in Figure 4.10 in which a single period of a cnoidal wave with a wavelength of 7.0 feet and a maximum wave height of 1.84 inches is shown. Discrepancies between theory and measurement are due to the variations in the basin topography as evidenced in Figure 4.2. This spatial variation in depth produces an approximate +/- 25% variation from the mean of the measured total wave heights for a cnoidal wave uniformly generated perpendicularly from the axis of the wave generator. This effect can be seen in the nine wave gage traces shown in Figure 4.11. The shoaling of the wave is obvious in the traces of gages 3, 6, and 7 which can be seen from Figure 4.2 to be located behind shallow areas. If these three gages are omitted, the variation is on the order of 14%. Fortunately, this shoaling effect is much less pronounced in the evolved waves which are used for verification of the KP equation. This is probably due to the fact that the test waves result from the nonlinear interaction of two separate waves generated from separate directions. The influence of the basin floor on the verification will be further addressed. The waves of interest, the candidate genus 2 waves, will now be discussed.

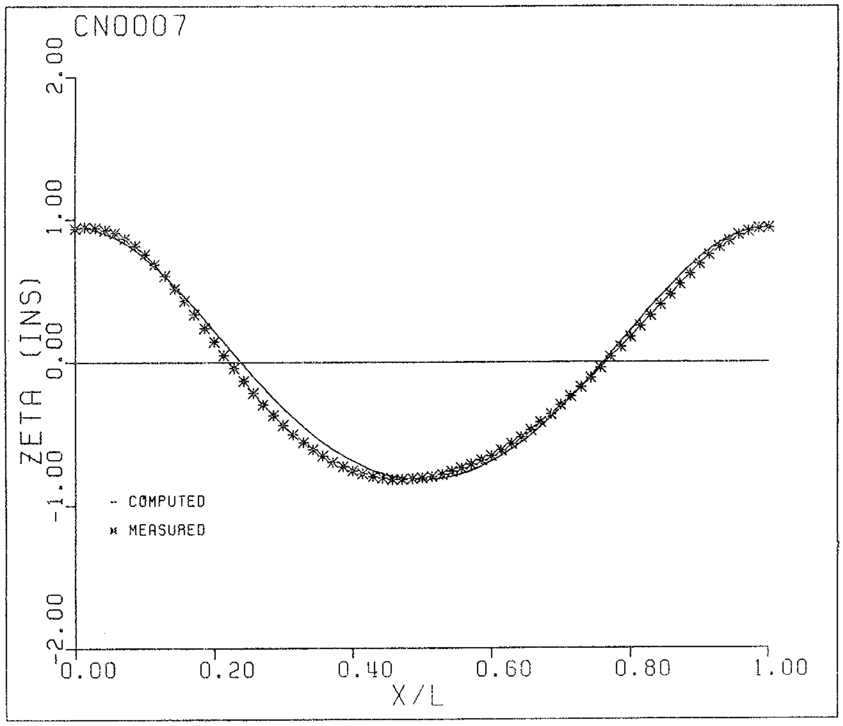

Figure 4.10 A comparison between a generated wave and cnoidal wave theory

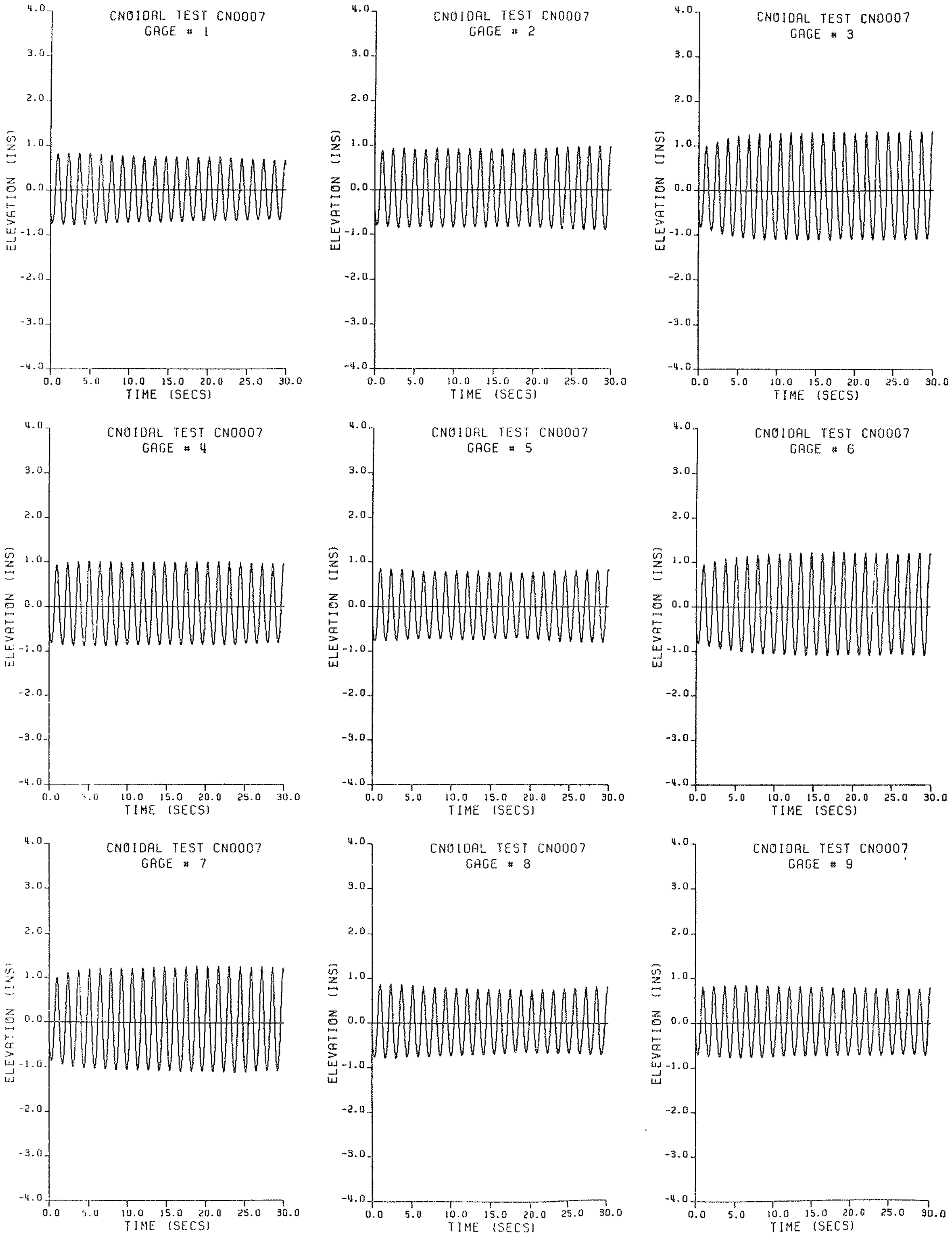

Figure 4.11 Wave profiles from the 9 wave gages for a uniformly generated cnoidal wave

4.3.2 The Generation of Genus 2 Waves

Genus 2 wave forms were produced in the wave basin by evolving the proper form rather than by directly generating it. The reason for this approach will be discussed at the end of this section. The evolution technique is as follows. The procedures described for generating cnoidal waves were modified such that a single cnoidal wave could be generated at an angle to the axis of the wave generator. A second wave was then simultaneously generated at an equal but negative angle such that the two separate waves are generated at a predetermined angle of intersection which is symmetric to the wave generator. In order to fully investigate the validity and limits of applicability of the KP equation as a model for three-dimensional nonlinear waves, an experimental program was devised to generate a variety of wave patterns which span a wide range of nonlinearity and three-dimensionality.

A broad range of nonlinearity of the basic wave shape is achieved by generating three basic cnoidal wave trains. These waves are generated with heights of approximately 1.0 inch and wavelengths of 7.0 ft, 11.0 ft, and 15.0 ft, corresponding to an elliptic parameter m of 0.44, 0.73, and 0.89 respectively. Water depth was maintained at 1.0 ft. Variations in the three-dimensionality of the resulting wave patterns was achieved by intersecting each of the three cnoidal wave trains at a variety of angles. These angles of intersection are obtained by programming a phase shift between adjacent wave paddles. A positive shift for one wave and a negative shift for the other wave results in the generation of the desired symmetrically intersecting waves. This phase shift is approximately equivalent to the angle of the wavecrest with respect to the axis of the generator. A wide range of angles of intersection were used in order to completely cover the range of weak to strong interaction of the two basic waves.

Twelve wave fields were selected for generation to test the KP equation. The generation components of each are shown on Table 4.1. The angle indicated in the table shows the approximate (linear wave relationship) correspondence between the phase shift and the angle of propagation.

Verification of the KP equation as a model for three-dimensional nonlinear waves will be successfully accomplished by reproducing the wave patterns indicated in Table 4.1 with exact solutions. Reproduction requires the development of a unique correspondence between the free parameters of the genus 2 solution and the physical characteristics of the observed wave field. Correspondence is developed in Chapter 5.

Table 4.1 The Experimental Waves

Test Number	Wavelength (ft)	Phase Shift (deg)	Angle (deg)	Period (sec)
CN1007	7.0	10.0	7.45	1.378
CN1507	7.0	15.0	11.21	1.378
CN2007	7.0	20.0	15.03	1.378
CN3007	7.0	30.0	22.89	1.378
CN4007	7.0	40.0	31.23	1.378
CN1011	11.0	10.0	11.75	1.947
CN1511	11.0	15.0	17.79	1.947
CN2011	11.0	20.0	24.04	1.947
CN3011	11.0	30.0	37.67	1.947
CN1015	15.0	10.0	16.12	2.553
CN1515	15.0	15.0	24.62	2.553
CN2015	15.0	20.0	33.75	2.553

Prior to addressing the free dynamical parameters of the exact solution, a comment on the generation technique utilized for this investigation is necessary. Waves were generated in the wave tank by evolving an approximate genus 2 wave as described above. This approach was first adopted because the relationship between the free parameters of the exact solution and the physical characteristics of the desired wave form were unknown at the onset of the investigation. For example, an appropriately shaped wave is first required in order to develop a means of relating the free solution parameters to that observed wave. These parameters could then be used to compute an exact solution which would emulate the observed wave. Following the successful completion of this task, the logical extension would be to generate the exact solution and analyze the resulting wave. This was in fact accomplished, but with disappointing results.

The finite dimensions of the 1.5 ft wide paddle proved to introduce strong perturbations in the small features of the resulting wave. An example result from experiment CN2015, described in Chapter 5, will be used here to illustrate this problem. The stem region of experimental wave CN2015 is on the order of 3.5 ft in length. It is physically impossible to generate this region exactly with 1.5 ft wide paddles. Examples of the perturbations introduced are shown in Figures 4.12 and 4.13. Figure 4.12 shows a wave trace in the saddle region for the evolved wave of experiment CN2015. Note the symmetrical peaks and uniform wave shape. An exact solution corresponding to this wave field was computed. Figure 4.13 demonstrates a similarly located wave trace for that generated exact solution. The perturbations are evident from the nonuniform shape of the resulting wave which actually evolves a third

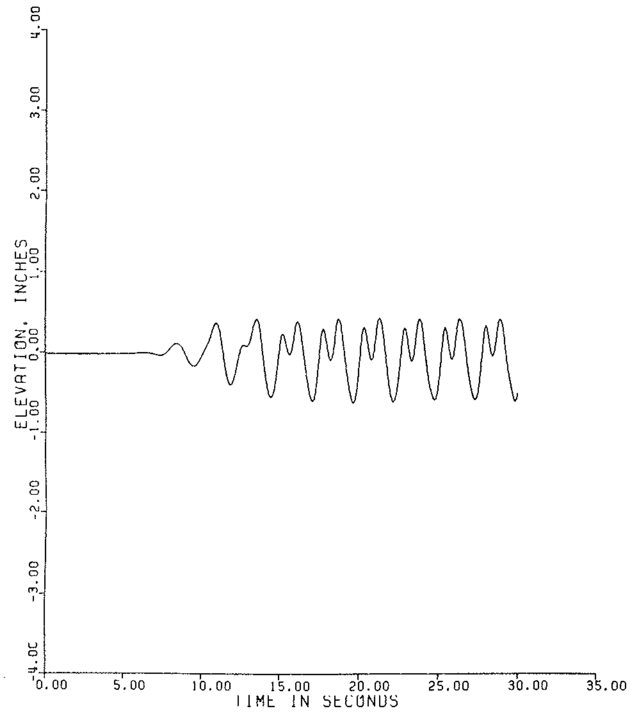

Figure 4.12 Measured wave profile in the saddle region of experiment CN2015

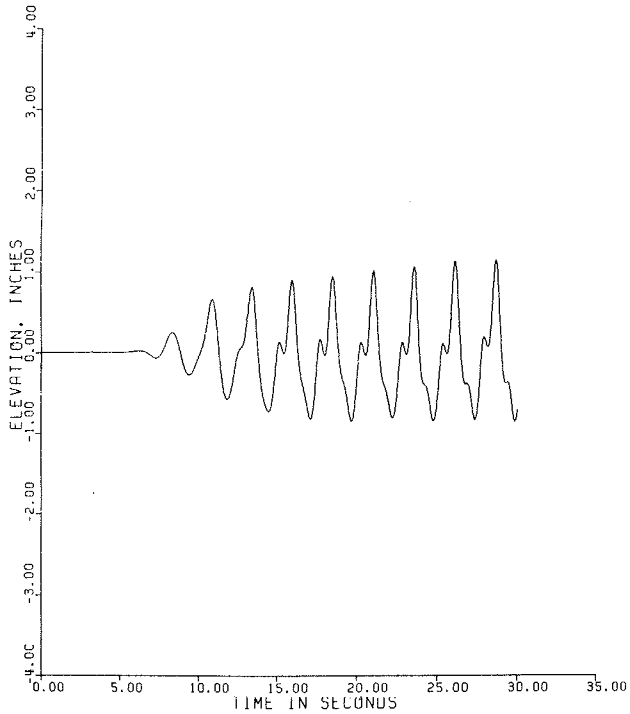

Figure 4.13 Measured wave profile in the saddle region corresponding to an exact solution generation of experiment CN2015

peak. Repeated attempts at generating exact waves always failed to generate a clean wave form. The conclusion of this exercise was that a relatively clean genus 2 wave could be continuously evolved but could not be discretely generated by existing facilities.

4.4 The Measurement of Waves

The difficulty of quantifying three-dimensional wave phenomena with two-dimensional instrumentation is well recognized. Furthermore, the presentation of two-dimensional data in a concise yet definitive form for effectively demonstrating three-dimensional effects is difficult. The measurement program developed here can best be motivated by looking at the basic features of the generated waves. Figure 3.3 shows a typical wave form produced by the technique described above. Symmetry of the wave pattern was achieved by generating identical cnoidal waves (equal wavelength and height) at symmetric angles. The period parallelogram, discussed in Chapter 3 and shown in Figure 3.4, was described as a basic surface pattern which repeats to form a global surface wave field. The complete specification of this area will define the surface pattern and be sufficient for verification of the KP solution. The basis for choosing symmetric waves can now be seen, a symmetric period parallelogram is generated which propagates in a direction perpendicular to the axis of the wave generator.

Two separate means of data collection were used to quantitatively measure the parameters of the basic parallelogram. First, a photographic technique was devised to measure the spatial distribution of the generated wave field. Photographs provided a visual representation of both the physical size of the resulting period parallelograms and of the internal features, such as the stem and saddle regions. These data were used to determine the placement and spacing of a single fixed linear array of recording wave gages which would be capable of quantifying the vertical, horizontal, and temporal distribution of each of the period parallelograms. These two collection techniques are described below.

4.4.1 The Photographic System

Measurement of the two-dimensional geometry of the surface wave patterns was found to be highly beneficial in that it provided both quantitative and qualitative information on the spatial structure of the period parallelogram. This procedures is described. Two Hasselblad Model 500 EL/M 70mm cameras were each equipped with a 50 mm lens, an automatic advance 50 exposure film canister, and a remote control exposure capability. The two cameras were installed approximately 23.0 feet above the floor of the wave basin, located on either end of an approximately 20.0 foot long 3 X 5 inch aluminum box beam which was clamped to an existing catwalk and cantilevered out over the wave basin. This procedure resulted in a final placement of the cameras centered on the wave generator a distance of 40.0 feet from the axis of the wave boards. Because of the focal length of the lenses, the field of vision of each cameras was approximately 23 X 23 feet. The resulting two photographs could then be combined in a mosaic to form a 23 X 40 foot picture. Illumination of the basin area beneath the cameras was by means of 2 Ascor, 8000 watt-second strobe lights with remote control activation capability.

Both cameras and strobes were connected to a remote control activation panel which, when activated, operated both simultaneously. The control panel was located adjacent to the wave generator console in the computer room. A single gage was centrally placed 55.0 feet from the wave generator, beyond the viewing range of the cameras. A schematic diagram of the photographic setup is shown in Figure 4.14. Gage output was monitored with a Tektronix Model 5111A dual trace oscilloscope, also located adjacent to the generator console, to provide the operator with a means of determining when to activate the cameras and strobes. It was assumed that when the wave front first became visible on the oscilloscope screen, the wave field would be fully developed in the camera viewing area. A photograph was taken at this time followed by four more at approximately 5.0 second intervals. This procedure was used for all experimental wave patterns. A total of 240 photographs, representing 120 mosaics, of surface wave patterns were taken for the study. A representative photograph of each wave pattern used for analysis is included in Appendix B.

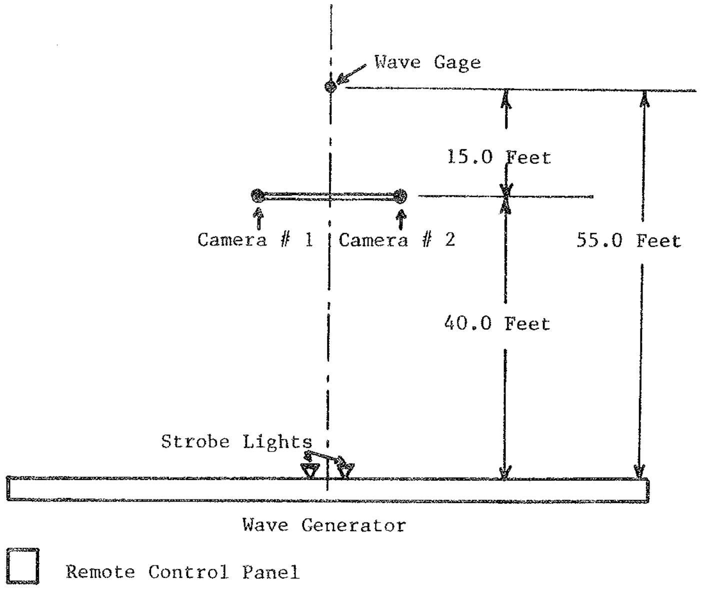

Figure 4.14 The photographic system

The photographic technique described above proved to be an invaluable tool for understanding and interpreting the qualitative features of the generated wave fields. Without the aid of these photographs, the successful formulation of a data collection program would have been extremely difficult.

A problem which exists with photographic data is that of distortion. Although the photographs were primarily used in a qualitative sense, this problem is addressed here. Horizontal measurements from the photographs are based on grid marks painted on the basin floor for that purpose. Since the waves are actually photographed on the surface (one foot above the bottom), a discrepancy between actual and measured distances is experienced which increases with distance from the camera lens. An example is shown in Figure 4.15 to illustrate this effect.

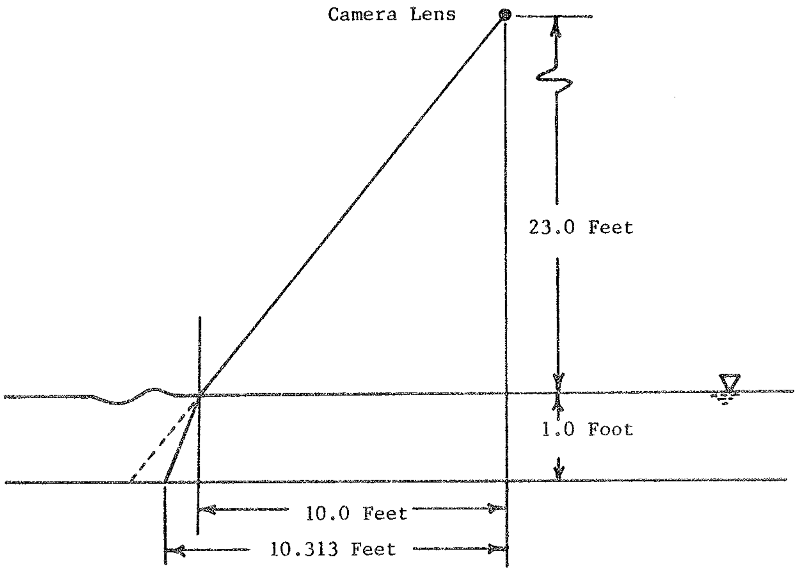

Figure 4.15 Horizontal measurement distortion

Assume a wave crest is photographed which is actually 23.0 feet below and 10.0 feet from the camera. Due to the diffraction of light (assuming an index of refraction of 1.3330) a distance of 10.313 feet will be measured from the floor scale. This amounts to an error of 3% in 10 feet (6% for the entire viewing area). Directly under the camera, the error is zero. Because of this variable horizontal discrepancy, error limits for horizontal measurements were determined. These limits will be further addressed in Chapter 5.

4.4.2 The Wave Gages

The second set of required data are quantitative water surface elevations which will relate the vertical structure of the observed waves to the exact genus 2 solutions of the KP equation. These data were used to quantify certain wave characteristics, such as the horizontal variation in height and shape within the period parallelogram. Measurement of the required three-dimensional distribution of the wave field was greatly simplified by the selection of the symmetrically intersecting waves. As previously mentioned, the resulting permanent wave form, bounded by the basic period parallelogram, propagates perpendicular to the face of the wave generator. The period of the generated wave is easily measured with wave gages and the width of the period parallelogram is measured from the photographs. These two data determine the propagating velocity of the permanent-form wavefield. By knowing the period and velocity, a time series measured from a stationary gage for one period can easily be converted to a spatial water surface distribution across one horizontal wavelength.

The simplification achieved by symmetry can now be demonstrated. As can be seen in the schematic of Figure 3.4, the axis of the stem region of interaction is parallel to the face of the wave generator. An array of nine recording wave gages was located in the wave basin parallel to this same line. The gages were placed a distance of 40.0 feet from the face of the wave generator, spaced 2.5 feet apart. The entire array was centered on the generator such that gages 1 and 9 were each 10.0 feet from the generator centerline as shown in Figures 4.1 and 4.2. The placement of these gages with respect to the hexagonal wave forms and period parallelograms is shown in Figure 4.16.

The sample wave pattern shown graphically now demonstrates the advantages of generating symmetrical waves. For example, it can be seen that a common point exists in the center of each hexagonal figure which represents the common apex of two period parallelograms. It can be seen that the location of each gage can be uniquely identified within a half

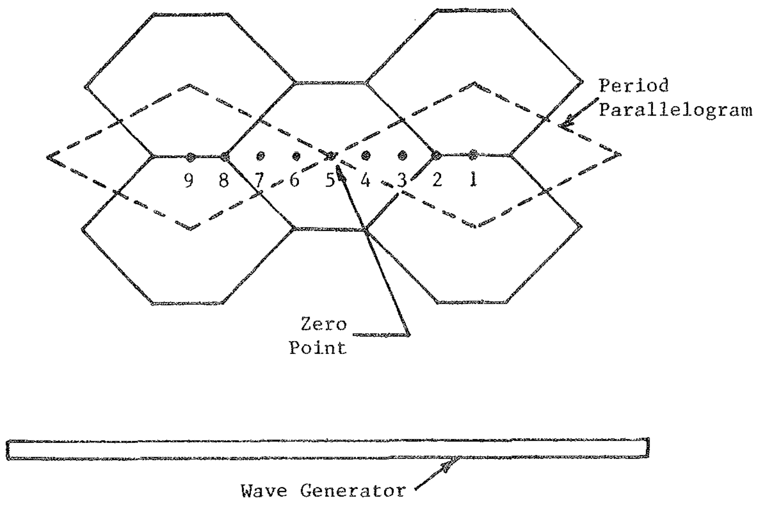

Figure 4.16 Schematic diagram for wave gage placement

parallelogram by referencing it according to its distance from the common, or zero point. Because of the symmetry, the left half of the right parallelogram is exactly equivalent to the right half of the left parallelogram. The determination of just one half parallelogram is then sufficient to completely describe the entire period parallelogram and hence the entire global wave field. The data collection scheme was specifically aimed at this goal by mapping each of the nine gages into a common half period parallelogram. In the example shown; gages 6 and 4, 7 and 3, 8 and 2, and 9 and 1 are equivalent since each pair are equidistant from the zero point. Since the actual location of that point with respect to the gage line axis varies for each test run, the first estimated relationships between the zero point and the gage locations were determined from the mosaic photographs. Subsequent adjustments were made by shifting the solution origin by varying ψ_{10} and ψ_{20} of Equations 3.49. An example of the gage-zero point correspondence will be presented in Chapter 5.

The water level gages used for this study are water-surface-piercing, parallel-rod, conductance type gages. They are identical to those for which the original ADACS was developed. Use of the gages made it possible to utilize existing calibration, storage, and plotting software. Each gage is associated with a Wheatstone bridge, shown schematically in Figure 4.17. Operationally, a transducer measures the conductance of the water between the two vertically mounted parallel rods. This measured conductance is directly proportional to the depth of submergence of the rods. The output from each gage is sent to the ADACS through shielded cables. The accuracy of the gages was reported

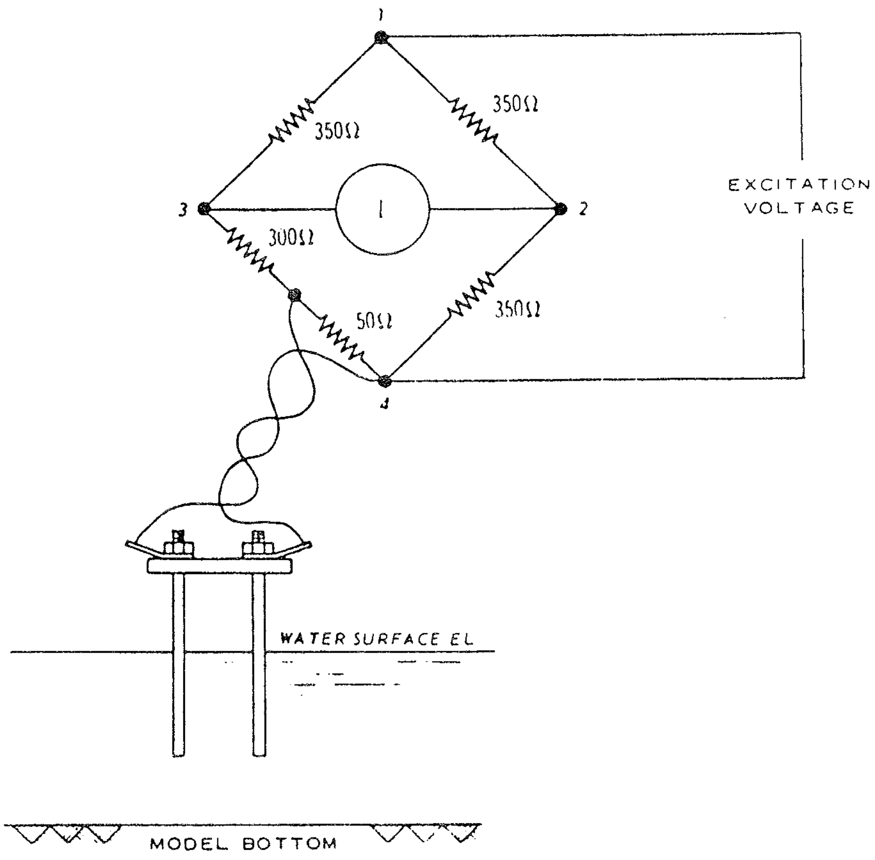

Figure 4.17 Schematic diagram of parallel-rod resistance transducer (Durham and Greer, 1976)

by Durham and Greer (1976) to be within 0.001 ft. A typical wave gage is shown in Figure 4.18.

The actual process of taking data was based on the procedures developed and the software written for the ADACS described in Section 4.3. The operational steps are as follows.

Each wave gage is calibrated prior to the generation of waves. The calibration process entails the monitoring of the output voltages from the linear-position potentiometer located on each gage. This is accomplished by system software/hardware interfacings which move each parallel rod sensor into and out of the water a known distance. Each sensor is systematically moved to 11 quasi-equally spaced (within the practical limits of the gear-train driven electric motor) locations over a user specified range. During this movement, 21 voltage samples are taken from which an average value for each of the 11 locations are computed. A schematic diagram of the calibration process is shown in Figure 4.19. The averaged 11 values for each gage are fitted to a least squares linear fit to determine the calibration curve. If the maximum deviation from this linear fit exceeds a user-specified tolerance, a quadratic fit is performed. A cubic spline can be applied if the quadratic fit is outside tolerances. The final resulting calibration curve relating voltages to water surface displacements for each gage is then stored in disk memory for later use by system software.

The control signal for a desired wave combination is used to generate an experimental wave field. The location of the wave front in the basin is determined by the operator by simply monitoring the output of any two of the nine gages with the dual channel oscilloscope. When it has been determined that the wave field is fully developed at the

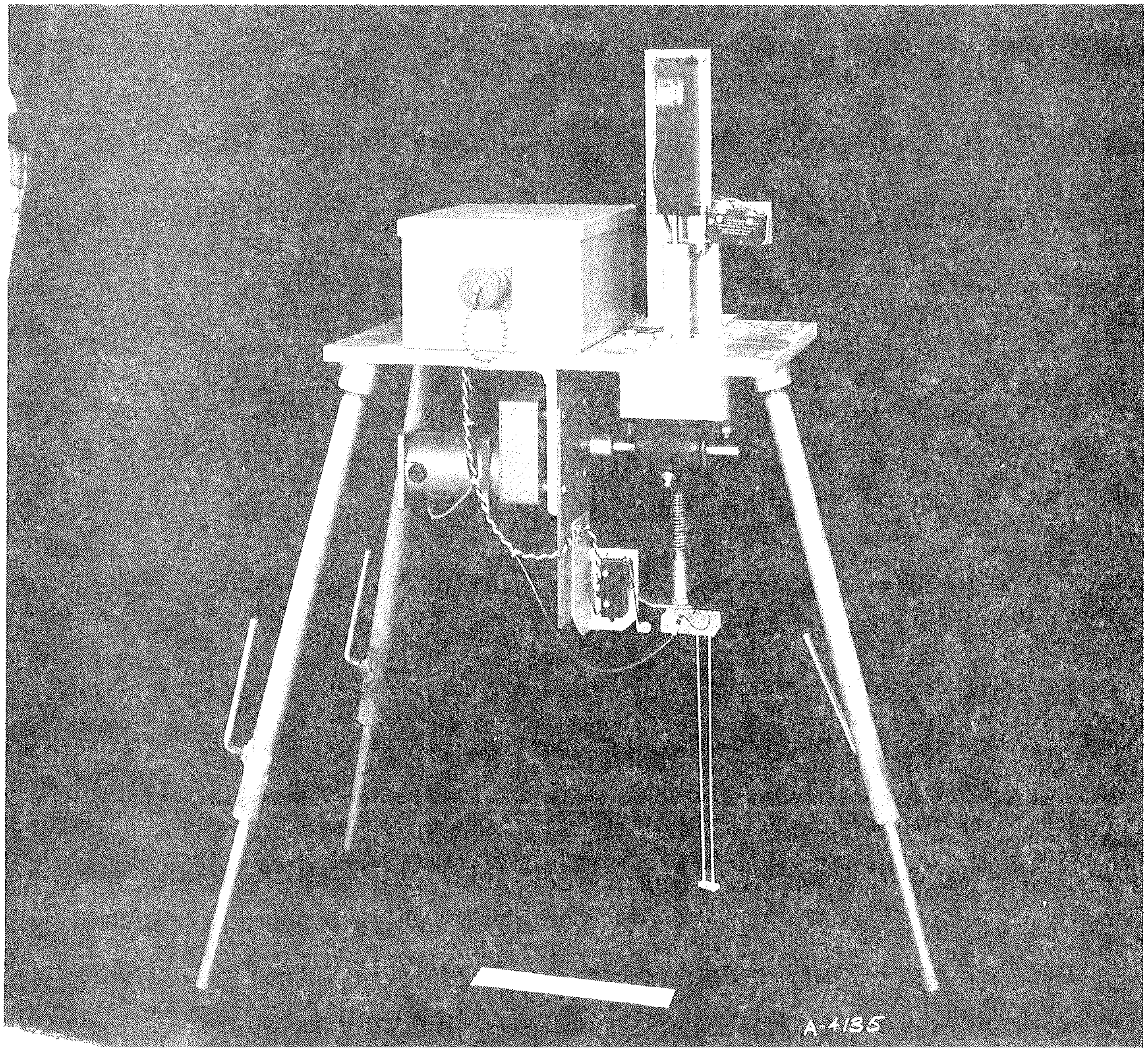

Figure 4.18 Parallel-rod wave sensor

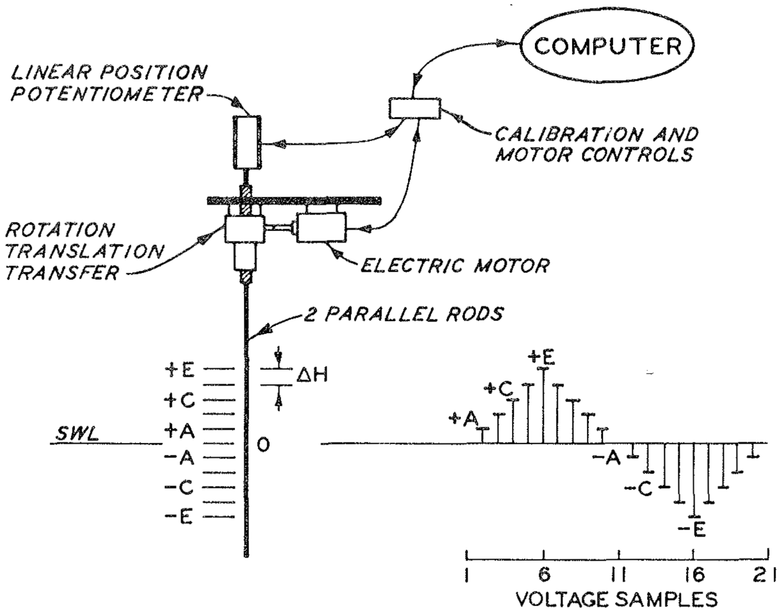

Figure 4.19 Waverod calibration (Turner and Durham, 1984)

array of wave gages, the operator initiates the sampling of data. Sampling extends for a user-specified period of time. The data, along with the corresponding calibration curves, are stored on disk. The time series for each gage is automatically plotted on a Versatec printer/ plotter and written into disk storage for subsequent analysis. The length of data sampling used for this study was 30.0 seconds. With a sampling rate of 50 samples per second, 13500 data points were collected and stored for all nine gages for each experimental wave.

The data collected for this project are presented graphically in Appendix B. The results of the verification of the KP equation to the 12 generated wave fields are presented in Chapter 5.

CHAPTER 5

A COMPARISON OF GENUS 2 THEORY WITH EXPERIMENTAL WAVES

This chapter relates the exact genus 2 solutions of the KP equation described in Chapter 3 to the wave characteristics measured in the twelve laboratory experiments described in Chapter 4. The development of this relationship requires the detailed assessment of the free parameters in the solution. In particular, insight into the sensitivity of the solution to each of these free parameters must be established since the spatial and temporal features of the solution are linked nonlinearily to these parameters. Once a basic understanding of the coupling between parameters is established, a methodology is developed for selecting and optimizing the solution such that a "best-fit" to measured data is achieved. The quantitative assessment of the comparisons between best-fit genus 2 waves and measured data for each of the twelve experiments of Table 4.1 will demonstrate the capability of the KP equation to model a wide range of laboratory-generated wave phenomena.

5.1 The Free Parameters of a Genus 2 Solution

The calculation of a general genus 2 solution of the KP equation requires the specification of six dynamical parameters and two nondynamical parameters. (These parameters were noted in Section 3.4.) The experimental program described in Sections 4.3 and 4.5.2 employs symmetrical waves in order to evolve a period parallelogram which is symmetric about both the x- and y-axis as was shown in Figures 3.4 and 4.16. A symmetrical parallelogram was desirable so that a fixed linear wave gage array could be used to measure all experimental waves. Symmetry introduces the following relations:

$$\mu_1 = \mu_2 \equiv \mu, \ \nu_1 = -\nu_2 \equiv \nu, \ \omega_1 = \omega_2 \equiv \omega \qquad 5.1$$

Hence, the number of free parameters for the symmetric subset of solutions is reduced to five, with only three of dynamical significance. These three free parameters are truly independent and can be arbitrarily selected from the nine dynamical parameters of the general genus 2 solution. The remaining six dependent parameters are computed from Dubrovin's theorem of Equation 3.66 and the relationships shown in Equations 5.1. The free parameters chosen for this investigation are b, μ, and λ. These were selected because their specification resulted in a rapidly convergent algorithm for computing a best-fit with measured data. The algorithm consists of an interactive program which was specifically developed to compare computed and measured wave characteristics. In order to gain insight into the effects of changing parameter values, a sensitivity analysis is made to demonstrate the impact of each of the independent free parameters on the computed waves.

In each of the following analyses, two of the independent variables are held fixed while the third is allowed to vary. The relative effect of the single parameter is then measured by changes in the nondimensional maximum computed wave elevation fmax, the angular frequency

ω, and the y-direction wavenumber ν. These parameters were selected because their values yield the measurable quantities of maximum wave elevation, period, and y-dimension length of the period parallelogram.

5.1.1 Sensitivity analysis for the parameter b

As already noted in Section 3.4, the parameter b provides a measure of the nonlinearity of the wave field. There it was shown that for $b \to 0$ the waves appeared as two KdV solitons whose interactions were highly localized in space. For b more negative, the wave heights decrease and a wave profile measured through the stem region becomes more sinusoidal. More detailed insight into the effects of b on the genus 2 waves is provided in Figure 5.1 which shows the effects of varying b on ω, fmax, and ν when λ and μ are fixed. It can be seen from Figure 5.1 that a 3-fold increase in b (-6. to -2.) produces a

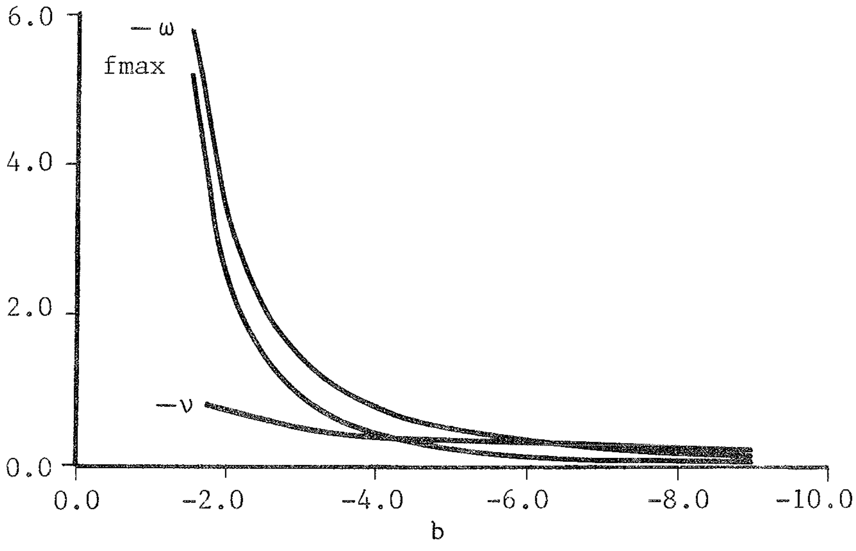

Figure 5.1 Sensitivity of the parameters ω , fmax , and ν to the parameter b

21-fold increase in the nondimensional maximum wave elevation (0.116 to 2.522). A comparable change in the angular frequency occurs while the value of ν is not affected significantly. The effect on ω is due to nonlinear changes in wave speed through the dispersion relation and the fact that the x-direction wavelength is fixed in the computation. The value of b can therefore be seen to be indicative of nonlinearity, somewhat equivalent to the elliptic parameter m of cnoidal theory. A qualitative demonstration of the relative effect of b on the wave shape can be seen in the normalized three-dimensional plots shown in Figures 5.2a and 5.2b. In the first case, the waves are seen to be highly nonlinear in shape while the waves are smoother and appear to be more linear in the second case.

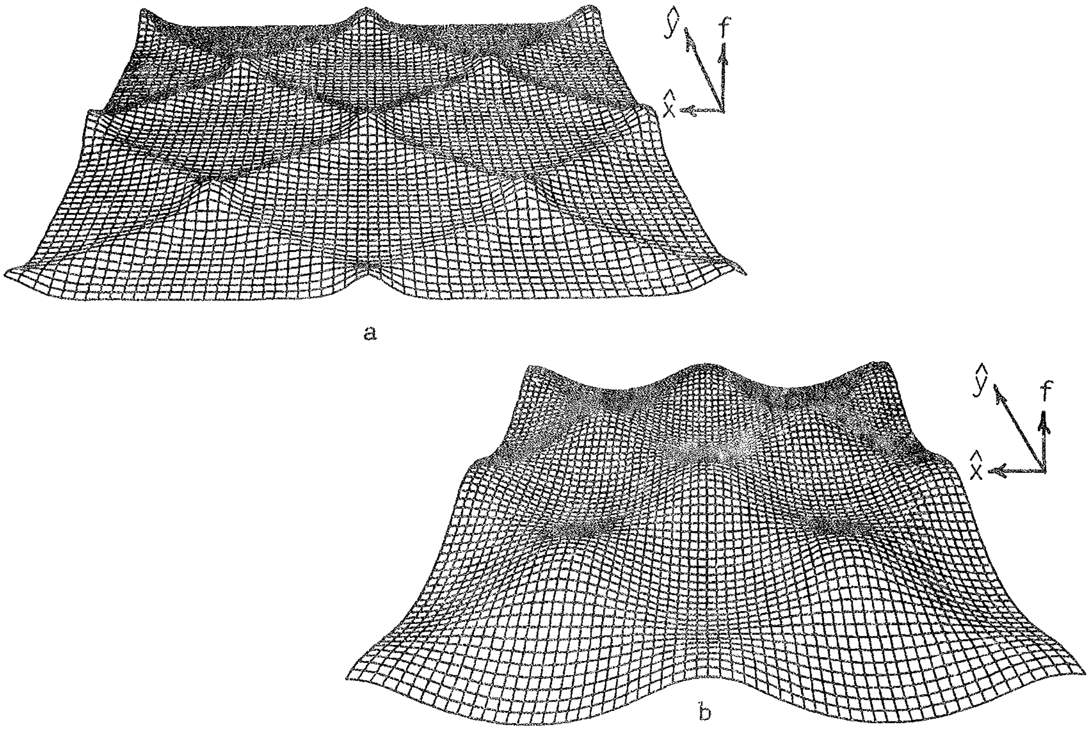

Figure 5.2 Example wavefields demonstrating the effect of the parameter b with λ =0.100 and μ =0.500
a) b = -2.000, ν = -0.629, fmax = 2.552, ω = -3.197
b) b = -6.000, ν = -0.277, fmax = 0.116, ω = -0.350

5.1.2 Sensitivity analysis for the parameter μ

The effect of the parameter μ is illustrated in Figure 5.3 which shows the variation of ω, fmax, and ν over a range of $0.2 \leq \mu \leq 0.9$. It can be seen that the frequency and, to a lesser extent, the wave height are sensitive to variations in μ. For example, an increase in μ decreases the x-direction wavelength over which the wave must travel. This results in a decrease of the period or increase of the angular frequency of the wave with respect to a coordinate system translating at the speed of a linear wave. This is shown in Figure 5.3. The total effect of these coupled changes are manifest in the maximum wave elevation shown in the figure. As with the parameter b, little effect is shown in the value of ν. Figures 5.4a and 5.4b qualitatively demonstrate the effect of μ to be a somewhat minor alteration of the shape of the period parallelogram. The most significant effect is not obvious from the three-dimensional plots, a 100% increase in μ (0.400 to

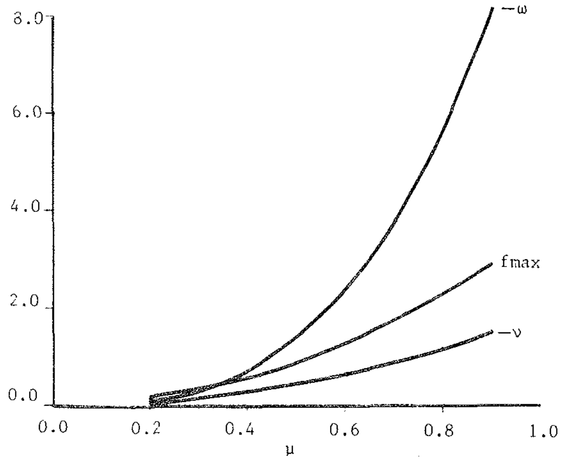

Figure 5.3 Sensitivity of the parameters ω, fmax, and ν to the parameter μ

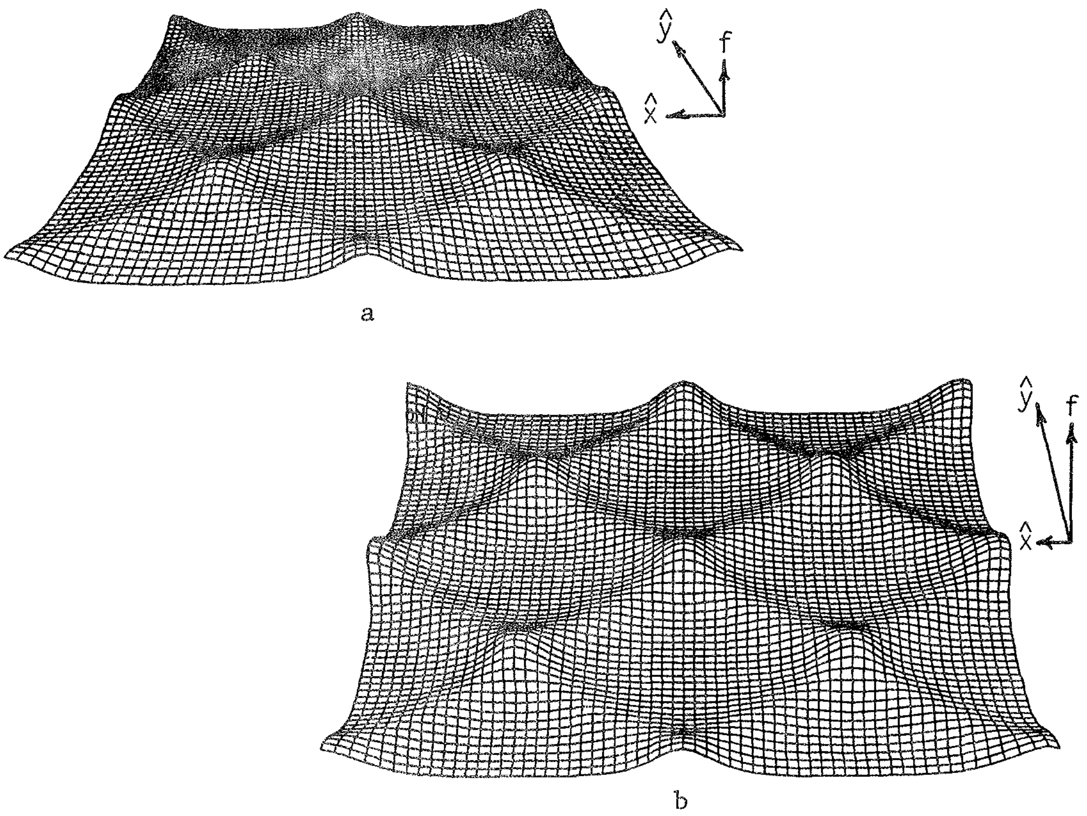

Figure 5.4 Example wavefields demonstrating the effect of the parameter μ with $b = -3.000$ and $\lambda = 0.100$
a) $\mu = 0.400$, $\nu = -0.291$, fmax = 0.572, $\omega = -0.713$
b) $\mu = 0.800$, $\nu = -1.163$, fmax = 2.286, $\omega = -5.705$

0.800) produces an 800% change in ω. However, the large change in ω is somewhat misleading since the frequency passes through zero as the wave celerity increases from less than to greater than the linear wave celerity. It can be seen that μ is primarily a measure of wave period and secondarily a measure of wave height.

5.1.3 Sensitivity analysis for the parameter λ

The effect of λ is evidenced in all parameters (ω, fmax, and ν) as shown in Figure 5.5. The most effective demonstration of its relative effect on the solution is seen in the qualitative features

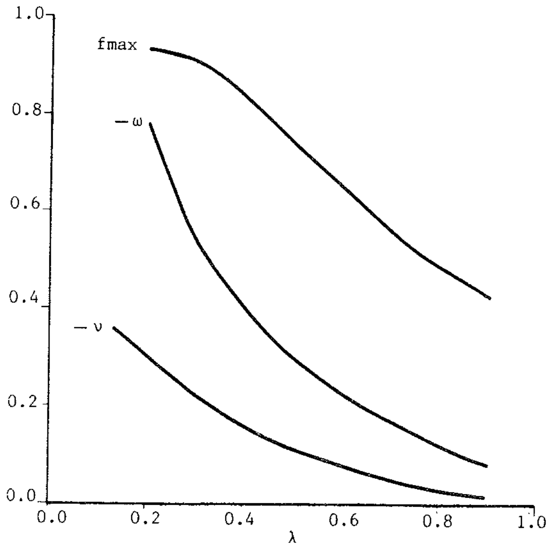

Figure 5.5 Sensitivity of the parameters ω, fmax, and ν to the parameter λ

evident in Figures 5.6a and 5.6b. In the first case, the saddle region is long, resulting in a short stem of interaction. This is an indication of weak interaction between the two waves. The second figure shows a much stronger degree of interaction as seen by the long stem and large angle between the saddle region and the stem axis. From the point of view of intersecting waves, this interaction is so strong that the original waves have completely lost their identity. The entire wave pattern is now represented by propagating stems with almost no saddle region in between. Note that Figure 5.5 and 5.6b include values of λ outside the allowable range of 0.5 according to Segur and Finkel for a Riemann matrix to be basic according to the definition of Equations 3.55. These values were included to demonstrate the effect of the parameter on the qualitative features of the solution. The observed effects provide an indication of the strength and magnitude of the phase shift experienced by the wavecrests of the original component waves.

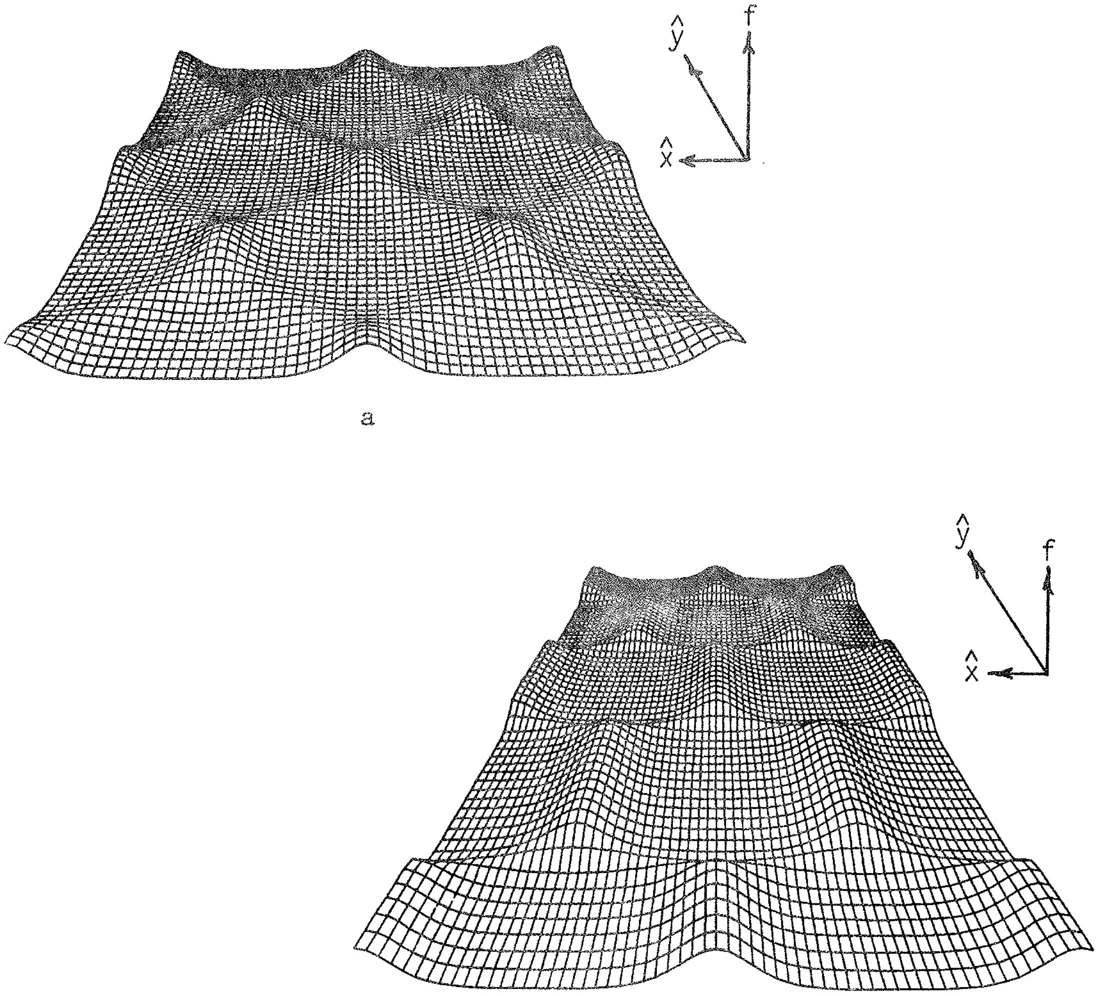

a

b

Figure 5.6 Example wavefields demonstrating the effect of the parameter λ with $b = -3.000$ and $\mu = 0.500$
a) $\lambda = 0.300$, $\nu = -0.218$, fmax = 0.908, $\omega = -0.541$
b) $\lambda = 0.800$, $\nu = -0.032$, fmax = 0.492, $\omega = -0.121$

5.2 The Dimensional Genus 2 KP Solution

The comparison of exact KP solutions to laboratory generated data requires the use of the scaling presented in Chapter 3 for relating the nondimensional KP parameters to their dimensional laboratory counterparts. The nondimensional variables $\hat{x}$, $\hat{y}$, f, and $\hat{t}$ are related to the dimensional variables $\tilde{x}$, $\tilde{y}$, ζ, and $\tilde{t}$ according to

$$\hat{x} = \frac{\varepsilon^{1/2}}{h} (\tilde{x} - \sqrt{gh}\, \tilde{t})$$

$$\hat{y} = \frac{\varepsilon \tilde{y}}{h}$$

$$f = \frac{3}{2\varepsilon h} \zeta \qquad 5.2$$

$$\hat{t} = \frac{\varepsilon^{3/2} \sqrt{gh}\, \tilde{t}}{6}$$

Use of the velocity potential results in the following relationships describing the three-dimensional velocity field:

$$u = \sqrt{g/h}\, \zeta$$

$$v = \sqrt{g/h} \int \zeta_{\tilde{y}} d\tilde{x}$$

$$w = - \sqrt{g/h}\, (h + \zeta)\zeta_{\tilde{x}} \ . \qquad 5.3$$

The nondimensional wave numbers (μ, ν) can be written in terms of dimensional wavelengths according to

$$\mu = \frac{2\pi h}{\varepsilon^{1/2} L_x}$$

$$\nu = \frac{2\pi h}{\varepsilon L_y} \qquad 5.4$$

where L_x and L_y represent the $\tilde{x}$ and $\tilde{y}$ dimensions of the observed period parallelogram. The maximum observed wave elveation ζ_{max} is related to fmax through the relationship:

$$\zeta_{max} = \frac{2}{3} \varepsilon h f_{max} \; . \tag{5.5}$$

The small parameter ε appearing in Equation 5.5 was used for ordering terms in the derivation of the KP equation. The numerical value of the parameter is arbitrary and can be set to unity without loss of generality. By specifying ε as unity and noting that a water depth of 1.0 foot was used for all experiments, it can be seen that the dimensional and nondimensional wavelengths are numerically equivalent.

The dimensional wave period measured in laboratory coordinates can be written in terms of the nondimensional solution by examining the phase variable in Equation 3.49. For example, the nondimensional phase

$$\psi = \mu\hat{x} + \nu\hat{y} + \omega\hat{t}$$

can be written in terms of dimensional quantities according to

$$\psi = \frac{\mu\tilde{x}}{h} + \frac{\nu\tilde{y}}{h} + \left(\frac{-\mu\sqrt{gh}}{h} + \frac{\omega\sqrt{gh}}{6h}\right)\tilde{t} \tag{5.6}$$

where μ and ω are KP values. The quantity in brackets represents the dimensional angular frequency and can be used to define the dimensional wave period in terms of the KP values μ and ω.

$$T = \frac{2\pi}{\sqrt{g/h}} \Big/ \left(\frac{\omega}{6} - \mu\right) \tag{5.7}$$

Equations 5.4 through 5.7 provide the relationship between laboratory quantities and solution parameters. These relationships will be utilized in the following section for obtaining a best-fit genus 2 solution for each of the experiments.

5.3 A Methodology for Relating Genus 2 Solutions to Observed Waves

The algorithm developed to relate the free parameters of the genus 2 solution to the observed wavefield is an iterative procedure based on the sensitivity analysis of section 5.1 and the laboratory data measured in the experiments. The algorithm will be described in detail using experiment CN3007 from Table 4.1 as an illustrative example.

The wave field corresponding to case CN3007 was generated using the technique described previously in Chapter 4. Wave gages located in the stem region indicate the period parallelogram has a period approximately equal to 1.378 seconds as was used to program the wave generator. This period is the most accurate information known describing the evolved wave pattern since it was independently computed by system software from the calibrated wave gage data. Overhead photographs were taken to form a mosaic of the wave field. The mosaic for experiment CN3007 is shown in Figure 5.7. The location of the period parallelogram and the nine

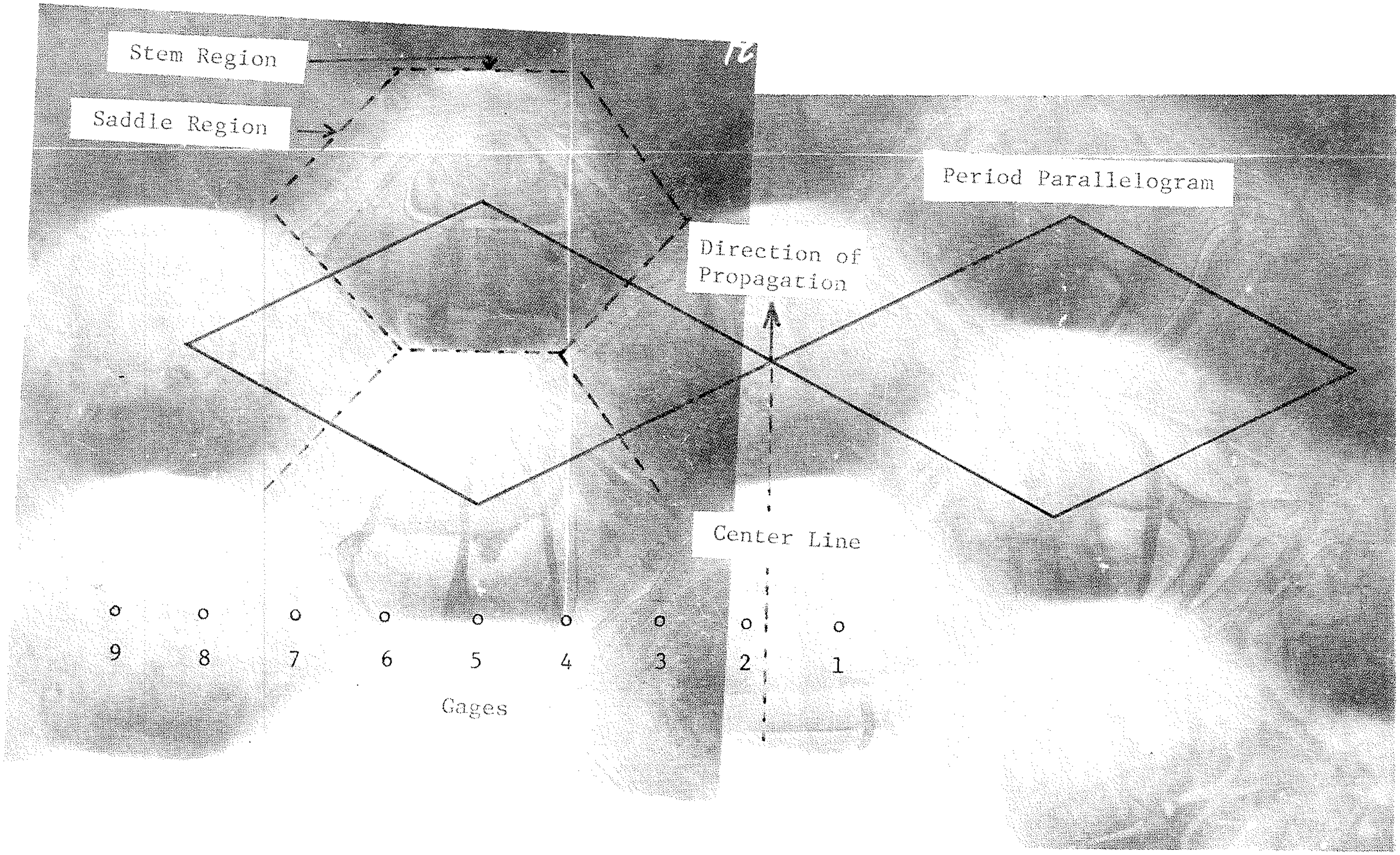

Figure 5.7 Mosaic photograph of the experimental wave field in experiment CN3007

recording wave gages, which were subsequently placed in the basin, are superimposed on the photograph. The dynamic features of the wave field, such as the stem and saddle regions, are clearly visible.

The photographs represent changes in intensity of light originating from the strobes and reflected by the water surface. Since the strobes are located on the wave generator, the approximately straight line segments showing an abrupt change in intensity from light to dark represent wave crests propagating directly away from the generator, in a direction of light to dark. The sharpness of this stem region indicates a near breaking condition for the CN3007 waves. The distinct crest lines representing the stems of interaction are connected by saddles of smaller crest heights. The global wave pattern, composed of a tiling of the basic period parallelograms, is clearly observed in Figure 5.7. The qualitative similarity to the example solutions shown in Chapter 3 can be seen. Certain extraneous features are also included in the photographs. The orthogonal white lines, for example, represent concrete seams on the floor of the wave basin. The ethereal small patterns appearing on the water surface are the result of reflections from the overhead catwalk and the structural members. Both of these features are irrelevant to the collection and analysis of data; however, their existence is acknowledged to explain their appearance. The mosaics for the entire set of experimental waves of Table 4.1 are shown in Figures B.1 of Appendix B.

Measurement of the x- and y-dimensions of the period parallelogram, drawn on each mosaic, results in an initial estimate for μ and ν respectively. An initial value for the parameters $\lambda = \tilde{\lambda}$ can be computed by using the values for the ψ_3 and ψ_4 intercepts of the parallelogram sides corresponding to $\psi_1 = 0,2\pi$ and $\psi_2 = 0,2\pi$. Although the intercepts are difficult to estimate since they depend on the accuracy with which one can draw the parallelogram and the stem and saddle regions, an initial value is obtained which is usually adequate for the first iteration of the optimization algorithm.

In addition to the initial estimates gained from the mosaics, a visual correspondence between the qualitative features of the wave field (stems and saddles for example) and the locations of the nine recording wave gages is determined. This is best illustrated by Figure 5.8, representing the wave traces of the nine gages for the CN3007 test wave. The exact correspondence between each gage and its respective location within the period parallelogram can easily be seen from the photograph. Gages 1, 2, 4, 5, 6, 8, and 9 are clearly located within a stem region where only one wave crest is experienced per passing of the period parallelogram. In contrast, gages 3 and 7 are located in the saddle region where two smaller peaks per period are seen. The visual correspondence between the wave measurements and the photograph proves to be almost indispensable for interpreting the observed three-dimensional waves from the two-dimensional wave traces. The wave traces for all experimental waves are presented in Figures B.2 of Appendix B.

Variations in wave shape and height shown in the initial portion of Figure 5.8 (and in other wave traces) resulted from the sampling of data at the end of the 10 second ramp motion programmed into the wave generator. During this time, the paddle movement is modified by ramping the paddle stroke from zero to its full programmed value in order to provide protection for the wave generator. These regions are usually evidenced by the incomplete evolution of a genus 2 type wave. In addition to

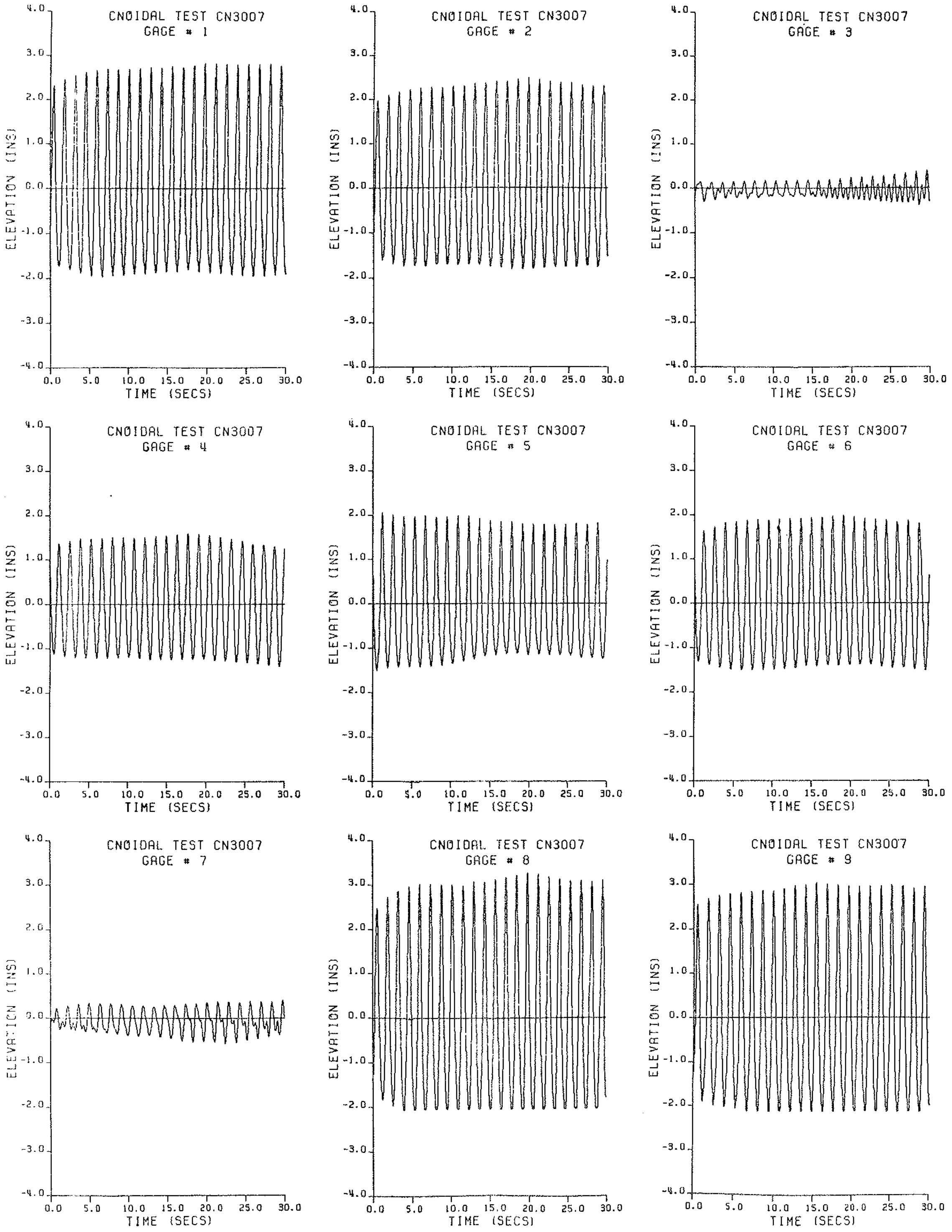

Figure 5.8 Wave profiles for the nine wave gages in experiment CN3007

these effects, reflections from the sidewalls and variations in depth alter the shape of the evolved wave. The error introduced by the depth variations will be addressed in the conclusions of this investigation.

The technique of quantitatively comparing the laboratory data with genus 2 solutions involves the computation of an exact solution corresponding to the location of each of the nine wave gages. From Figure 5.7, the location of each gage with respect to the origin of the coordinate system is estimated. (This origin or zero point correspondence was discussed in Section 4.4.2.) For the example of CN3007, the y-distances were determined to be

Gage # 1:	1.50 ft	Gage # 2:	1.00 ft	Gage # 3:	3.50 ft
Gage # 4:	6.00 ft	Gage # 5:	8.50 ft	Gage # 6:	6.00 ft
Gage # 7:	3.50 ft	Gage # 8:	1.00 ft	Gage # 9:	1.50 ft

The estimate of ν for experiment CN3007 resulted in a y-distance wavelength of 17.0 ft, corresponding to a symmetrical half-length of 8.5 ft. The mirror reflection of distances about 0.0 and 8.5 ft is shown in the above data (i.e. gages 4 and 6 about 8.5 ft and gages 1 and 9 about 0.0 ft). For the case of CN3007, the period parallelogram is 17.0 ft long while the linear gage array is 20.0 ft in length. Several gages can be seen to lie in adjacent parallelograms (gages 1 and 9). Regardless of the size of the parallelogram, each gage can be related to the common point. The determination of the location of this point with respect to the gages is equivalent to selecting an origin of the period parallelogram by means of the nondynamical parameters ψ_{10} and ψ_{20}. The photographs provide this first estimate.

Preliminary estimates of the solution parameters were used to generate exact solutions. For each test case, 31 solution traces, equally spaced along the y-axis of the period parallelogram and parallel to the x-axis, were computed for the three-dimensional wave pattern. These individual traces can be seen in the x-parallel profiles defining the three-dimensional plots. Since the parallelogram is symmetric, a plot of a half-parallelogram is sufficient to define the entire parallelogram, thus quantifying the vertical and horizontal distribution of the entire global wave field. Figure 5.9 presents a detailed plot of this half region by plotting the 16 two-dimensional solution profiles. Note that the crest of the top trace represents the center of the stem region while the middle portion of the bottom trace represents the trough, bounded by a stem crest at either end. The center traces represent the saddle area connecting the stems of adjacent parallelograms. A clearer example of the saddle region is shown in Figure 5.10, where the traces of experiment CN2015 are shown (the photograph corresponding to CN2015 can be seen in Appendix B). The distinct double peaks of the saddle region are easily identified in this figure.

A means of analyzing the complex three-dimensional wave pattern in a way which was both concise and definitive was developed, based on the above two-dimensional slice presentation. Employing this approach, an exact KP solution was evaluated at nine y-locations, corresponding to the locations of each of the nine wave gages within a common half-period parallelogram. This procedure yielded a set of nine two-dimensional slices through the wave pattern which provided a horizontal and vertical definition for the overall wave which could be utilized for further analysis of the data in a quantitative sense. For example, a trace of

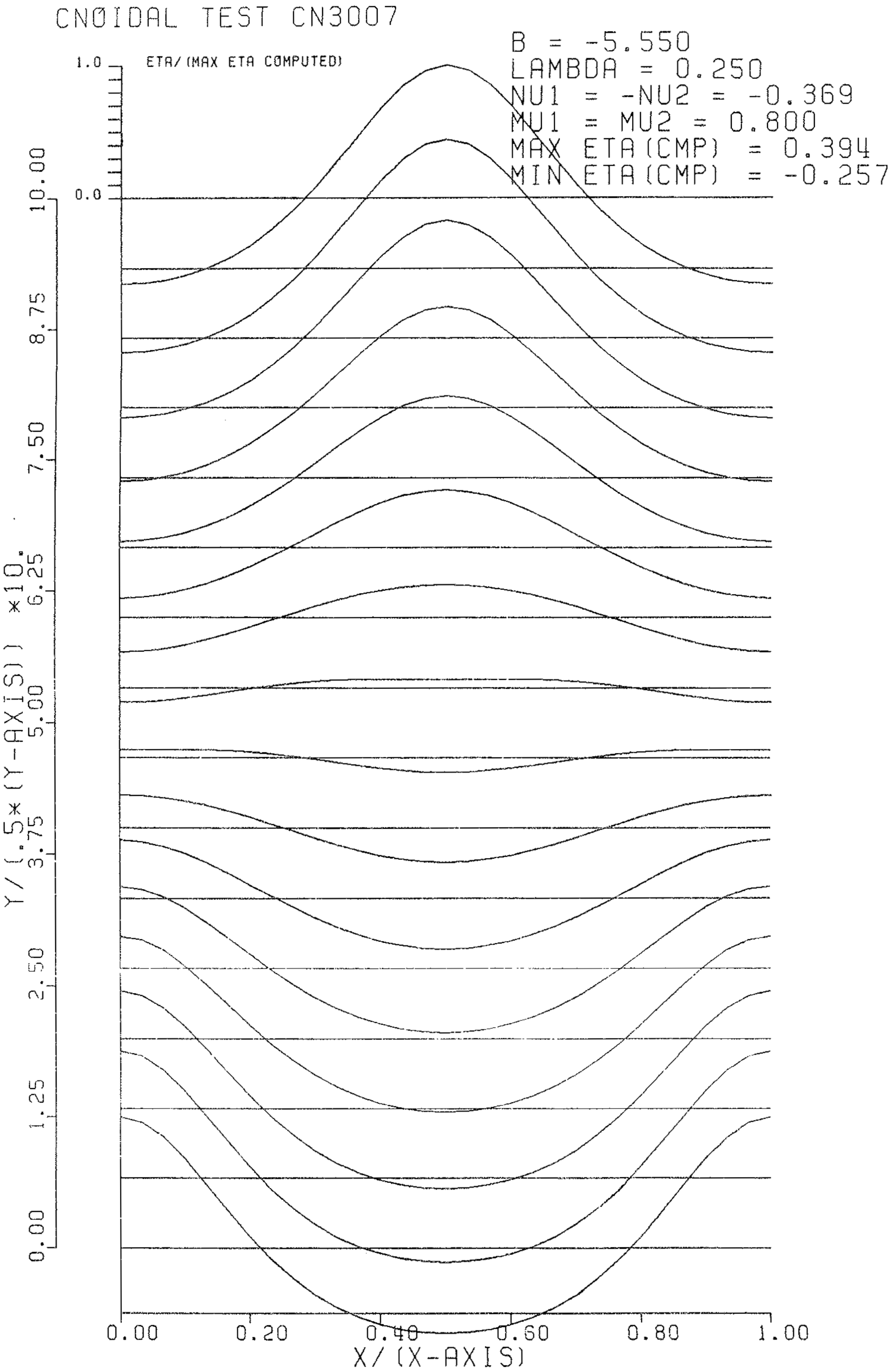

Figure 5.9 Sixteen KP wave profiles for the half-parallelogram solution corresponding to experiment CN3007

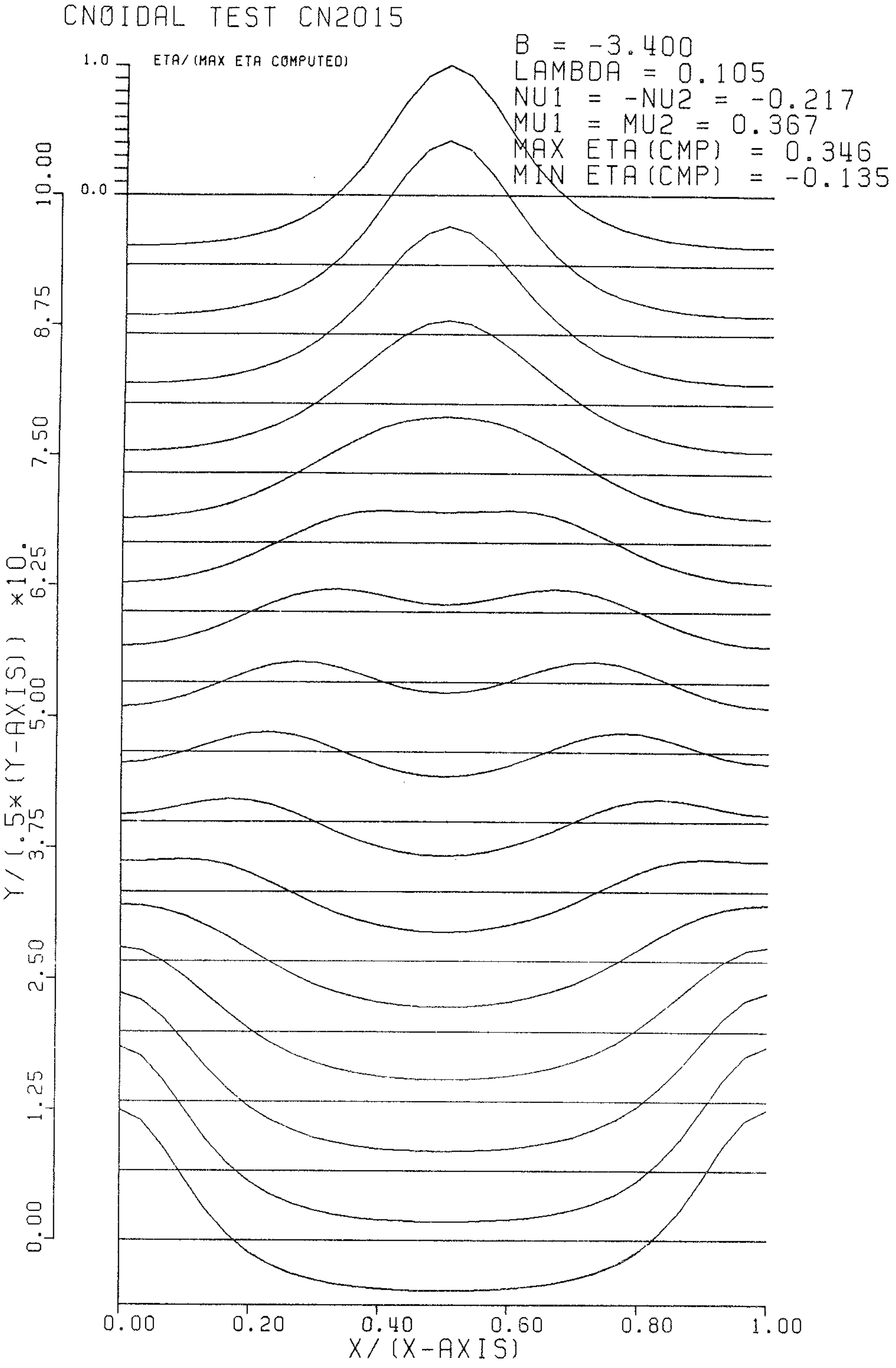

Figure 5.10 Sixteen KP wave profiles for the half-parallelogram solution corresponding to experiment CN2015

solutions was computed such that an exact solution was computed to correspond to the data sampling rate of 50 samples per second for the measured period of each experimental wave. This computation yielded a set of computed wave elevations which were directly comparable in time (point by point) to the collected wave gage data. This permits the use of standard data analysis techniques for comparing the two sets of data. The chosen comparison was a root-mean-square (rms) analysis which defined the rms error between the experimental data and the observed data as

$$\mathrm{rms} = \left\{ \sum_{m=1}^{N} \left(\frac{\zeta_{ob} - \zeta_{comp}}{N} \right)_m^2 \right\}^{1/2} \tag{5.8}$$

where N represents the total number of points in the time series. An average rms error was also computed as the arithmetic mean, or average, of the nine individual rms values so that a comparison of the overall fit for each experimental wave could be made. The rms error approach for comparing two time series of data requires the selection of a single period of data from the 30.0 seconds of data sampled for each experimental wave. The criteria for selecting this "typical" wave will be discussed in the following section. In both examples presented, the free parameters of the solution have been optimized. The following paragraphs demonstrate this optimization process.

The generation of an exact genus 2 solution corresponding to an observed wave field requires the specification of b, μ, and λ describing that wave field. The mosaic photographs are used to estimate

μ, ν, and λ. The maximum observed wave height and the wave period T are determined from the wave gages. The direct use of this data results in an overspecification of the problem. An iteration scheme was therefore developed to converge on a solution which is consistent with all of the data, within the specified limits of accuracy. The following iteration procedure is effectively used to optimize each of the free parameters for each of the twelve experiments.

a. The estimated values for μ, ν, and λ were determined from the photographs. The nondynamical parameters ψ_{10} and ψ_{20} were initialized by requiring the solutions to be computed at specified locations within the period parallelogram corresponding to the location of the wave gages. A single wave period was selected from the wave records. The selection of this single period will be discussed in the following section. A value of b was then selected such that the dimensionalized maximum KP solution (from Equation 5.6) was within 5.0% of the maximum measured elevation at a wave gage whose location is nearest to the center of the stem region where maximum wave elevations occur.

b. The value of $\mu_1 = \mu_2$ was adjusted, if necessary, until the dimensionalized period (from Equation 5.7) was within 3.0% of the measured period corresponding to the wave gage used in Step a. for determining a maximum elevation.

c. The value of λ was adjusted, if necessary, until the dimensionalized value of $\nu_1 = -\nu_2$ yielded a wavelength for the computed period parallelogram which was within 10.0% of the value estimated from the mosaic photographs. A 10-percent criterion was used for this iteration because the length of the parallelogram was difficult to determine accurately from the photographs.

d. Because of the nonlinear coupling of the solution with its parameters, each adjustment affected all parameters to some extent. If corrections were found to be necessary, Steps a. through c. were repeated until all of the computed parameters were within the specified tolerances. An interactive program was written to make the computations and comparisons required for this iteration procedure.

e. A KP solution for each of the wave gages was calculated. A normalized plot comparing theory to measurements at the nine gage locations was made. All comparisons are shown in Figures B.3 of Appendix B. Included in each plot is the rms error for each wave trace. Possible phasing problems regarding the gage locations within the parallelogram were rectified by adjusting the nondynamical phase parameters.

f. A normalized contour map and a three-dimensional view for each wave field was finally prepared as a visual demonstration of the KP solution. Contour plots and three-dimensional view plots for each of the experimental wave are presented in Figures B.4 of Appendix B.

The above procedures were followed for each of the test wave fields of Table 4.1. A minimum tolerance of 5.0% for waveheight, 3.0% for period; and 10.0% for the y-direction wavelength was satisified in all experiments. Section 5.4 presents and discusses these results.

5.4 Presentation and Discussion of Results

The comparisons mentioned in Section 5.3 between the genus 2 solutions and the observed waves for the experiments CN3007 and CN2015 are presented in Figures 5.11 and 5.12. Note that for each gage, the genus 2 solution is shown by a solid line and experimental data are indicated by asterisks. Each gage comparison has a corresponding rms error associated with it to provide a measure of the accuracy of fit. In Figure 5.11, the rms error varies from a value of 0.077 (i.e. which can be interpreted as a 7.7% error) for gage 9 to 0.263 for gage 5. Figure 5.12 shows a range of from 0.038 for gage 4 to 0.203 for gage 2 for expemiment CN2015. Each comparison is based on the deviation between the computed solution and the measured wave profile; hence, agreement requires that both heights and phases match. A difficult area to match is the saddle region in which the wave heights are low and the phasing is complicated since two wave crests are experienced per wave period. For this reason, the rms error in the saddle region is often higher (indicating a poorer fit) than in the stem region. Examples can be seen in the traces of Figures 5.11 and 5.12 as well as for the other experiments shown in Appendix B. The rms values in Figure 5.11 for gages 3 and 7, which are located in the saddle region, are higher than those for gages 8 and 9 located in the stem. Similarily, the large errors for gages 1 and 2 of CN2015 indicate that their location is in the saddle region. When the wave elevations are small, as in gage 3 of Figure 5.11, disagreement is often not as obvious from the rms value as it is in the stem region. In the saddle region, a large deviation from a small number has less impact than a small deviation from a large number in the stem. The effect of small waves on the error estimates

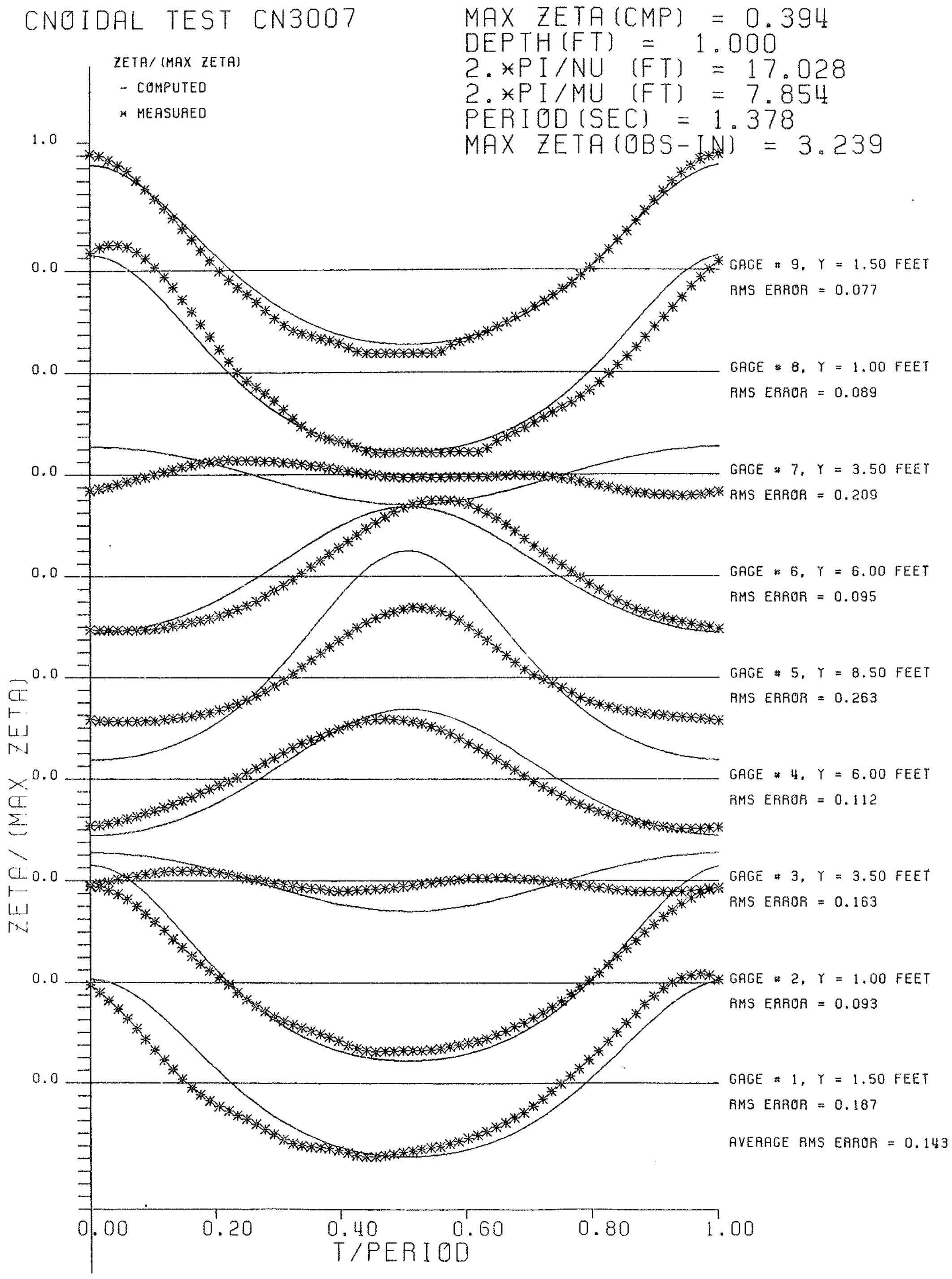

Figure 5.11 Theoretical and experimental wave profiles for experiment CN3007

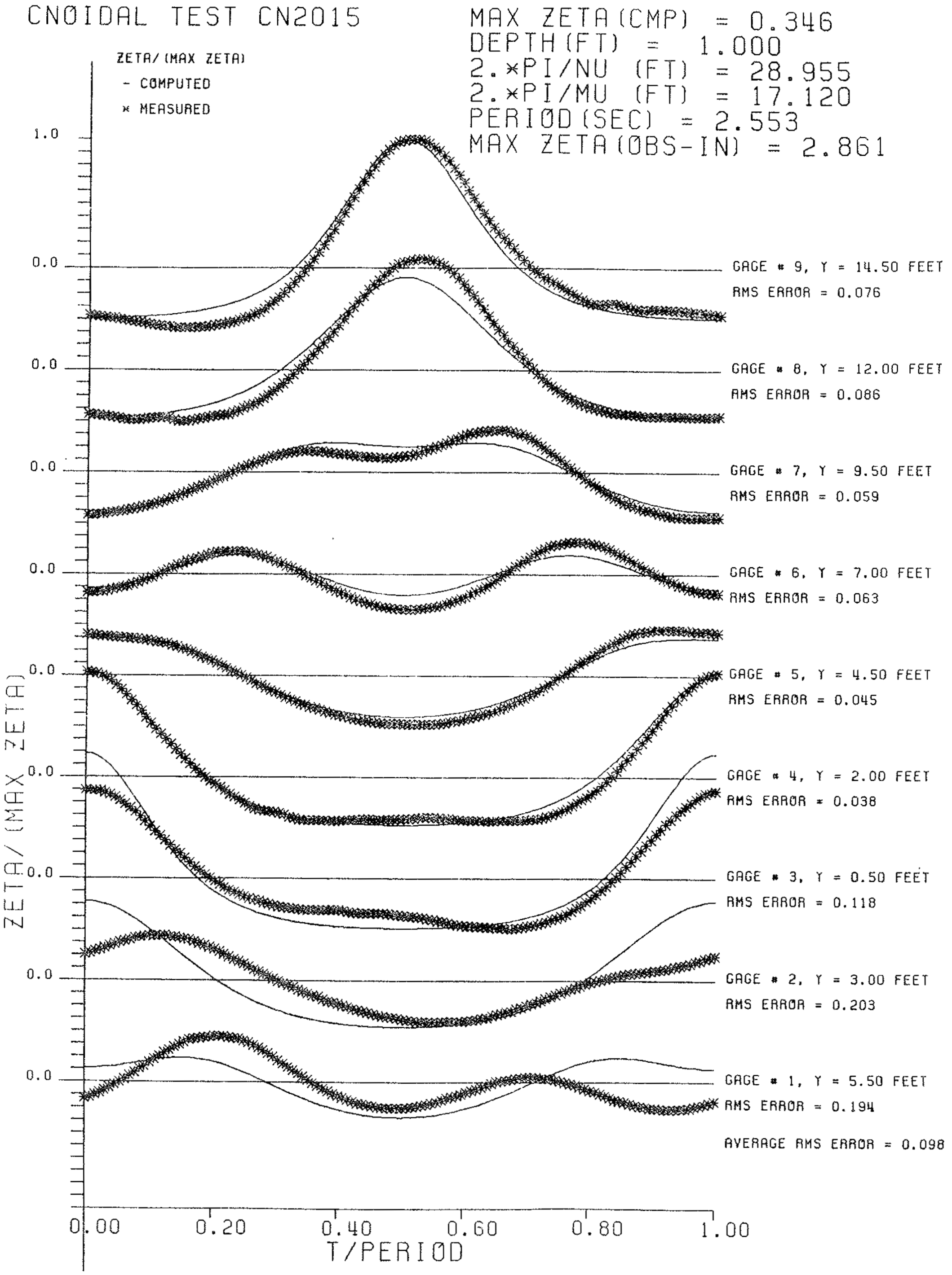

Figure 5.12 Theoretical and experimental wave profiles for experiment CN2015

can be seen in a comparison of gages 1 and 3 of Figure 5.11. Gage 1 shows an error of 0.187 while the visually poorer agreement of gage 3 indicates a better error estimate of 0.163. The rms error values for each gage and for each experiment are presented in Figures B.3 in the Appendix B.

Following optimizing of solution parameters for each experimental wave, a normalized contour map and a three-dimensional perspective view of the computed genus 2 solution was prepared to demonstrate its features. The results for experiments CN3007 and CN2015 are shown in Figures 5.13 through 5.16. In each figure, the saddle and stem regions can be identified and compared to the respective mosaic photograph in Appendix B.

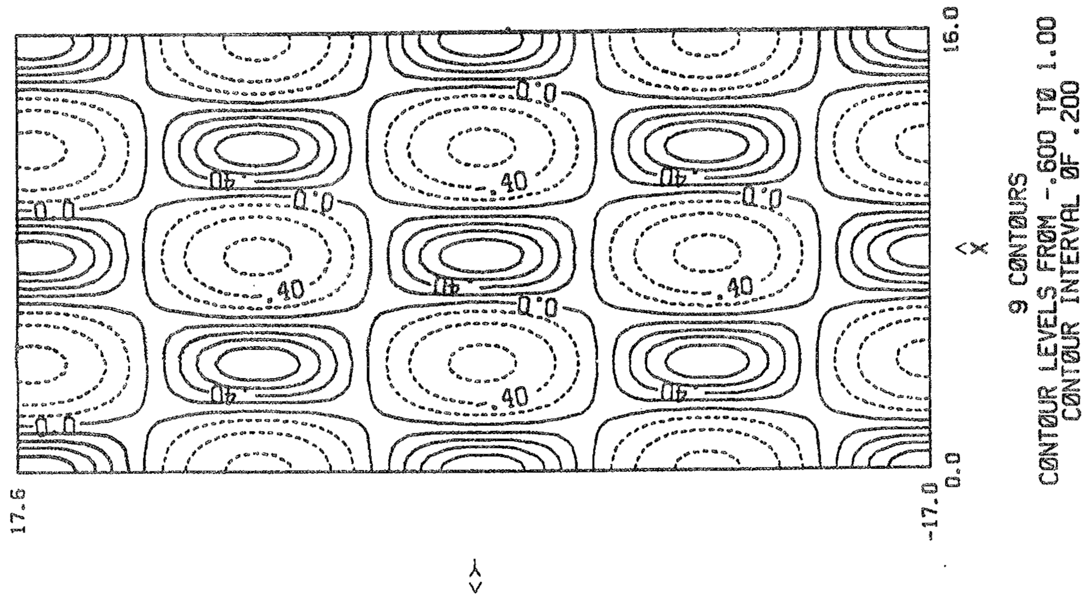

Figure 5.13 Normalized contour map of the theoretical solution for experiment CN3007

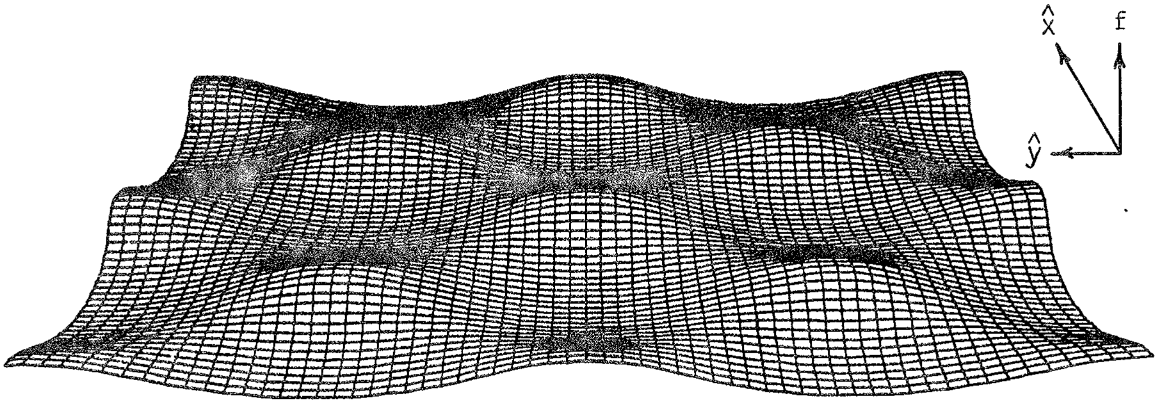

Figure 5.14 Three-dimensional view of the theoretical solution for experiment CN3007

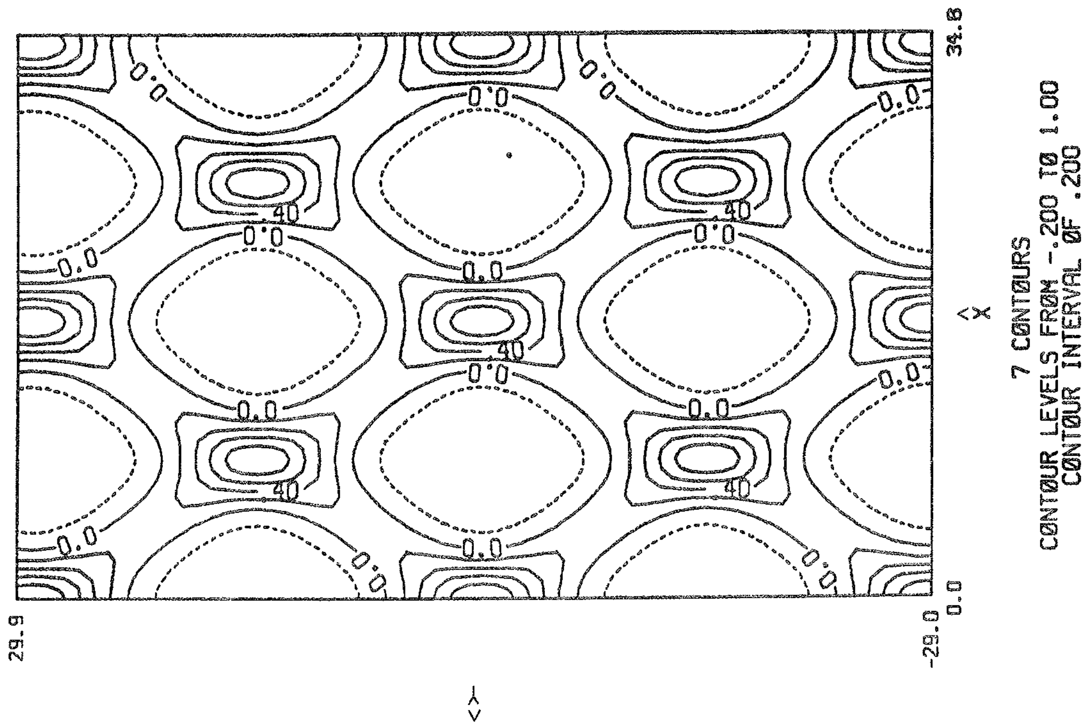

Figure 5.15 Normalized contour map of the theoretical solution for experiment CN2015

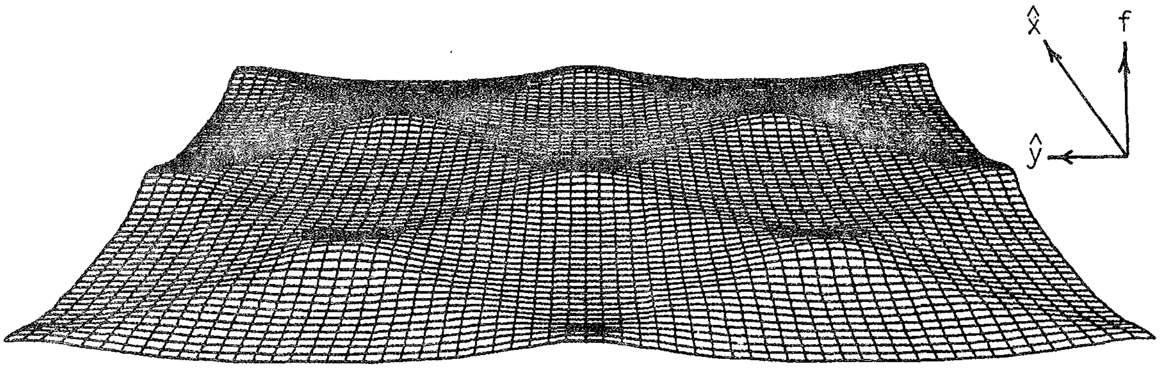

Figure 5.16 Three-dimensional view of the theoretical solution for experiment CN2015

The free parameters and the computed dependent variables of the exact genus 2 KP solution for each of the twelve experiments are presented in Table 5.1. Several observations can be made concerning these parameters. For example, it can be seen that the parameter b increases (becomes less negative) with the angle of intersection and with wavelength. Angle effects can be seen within each grouping of experiments. The nominal 7-foot tests, for example, show a change from -6.200 for CN1007 to -5.150 for CN4007. The effect of the wavelength can be seen in the change from the 7- to the 15-foot tests in which the value changes from approximately -6.0 to -3.5. Results indicate that waves become linear as wavelengths and angles increase. A similar indication of the reduction in wave-wave interactions is shown by the values of λ . Experiment CN1007 indicates a value outside the limits shown by

Table 5.1 Free parameters of the genus 2 KP solution for the experimental program

	Genus 2 Parameters					
Experiment	b	λ	μ	ν	ω	fmax
CN1007	-6.200	0.550	0.900	-0.135	-0.578	0.310
CN1507	-5.500	0.500	0.867	-0.179	-0.379	0.439
CN2007	-5.730	0.400	0.843	-0.230	-0.286	0.383
CN3007	-5.550	0.250	0.800	-0.369	-0.118	0.394
CN4007	-5.150	0.160	0.720	-0.463	-0.632	0.405
CN1011	-4.950	0.400	0.585	-0.131	+0.025	0.293
CN1511	-4.600	0.350	0.565	-0.156	-0.059	0.349
CN2011	-4.400	0.225	0.540	-0.228	-0.240	0.373
CN3011	-4.450	0.120	0.500	-0.304	-0.497	0.302
CN1015	-3.850	0.340	0.420	-0.106	-0.100	0.323
CN1515	-3.600	0.145	0.390	-0.193	-0.307	0.342
CN2015	-3.400	0.105	0.367	-0.217	-0.409	0.346

SF to be required of a basic Riemann matrix. The criterion of SF specifies a limit of +/- 0.5, although the experiments all indicate a positive value indicating a positive phase shift. It appears therefore that the +/- 0.5 criterion can be shifted to a 0.0 to 1.0 limit without loss of generality. The values of μ merely indicate that the x-direction wavelengths are increasing with increasing cnoidal wavelength as would be expected.

The dependent variables (ν, ω, and fmax) reflect the changes in the independent parameters. It can be seen from Table 5.1 that the y-direction wavenumber (ν) decreases as the wave interactions become less. The correlation with the parameter λ can be seen in each set of experiments. An interesting trend in the angular frequency is shown. As the y-direction wavelength increases (as shown by a corresponding decrease in ν), the value of the angular frequency ω necessarily decreases according to Equation 5.7. Otherwise, the measured wave period will not be duplicated by the computed wave. As an example, a positive value of +0.025 for experiment CN1011 is required to balance the effect of the μ value of 0.585 in order to arrive at a computed period equivalent to the measured period of 1.947 seconds. All other values can be seen to be negative and decrease with decreasing μ. As previously stated, maximum wave elevations were maintained relatively constant as shown by the fmax values.

The computed values of ν, ω, and fmax form the basis of the optimization algorithm since it was their values which were used for the comparison with laboratory measured wave characteristics. For example, λ was used to compute a y-dimension wavelength which was required to be accurate to within 10% of the measured value. A 5% criterion was established for the deviation of the maximum wave height computed from fmax and the measured elevation and a 3% error limit was set for differences in the measured period and the period computed from μ. The degree of success achieved with this solution algorithm can be seen in Table 5.2 in which a comparison of these consistency checks is listed.

The specified tolerances were maintained for each experiment as can be computed from the measured/computed comparisons. Included in Table 5.2 is an alternate estimate of overall error, the total rms value, defined as shown below. This formulation was included as an alternate indicator of error to the average rms value shown in Figures B.3.

$$\mathrm{rms}^2_{\mathrm{TOT}} = \frac{1}{9} \sum_{m=1}^{9} \left(\mathrm{rms}^2\right)_m \qquad 5.9$$

Table 5.2 Comparison of measured and computed wave parameters

Experiment	y-wavelength (ft)	measured/computed maximum elevation (ins)	period (sec)	total RMS error
CN1007	46.9/46.5	2.436/2.479	1.38/1.38	0.152
CN1507	34.0/35.1	3.588/3.508	1.38/1.38	0.198
CN2007	27.0/27.3	3.064/3.061	1.38/1.39	0.171
CN3007	17.0/17.0	3.239/3.154	1.38/1.35	0.156
CN4007	12.5/13.6	3.305/3.237	1.38/1.34	0.191
CN1011	48.0/48.0	2.395/2.347	1.95/1.91	0.195
CN1511	38.1/40.3	2.867/2.792	1.94/1.92	0.127
CN2011	26.0/27.6	3.104/2.988	1.94/1.91	0.133
CN3011	20.0/20.7	2.483/2.417	1.95/1.90	0.182
CN1015	56.1/59.3	2.653/2.581	2.55/2.53	0.125
CN1515	32.1/32.6	2.844/2.736	2.54/2.51	0.096
CN2015	27.0/29.0	2.861/2.767	2.55/2.55	0.114

Examination of the results shown in Tables 5.1 and 5.2 show that the computed error between observed waves and genus 2 solutions never exceeds 20%. The nominal 15-foot wavelength experiments (CN1015, CN1515, and CN2015), which were shown to be the most weakly nonlinear according to the values of b, showed errors of only about 10%. Rms errors of this magnitude are acceptable since variations in the elevation of the basin floor are documented to be on the order of 10% of the water depth and some of the waves were observed to be near the point of breaking. Examination of the single cnoidal wave shown in Figure 4.10 shows a 25% variation in the wave envelope. A similar error analysis for the cnoidal wave would show at least the same order of magnitude as seen in the KP waves. In view of the physical size of the facility and the known sources of potential contamination of the wave form, an accuracy of 20% for a three-dimensional wave form is considered very good and is, in fact, better than anticipated.

The method of analysis leading to the results in Tables 5.1 and 5.2 makes use of a single period of measured wave data from a 30.0 second record. In order to show that this analysis technique does provide a definitive comparison, it remains to be demonstrated that this chosen wave is typical of all waves in the record.

A certain amount of variation in the shape of the experimental waves was discussed from the standpoint of the rms error analysis. Some of this variation is due to the startup of the wavemaker which can be seen in the beginning of several of the wave traces shown in Figures B.2. In addition, reflections from the sidewalls and the shoaling effects previously mentioned affect the wave shape. In consideration of all of these factors, the wave period to be analyzed in detail was selected by looking at the wave traces of the nine gages for each experimental wave and choosing a single period which appeared to be fully developed. This region was generally evidenced by the evolution of the two distinct peaks per period in the saddle region. These dual peak regions are clearly visible in the wave traces shown in Figures B.2.

The periods selected for analysis are considered to be typical for the fully developed wave region. In an attempt to quantify this statement, an average rms error was computed for a composite wave calculated by averaging (in time) the selected wave plus 5 adjacent (either preceding or following) wave periods to produce a single composite period of data. This resulted in an analysis of 8.27 seconds of data for the nominal 7.0 ft wavelengths, 11.68 seconds for the 11.0 ft wavelengths, and 15.32 seconds for the 15.0 ft wavelengths. Table 5.3 shows the

Table 5.3 Comparison of the average RMS error for the typical wave and the composite wave

Experiment	typical wave start time (secs)	typical wave average RMS error	composite wave average RMS error
CN1007	23.80	0.141	0.152
CN1507	21.42	0.188	0.186
CN2007	18.46	0.150	0.143
CN3007	21.18	0.143	0.146
CN4007	15.60	0.184	0.178
CN1011	12.28	0.174	0.185
CN1511	15.88	0.122	0.128
CN2011	18.70	0.126	0.133
CN3011	3.18	0.172	0.245
CN1015	4.90	0.120	0.122
CN1515	9.86	0.094	0.095
CN2015	4.54	0.098	0.103

beginning time for each typical wave (see Figures B.2) in each experiment, the average rms error of the typical wave, and the average rms error of the composite wave. Results in Table 5.3 show that the average rms error computed for the composite wave is essentially identical to that computed for the typical wave, with one exception. The typical wave selected for experiment CN3011 appears to have been sampled during the generation ramp, thereby introducing error into the composite wave comparison. The discrepancy can be seen in the average rms error values in which the typical wave shows a value of 0.172 and the composite wave shows 0.245. Inspection of the wave trace for experiment CN3011 shown in Figure B.2i reveals that a starting time of 3.18 seconds was too early in the data series for a typical to composite wave comparison to be meaningful. With this exception, the results show that the typical wave used for the data comparisons is representative of the wave trace. Therefore, the analyses performed and reported are valid.

The results shown in Tables 5.1 and 5.2 quantify the capability of the genus 2 solutions to model the vertical and horizontal distribution of the twelve experimentally generated wave fields. Table 5.3 shows that these comparisons are representative of the entire generated wave. It now remains to be shown that the generated wave fields represent a broad range of conditions and that the comparisons between theory and measurement represent a comprehensive data base for testing the KP equation. If the KP equation proves to be capable of predicting a large variety of waves, its potential applicability for addressing relevant problems may be significant. To accomplish this, each wave field can be categorized as to its degree of nonlinearity, dispersiveness, or three-dimensionality by looking at the numerical values computed for each of the small parameters used in the scaling of the equation shown in Chapter 3. The applicability of the genus 2 solutions to model a variety of waves can then be assessed by considering the error estimates for each of the generated wave fields in view of these computed parameters.

The original derivation of the KP equation was based on the assumed smallness of each of its scaling parameters, i.e. weakly nonlinear, weakly dispersive, and weakly three-dimensional. An equation with the ability to provide an accurate description of the waves when the underlying assumptions of its derivation are met, but still provide an acceptable prediction when the assumptions are moderately violated, can be referred to as robust. Robustness is a highly desirable quality of a wave model since it demonstrates the capacity of the equation to acceptably reproduce a wide class of waves. Table 5.4 presents the

Table 5.4 Small parameters defining nonlinearity, dispersiveness, and three-dimensionality for the experimental program

Experiment	$\alpha = \frac{a}{h}$	$\beta = (kh)^2$	$\epsilon = \left(\frac{m}{l}\right)^2$	α/β	total rms error
CN1007	0.203	0.810	0.022	0.251	0.152
CN1507	0.299	0.752	0.043	0.398	0.198
CN2007	0.255	0.711	0.074	0.359	0.171
CN3007	0.270	0.640	0.213	0.422	0.156
CN4007	0.275	0.518	0.414	0.531	0.191
CN1011	0.200	0.342	0.050	0.585	0.195
CN1511	0.239	0.319	0.076	0.749	0.127
CN2011	0.259	0.292	0.178	0.887	0.133
CN3011	0.207	0.250	0.370	0.828	0.182
CN1015	0.221	0.176	0.064	1.256	0.125
CN1515	0.237	0.152	0.245	1.559	0.096
CN2015	0.238	0.135	0.350	1.763	0.114

small parameters computed for each of the twelve wavefields: α representing nonlinearity, β representing dispersion, ϵ representing three-dimensionality, and the ratio α/β representing the relative effects of nonlinearity and dispersion (comparable to the Ursell number).

Table 5.4 indicates that the nonlinear parameter α, shows the least amount of variation throughout the wave tests. A low value of 0.203 for experiment CN1007 and a maximum value of 0.299 was measured for experiment CN1507. The narrow range of α is not significant in these tests. It is the one parameter which could not be varied beyond a very limited range, due to the method of generation. The experimental waves were evolved by combining cnoidal wave trains with wavelengths varying from 7 to 15 ft and a variety of angles of intersection. Each cnoidal wave was generated with a maximum wave elevation of approximately 1.0 inch. This maximum elevation was used for the generation of all cnoidal wave trains because it was found that larger waves broke for the short wavelength tests (i.e. tests CN3007 through CN3040) while smaller waves were barely visible in the mosaic photographs of the 15 foot wavelength tests (CN1507 through CN1520). For this reason, the range of maximum elevation is necessarily limited. It can be seen, however, that the parameter α is not particularly applicable to these three-dimensional waves since a strong degree of nonlinearity can be seen in the mosaics of the 7-foot waves in which almost all waves can be seen to be on the verge of breaking in the stem region.

The second parameter, β, provides a measure of wave dispersion and is used to categorize a flow as deep or shallow. Results shown in Table 5.4 indicate almost an order-of-magnitude range for this parameter. For example, experiment CN1007 was measured at 0.810 and experiment CN2015 showed a value of 0.135. Since all values are in the shallow-water regime, it can be concluded that the experimental program covers a broad range of shallow-water conditions.

The third parameter represents the most important aspect of the present study since it provides a quantitative description of the three-dimensional structure of the waves. This parameter provides the means of actually quantifying the capability of the KP equation to model a genuinely three-dimensional flow. Results reported in Table 5.4 show that the generated wave fields exhibited a strong three-dimensional structure whose descriptive parameters spread over an order of magnitude. Experiment CN1007 showed the least amount of three-dimensionality as indicated by the value of 0.022. A maximum value of 0.414 was measured for experiment CN4007. The assumption of weakly three-dimensional is clearly violated by this latter figure since it indicates the wave to be almost equally structured in both principal directions. The computed error for this test is, however, only 19.1%. Experiments CN3011 and CN2015 also show a high degree of three-dimensional structure which surpasses the weak assumption. The error for these experiments is computed to be just 18.2% and 11.4% respectively. The fact that the genus 2 solutions are capable of modeling these waves to the reported accuracy certainly shows the KP equation to be robust in its ability to accurately model a three-dimensional wave field.

A final calculation is shown in order to demonstrate that the observed permanent form waves have an Ursell parameter of order unity. The ratio of α/β represents the ratio of nonlinearity to dispersiveness reported by Ursell. Ursell showed that this ratio is of order unity for a permanent form wave. Table 4.5 shows this value to be in the range of 0.251 (CN1007) to 1.763 (CN2015).

In addition to an evaluation of the scaling parameters, several observations can be made regarding the experimental wave fields which demonstrate the robustness of the laboratory waves. For example, it was stated that during the wave generation phase, the maximum specified wave elevations for the component waves had to be reduced because the evolved waves were breaking. Even when they did break, the wave crests reformed and the horizontal integrity of the hexagonal pattern was retained. Not only did the generated waves prove to be stable to a variety of geometrical configurations, they were also observed to be stable to several sources of external perturbation. For example, variations in the depth of flow shown in Figure 4.1 were shown to produce wave height variations of 25%. Also; reflections from sidewalls, the fact that the correct wave was not generated but evolved, the 10 second generation ramp, etc., all contributed to a small spatial variability in the experimental waves. Although these extraneous sources of error are known to exist (but could not be corrected), the waves always retain their basic qualitative features with the observed perturbations maintained about these fixed wave features.

The results of the laboratory phase of the investigation show that stable three-dimensional nonlinear wave forms were successfully produced in the wave basin which are qualitatively similar to the genus 2 solutions of the KP equation. These wave forms were evolved by simultaneously generating two cnoidal wave trains of variable wavelength at symmetrical angles of intersection to the wave generator. The wavelengths and angles of intersection used to produce these wavefields are presented in Table 4.1. The wave forms were observed to evolve into genus 2-like hexagonal surface patterns almost immediately after leaving the wave generator paddles. All wave forms were shown to be extremely stable with respect to both variations in the basic wave components and to perturbations to the evolved wave. Examples of this stability are evident in the photographs shown in Figures B.1 and in the wave gage traces shown in Figures B.2. A correspondence between the three free parameters of the genus 2 solution was developed and described. The resulting exact solutions were compared with their respective laboratory waves. Quantitative comparisons between the computed solutions and the observed waves were provided by means of an rms error analysis. Results of that analysis show the KP equation to be capable of accurately modeling genuinely three-dimensional, nonlinear, waves in shallow water.

CHAPTER 6

CONCLUSIONS

A new class of genuinely three-dimensional, nonlinear, shallow water waves is reported herein. These new waves are produced in the laboratory by the simultaneous generation of obliquely intersecting cnoidal wave trains. The generation procedure requires the use of a large-scale directional spectral wave generation facility. The resulting wave pattern resembles a tiling of uniformly sized, permanent form, hexagonal surface wave patterns. Wave crests defining the hexagonal pattern consists of stems of interaction, resulting from the nonlinear interaction of the two component cnoidal waves, and saddle regions connecting forward and rearward adjacent stems. Wave heights along these crests vary from a maximum in the stem region to a minimum in the saddle area. These waves are stable and possess the qualitative features given by exact solutions to the Kadomtsev-Petviashvili (KP) equation. The KP equation has been shown to admit an infinitely dimensional family of exact solutions in terms of Riemann theta functions of genus N. The solutions of interest are the genus 2 solutions. These exact solutions are biperiodic in the sense that they have two independent periods in both space and time.

A comprehensive laboratory investigation is described which demonstrates that the genus 2 solutions of the KP equation quantitatively describe the features of these new waves. Experiments are reported in which twelve wave fields are evolved through the discrete generation of cnoidal wave trains of various wavelengths and at various angles of intersection. The horizontal and vertical structure of each experimental wave is quantified by overhead mosaic photography and by a linear array of nine resistance-type recording wave gages. A wide range of variability in size and shape of the repetitive wave pattern is achieved in order to fully test the limits of applicability of KP theory.

General genus 2 solutions of the KP equation require the specification of eight free parameters, two of which are nondynamical in nature. A subset of this general solution is tested by the generation of equal and symmetric (with respect to the axis of the wave generator) component waves. Symmetry introduces three constraints which reduce the required number of free parameters to five, three dynamical and two nondynamical. Verification of the KP equation using twelve wave fields therefore requires the development of a unique correspondence between the three free solution parameters and the physical characteristics of the laboratory generated waves. The experimental procedure reported here utilizes the maximum measured wave elevation in the stem, the measured wave period, and the measured y-direction wavelength of the repetitive surface pattern to compute and optimize the 3 free parameters.

Results of this investigation show that a reasonable agreement was achieved between all experimental waves and their respective optimized exact solutions. Accuracy of the theoretical solution fit was quantified by rms error computations between experimental data at each wave gage and exact solutions corresponding to the location of each gage. Total error estimates for each experiment, computed from the individual gage rms values, varied from 9.6% to 19.8% over the entire range of data. The following sources of contamination are known to have contributed to these discrepancies. Variations in the nominally 1 ft water depth were measured to be 10%. Wave reflections from the sidewalls were observed to occur following wave generation, and wave fields were generated which clearly violated the basic assumptions of weak nonlinearity, weak dispersiveness, and weak three-dimensionality used in the derivation of the KP equation (several of the wave fields were on the verge of breaking while others evolved from waves intersecting at nearly 40 degrees). In view of these sources of error, the measured agreement is considered excellent.

APPENDIX A

ELLIPTIC FUNCTION SOLUTIONS TO THE KdV EQUATION

The generation of the nonlinear surface wave patterns for this project required the computation of the "cn" Jacobian elliptic function, the complete elliptic integrals of the first and second kinds, and the incomplete elliptic integral of the second type. Due to the importance of these functions in the generation of waves, the solution techniques used for their calculation are described below.

The cn Jacobian elliptic function calculation was based on the reference parameters shown on Figure A.1.

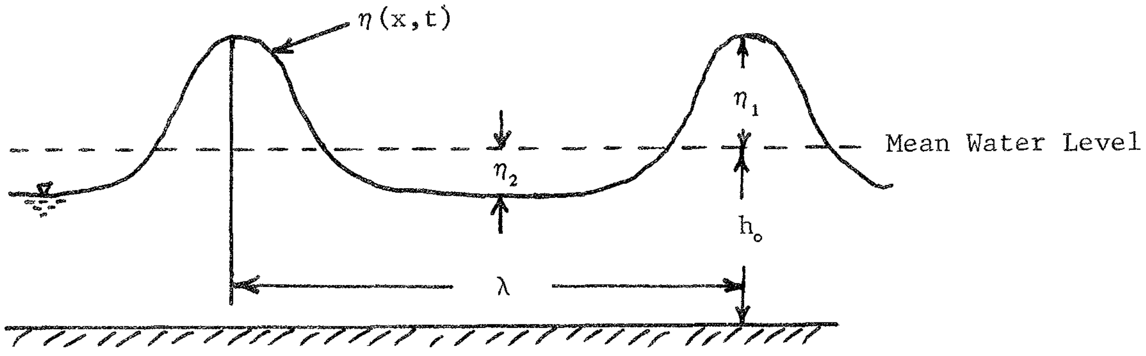

Figure A.1 Schematic diagram of the fluid boundary

The following relationships, presented by Hammack (1985), were used to define the cn function:

$$\eta = -\eta_2 + (\eta_1 + \eta_2)\mathrm{cn}^2\left\{\left[\frac{3(\eta_1 + \eta_3)}{4\ h_o}\right]^{1/2} \left(\frac{x-Vt}{h_o}\right)\middle|\, m\right\} \qquad \text{A.1}$$

$$m = \frac{\eta_1 + \eta_2}{\eta_1 + \eta_3} \qquad \text{A.2}$$

$$\lambda = h_o\left[\frac{16h_o}{3(\eta_1 + \eta_3)}\right]^{1/2} K(m) \qquad \text{A.3}$$

$$\eta_3 = \eta_1\left[\frac{E(m)}{K(m) - E(m)}\right] \qquad \text{A.4}$$

$$V = (gh_o)^{1/2}\left[1 + \frac{1}{2}\left(\frac{\eta_1}{h_o} - \frac{\eta_2}{h_o} \ \frac{\eta_3}{h_o}\right)\right] \qquad \text{A.5}$$

where E(m) and K(m) represent the complete elliptic integrals of the first and second type. The known wave characteristics are the wavelength λ and the peak wave height above mean water η_1. Computationally, an initial value for the elliptic parameter m is selected as 0.5. The complete integrals of the first and second type are then computed, corresponding to this m, from the following representation presented by Abramowitz and Stegun (1970):

$$\begin{aligned} K(m) = {} & (1.38629 + 0.1119723\ m_1 + 0.0725296\ m_1^2) \\ & + (0.50 + 0.1213478\ m_1 + 0.0288729\ m_1^2)\ \ln(1./m_1) \end{aligned} \qquad \text{A.6}$$

$$\begin{aligned} E(m) = {} & (1.00 + 0.4630151\ m_1 + 0.1077812\ m_1^2) \\ & + (0.2452727\ m_1 + 0.0412496\ m_1^2)\ \ln(1./m_1) \end{aligned} \qquad \text{A.7}$$

where the complementary elliptic parameter m_1 is defined as

$$m_1 = 1. - m . \qquad \text{A.8}$$

A value for η_3 can now be computed from equation A.4 for the trial value of m. A wave length λ can then be computed and compared to the known wavelength value. An iterative solution is now used to determine an m value which will produce a wavelength that matches the input value to some desired degree of accuracy. When this criteria has been satisified, all of the arguments of equation A.1 are determined. Consolidation of equations A.1 through A.5 results in the following compact definition:

$$\eta = -\eta_2 + (\eta_1 + \eta_2)\ \mathrm{cn}^2(u|m)$$

where the elliptic argument is defined as

$$u = 2K(m)\left(\frac{x}{\lambda} - \frac{t}{T}\right) . \qquad \text{A.9}$$

The procedure for computing the cn function, once the arguments have been determined, was based on the procedure given by Milne-Thompson (1950). The algorithm used makes use of a known nonlinear wave property that the elliptic parameter m approaches unity as the wave becomes more nonlinear (in contrast, m=0 is a property of a linear sinusoidal wave shape). Since only nonlinear wave shapes with a high m value were of interest, the following approximations were used to compute the sn, cn, and dn functions:

$$\mathrm{sn}(u|m) = \tan u + \frac{1}{4} m_1 \mathrm{sech}^2 u\,(\sinh u \cosh u - u) \qquad \text{A.10}$$

$$\mathrm{cn}(u|m) = \mathrm{sech}\, u - \frac{1}{4} m_1 \tanh u\, \mathrm{sech}\, u\,(\sinh u \cosh u - u) \qquad \text{A.11}$$

$$\mathrm{dn}(u|m) = \mathrm{sech}\, u + \frac{1}{4} m_1 \tanh u\, \mathrm{sech}\, u(\sinh u \cosh u + u)\ . \qquad \text{A.12}$$

The above approximations are only exact when the parameter m is unity. The accuracy of this represention for waves with a parameter value less than unity can be substantially improved by increasing the parameter value by using an ascending Landen transformation. These relationships are as shown below.

$$\mu_1 = \left(\frac{1 - m^{1/2}}{1 + m^{1/2}}\right)^2 \qquad \text{A.13}$$

$$\mu = \frac{4m^{1/2}}{(1 + m^{1/2})^2} \qquad \text{A.14}$$

$$v = \frac{u}{1 + \mu_1{}^{1/2}} \qquad \text{A.15}$$

$$\mathrm{sn}(u|m) = \frac{(1 + \mu_1^{1/2})\mathrm{sn}(v|\mu)\mathrm{cn}(v|\mu)}{\mathrm{dn}(v|\mu)} \qquad \text{A.16}$$

$$\mathrm{cn}(u|m) = \frac{1 - (1 + \mu_1^{1/2})\mathrm{sn}^2(v|\mu)}{\mathrm{dn}(v|\mu)} \qquad \text{A.17}$$

$$dn(u|m) = \frac{1 - (1 - \mu_1^{1/2})sn^2(v|\mu)}{dn(v|\mu)} \qquad A.18$$

where the right hand terms are computed with Equations A.10, A.11, and A.12. The use of the approximations in conjunction with the ascending Landen transformation will result in the computation of the Jacobian elliptic functions to any desired degree of accuracy. For example, a single application will effectively increase an m value of 0.640 to a value of 0.988. A single transformation was used for all wave conditions.

Computation of the incomplete integral of the second kind, $E(u|m)$, was based on the procedure extracted from Abramowitz and Stegun (1965) and presented by Goring (1978). This computational procedure begins with the defining of an Arithemetic-Geometric Mean (AGM) scale as follows:

$$\begin{array}{lll}
a_o = 1 & b_o = \sqrt{m_1} & c_o = \sqrt{1 - m_1} \\
 & & \\
a_1 = \frac{1}{2}(a_o + b_o) & b_1 = \sqrt{a_o b_o} & c_1 = \frac{1}{2}(a_o - b_o) \\
\bullet & \bullet & \bullet \\
\bullet & \bullet & \bullet \\
\bullet & \bullet & \bullet \\
a_n = \frac{1}{2}(a_{n-1} + b_{n-1}) & b_n = \sqrt{a_{n-1}\, b_{n-1}} & c_n = \frac{1}{2}(a_{n-1} - b_{n-1})
\end{array} \qquad A.19$$

Computations stop at the nth step when $a_n = b_n$ (i.e. when $c_n = 0.$) or to the degree of accuracy desired. The incomplete integral can be computed in the following three steps:

1. Define the argument

$$\phi_n = 2^n a_n u$$

where u is the elliptic argument defined by equation A.9 and N represents the Nth step of the AGM matrix.

2. Compute the additional arguments

$$\phi_{n-1}, \phi_{n-2}, \ldots, \phi_0$$

from the relationship

$$\phi_{n-1} = \sin^{-1}(c_n \sin \phi_n / a_n) + \phi_n /2.$$

3. Compute the incomplete elliptic integral of the second type

$$E(u|m) = \frac{E(m)u}{K(m)} + c_1 \sin \phi_1 + c_2 \sin \phi_2 + \ldots + c_n \sin \phi_n$$

All of the above numerical representations were used in the generation of the two-dimensional surface wave patterns with the directional spectral wave generator.

APPENDIX B

EXPERIMENTAL DATA AND EXACT GENUS 2 KP SOLUTIONS

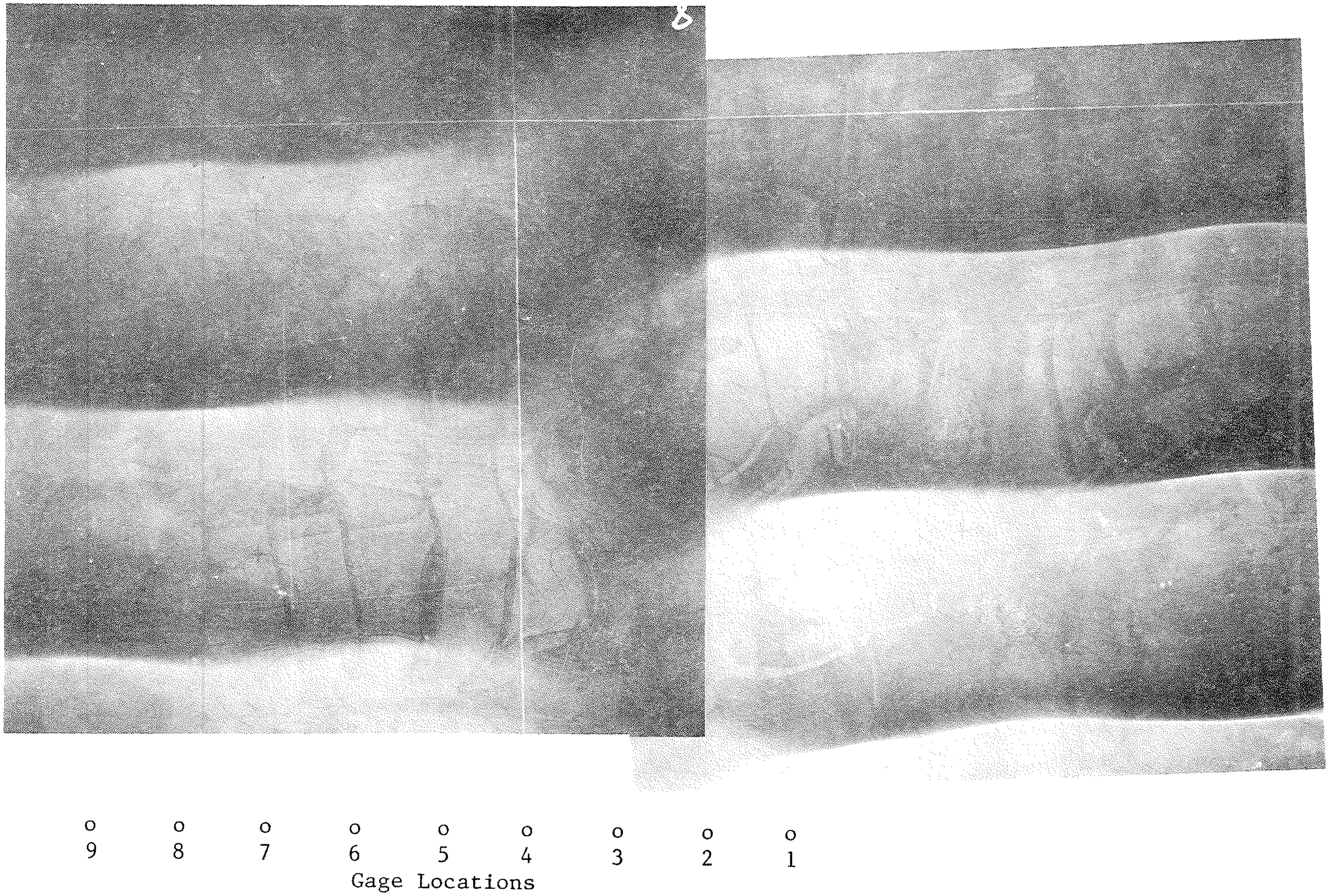

Figure B.1 Mosaic photographs of the experimental waves.

a) Experiment CN1007

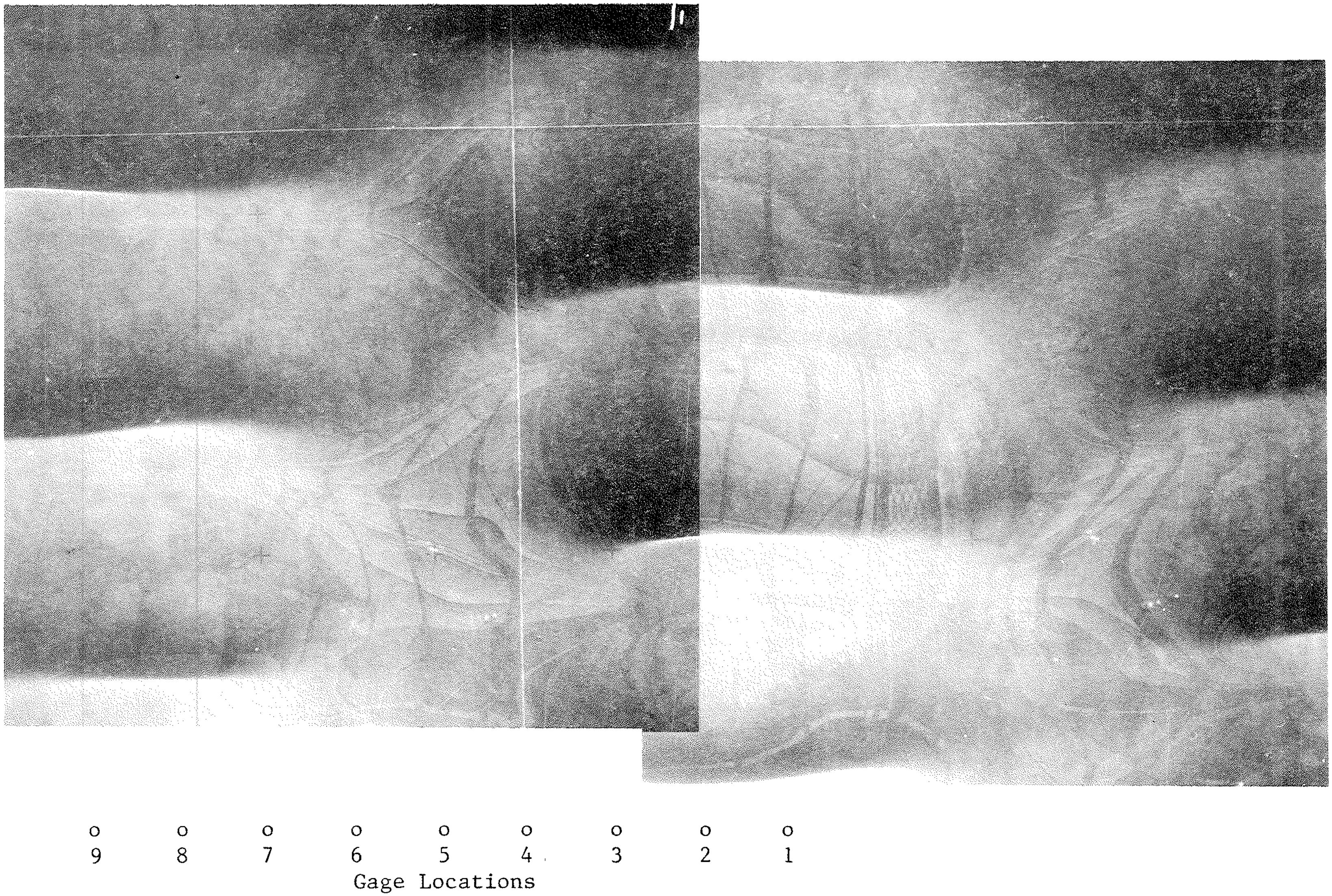

Figure B.1b Experiment CN1507

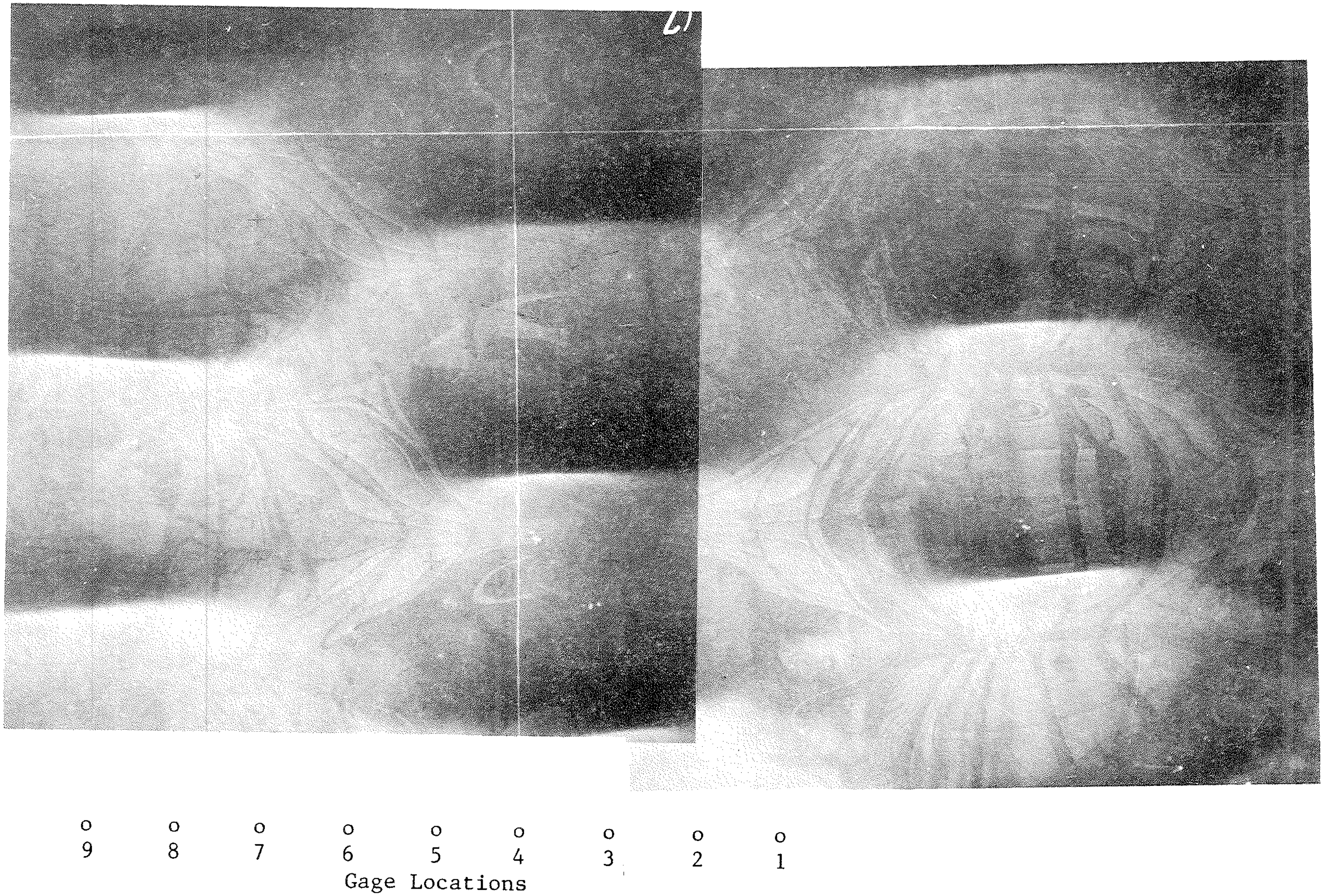

Figure B1c Experiment CN2007

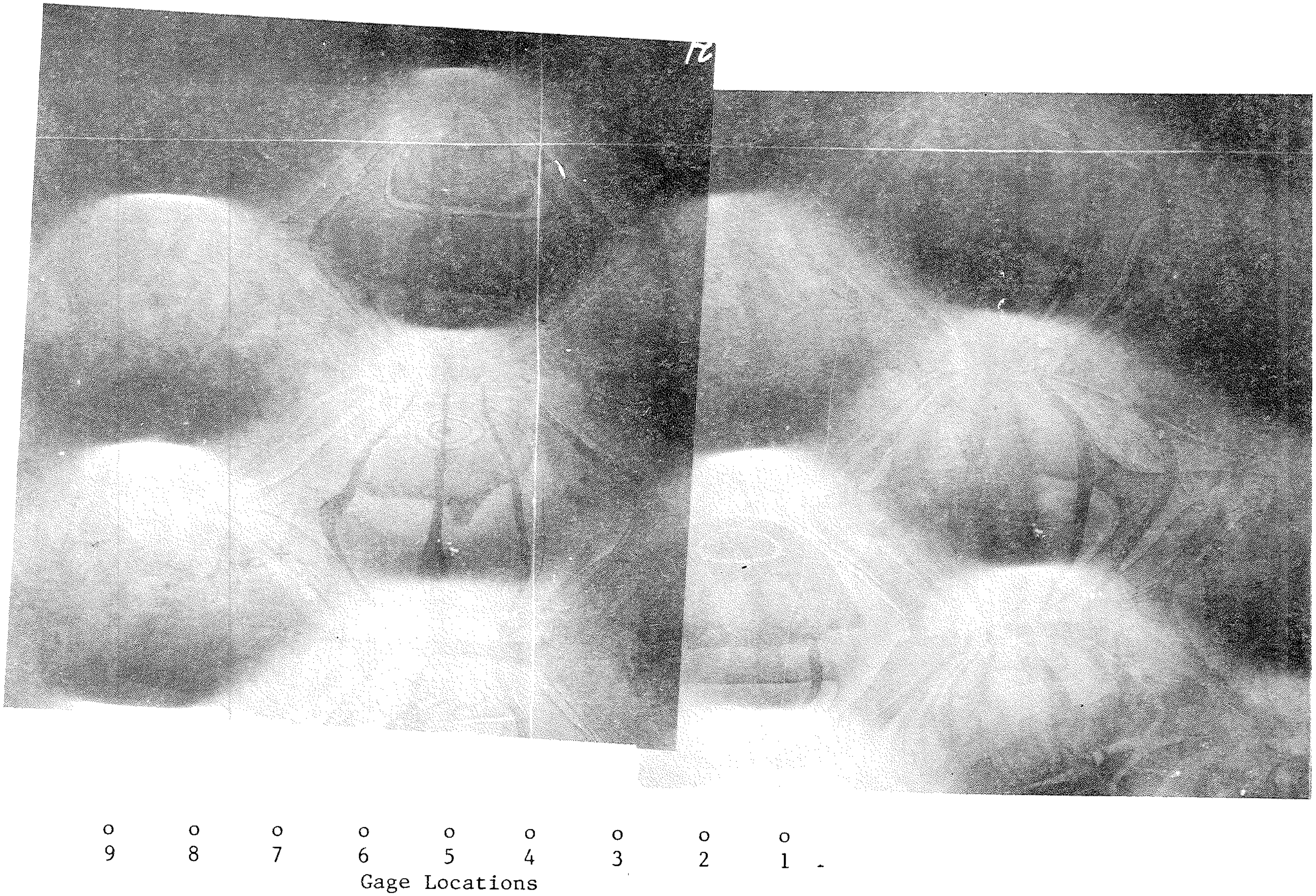

Figure B.1d Experiment CN3007

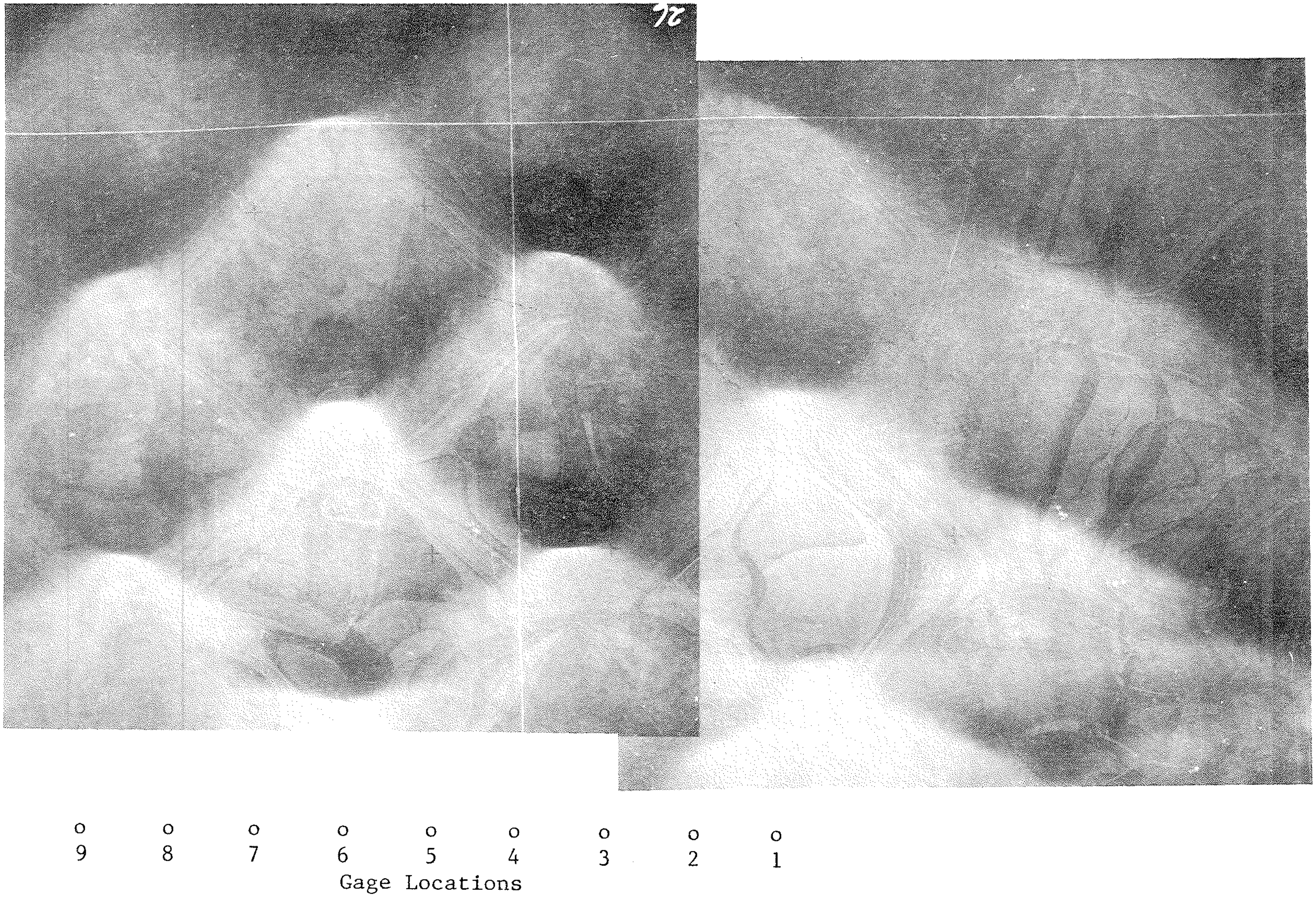

Figure B.1e Experiment CN4007

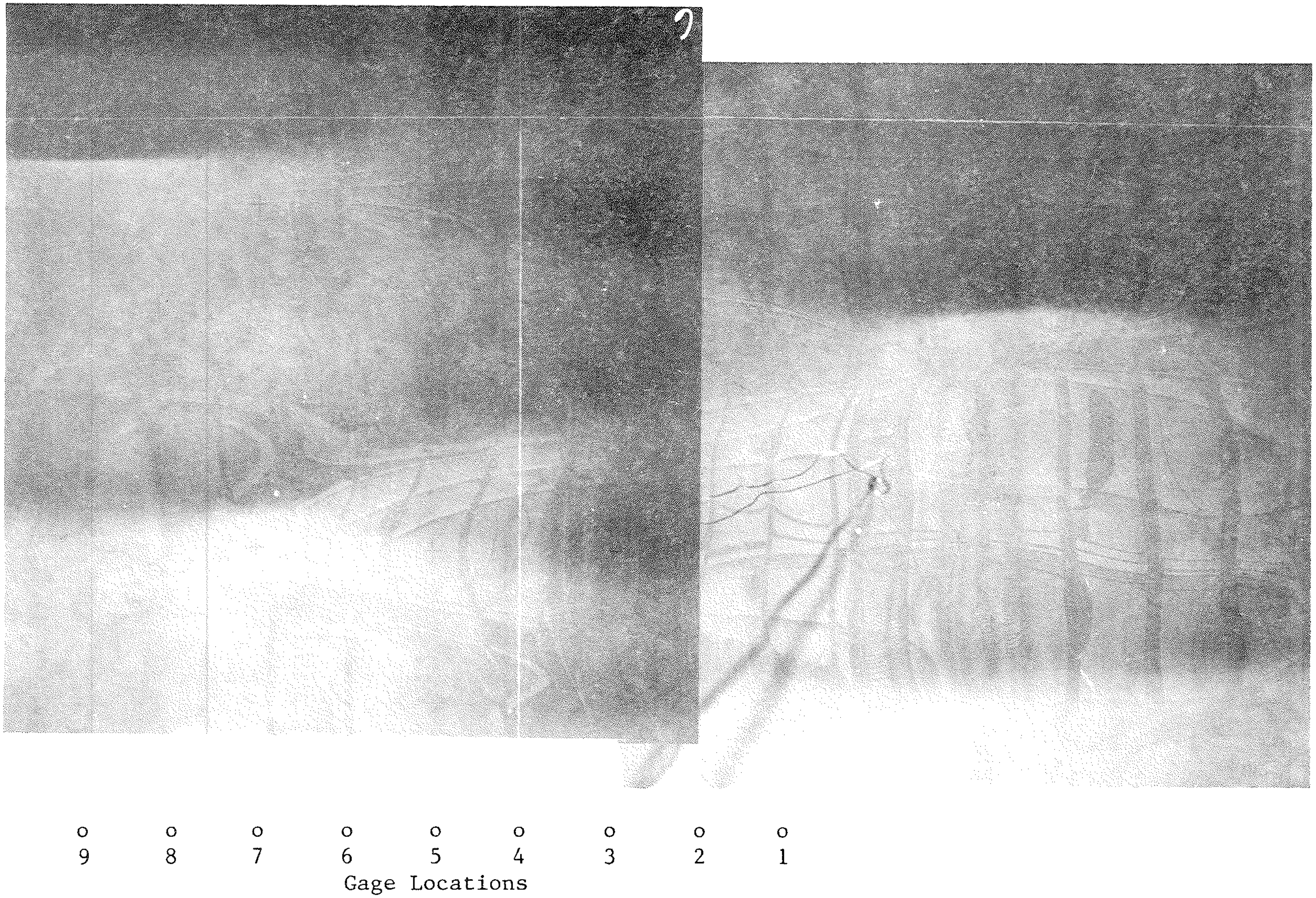

Figure B.1f Experiment CN1011

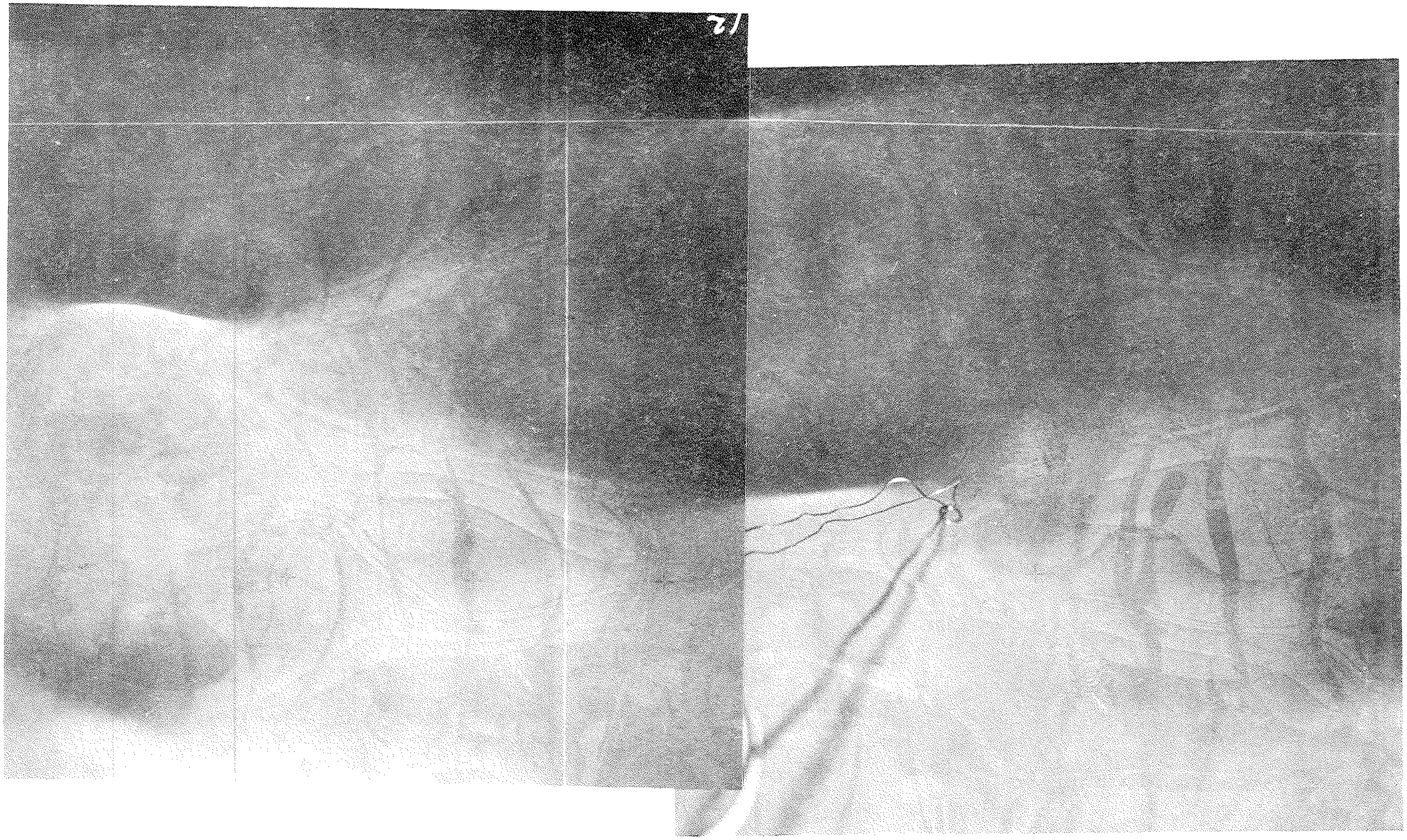

Figure B.1g Experiment CN1511

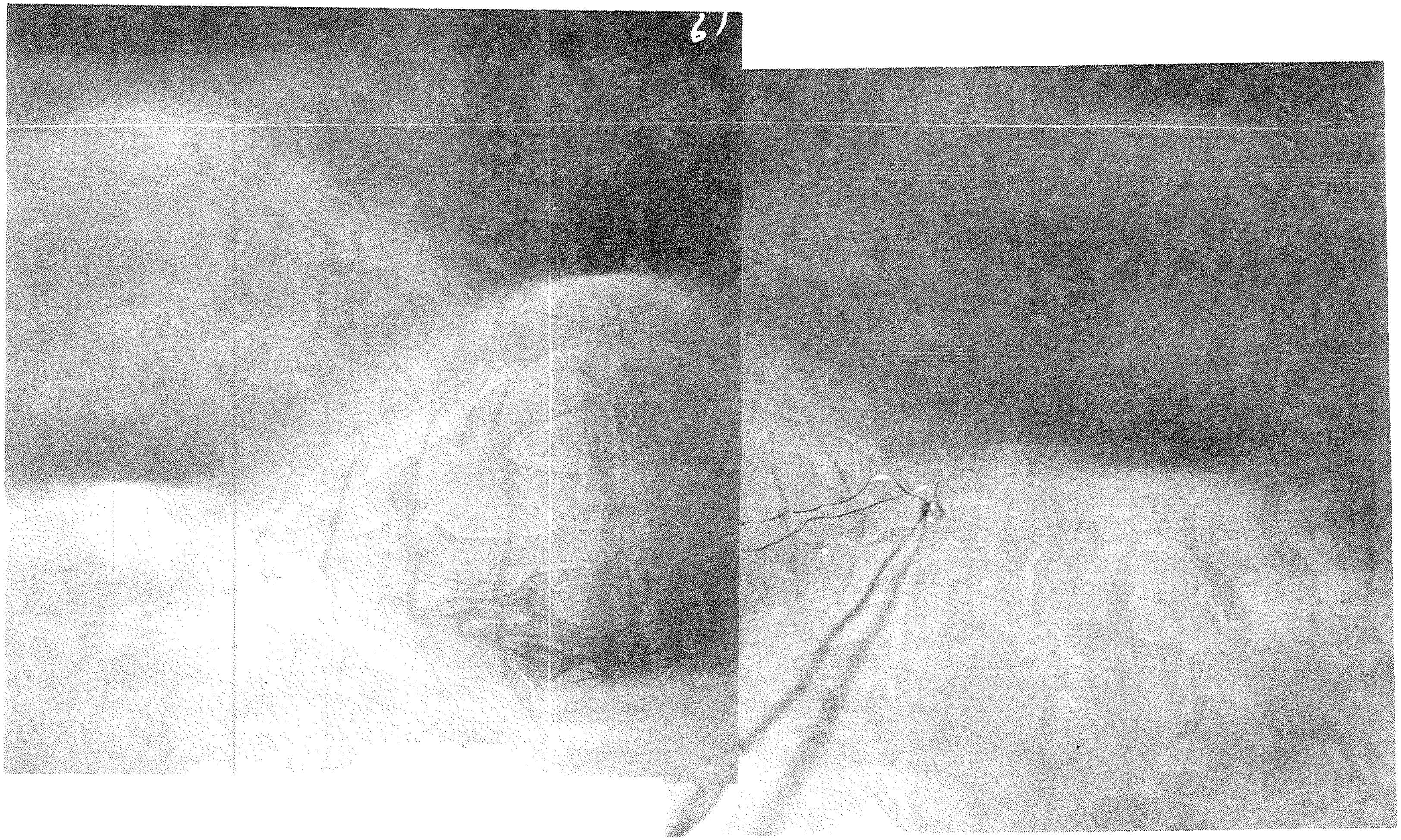

o o o o o o o o o
9 8 7 6 5 4 3 2 1
Gage Locations

Figure B.1h Experiment CN2011

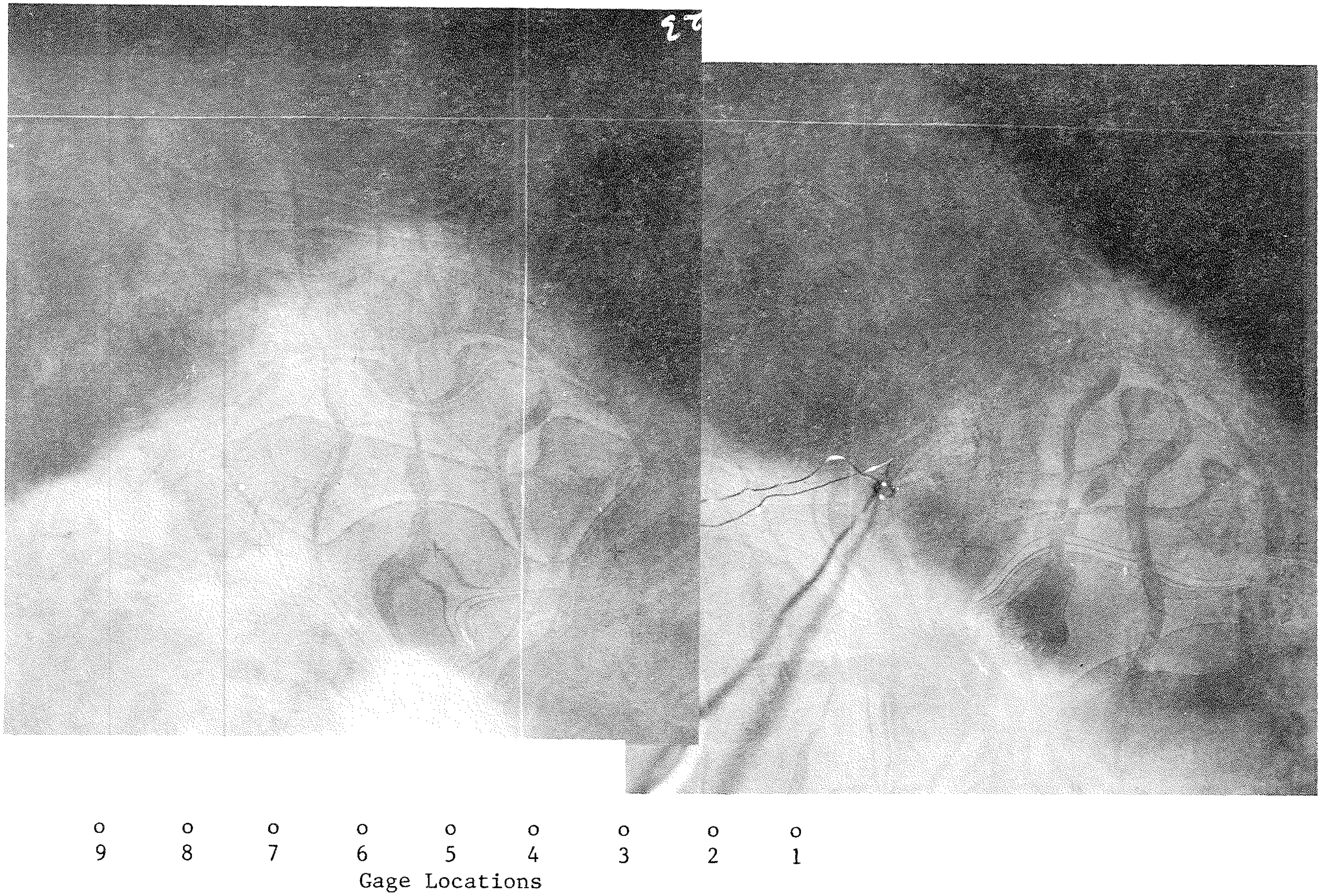

Figure B.1i Experiment CN3011

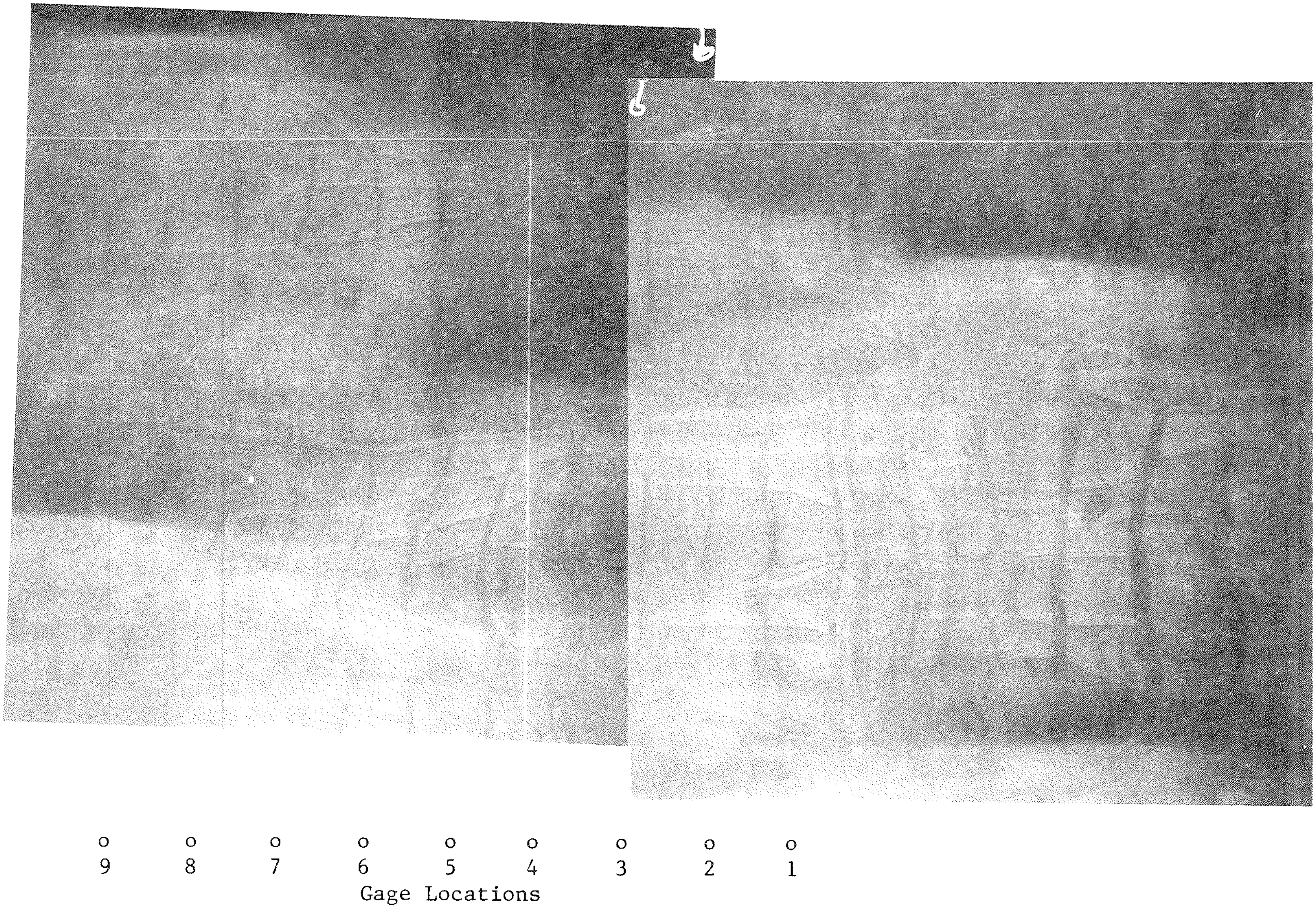

Figure B.1j Experiment CN1015

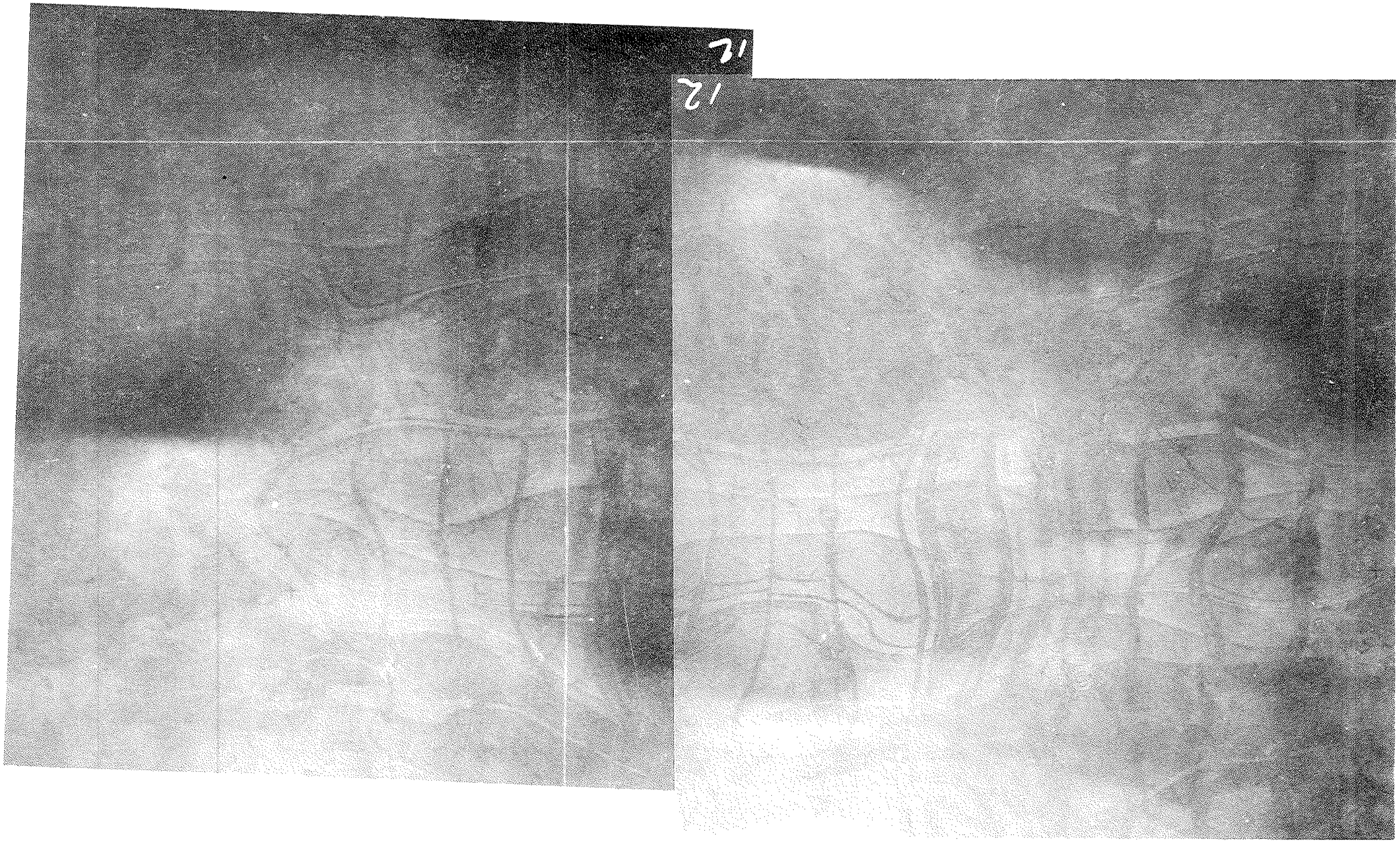

o o o o o o o o o
9 8 7 6 5 4 3 2 1
Gage Locations

Figure B.1k Experiment CN1515

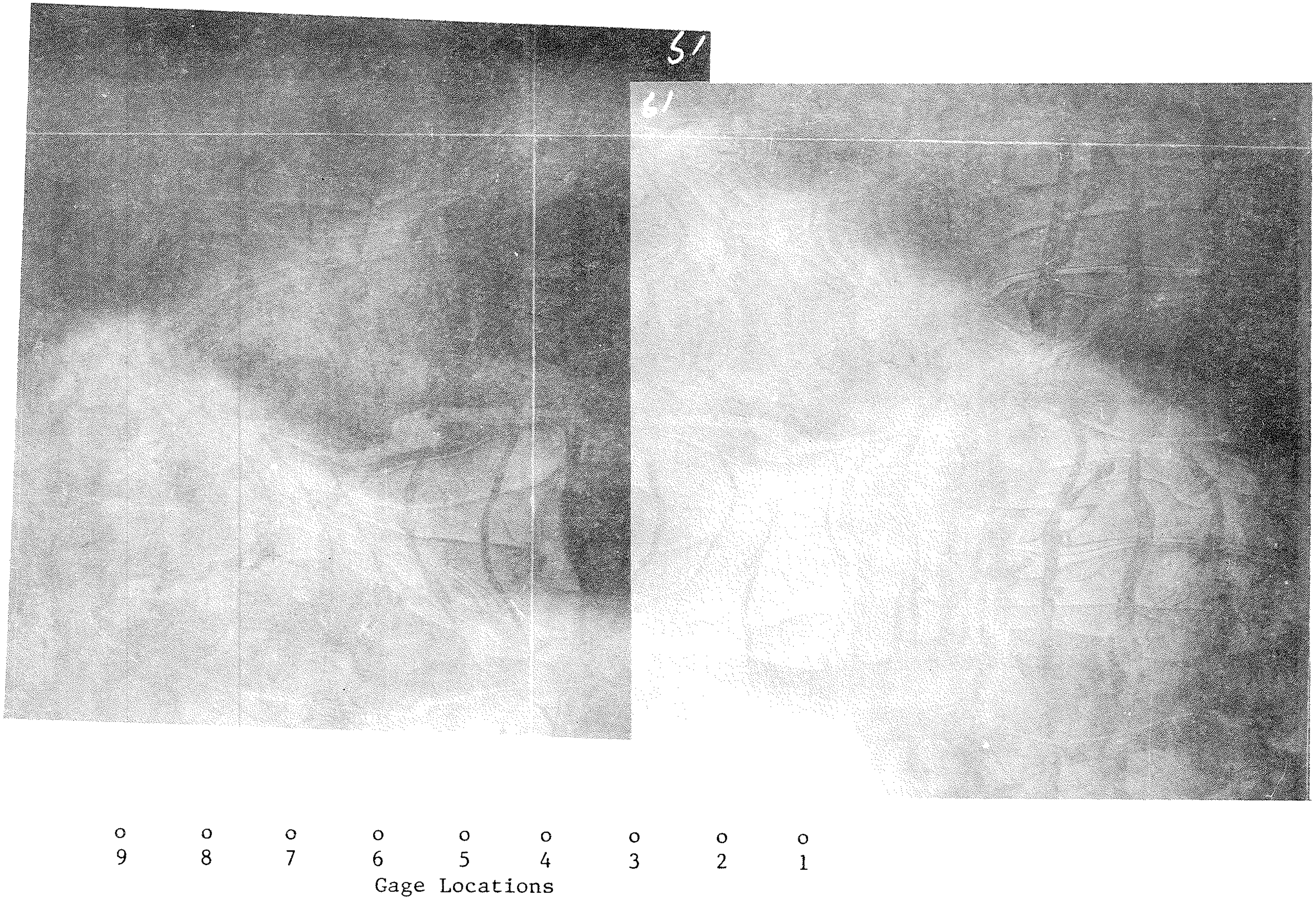

Figure B.11 Experiment CN2015

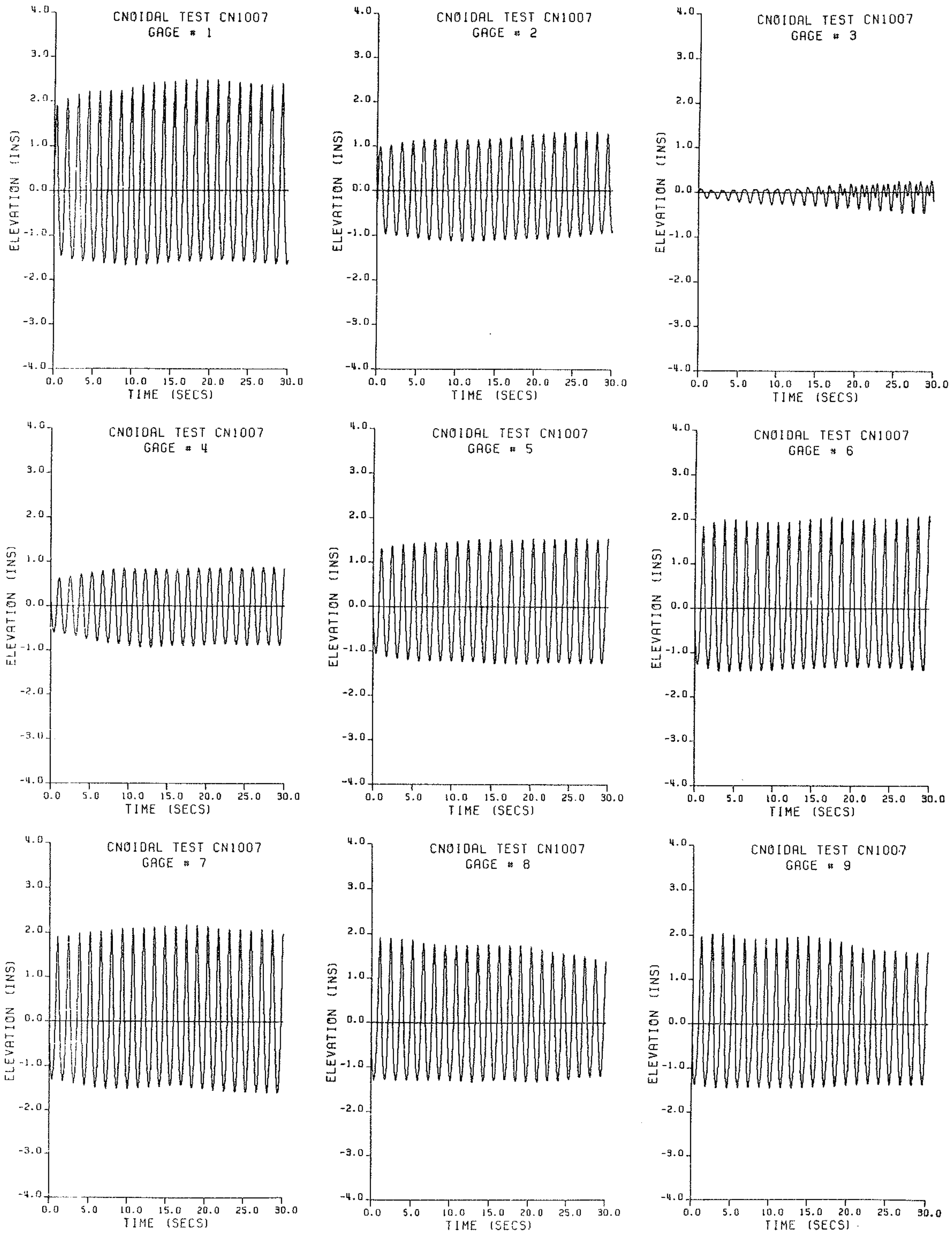

Figure B.2 Experimental wave profiles.

a) Experiment CN1007

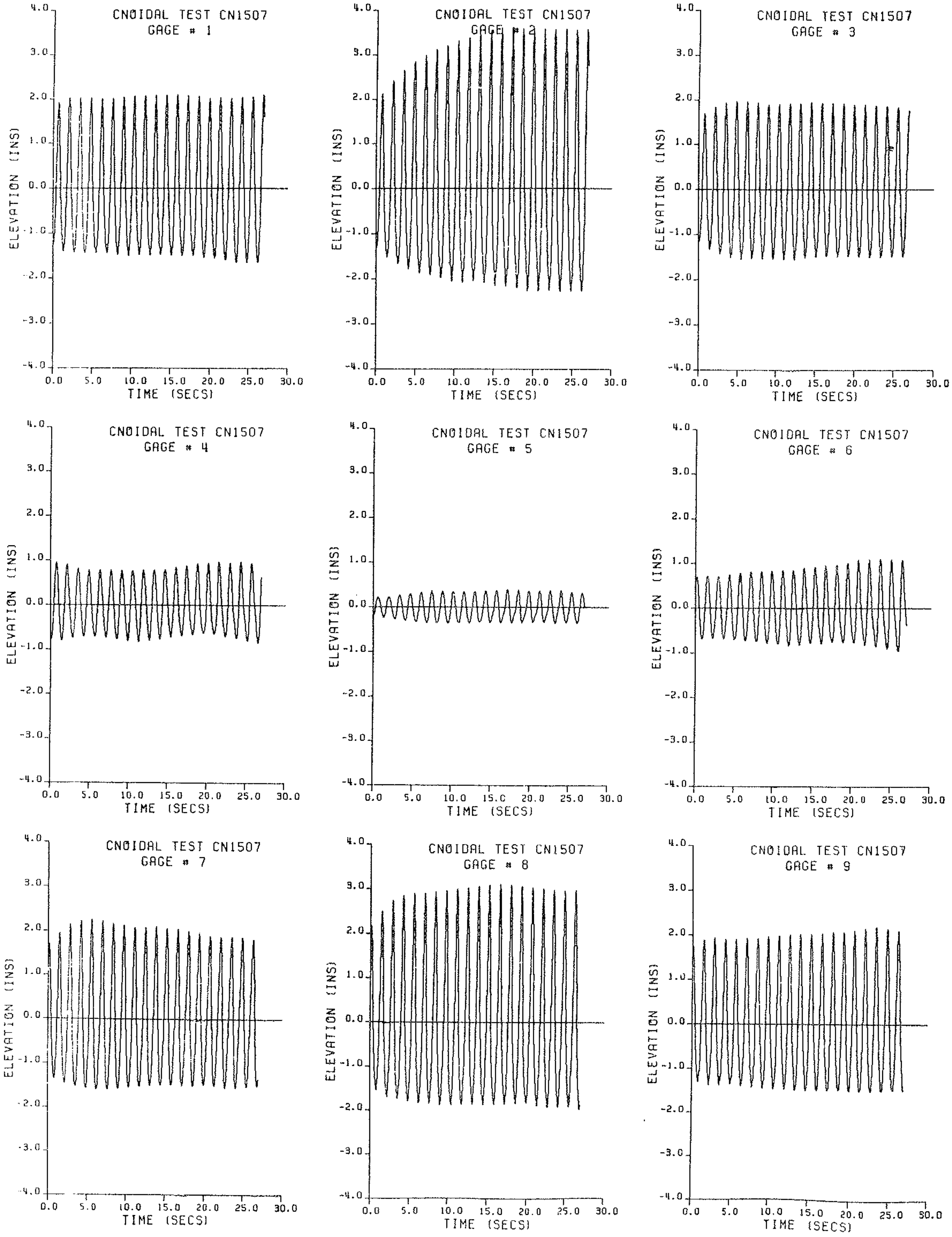

Figure B.2b Experiment CN1507

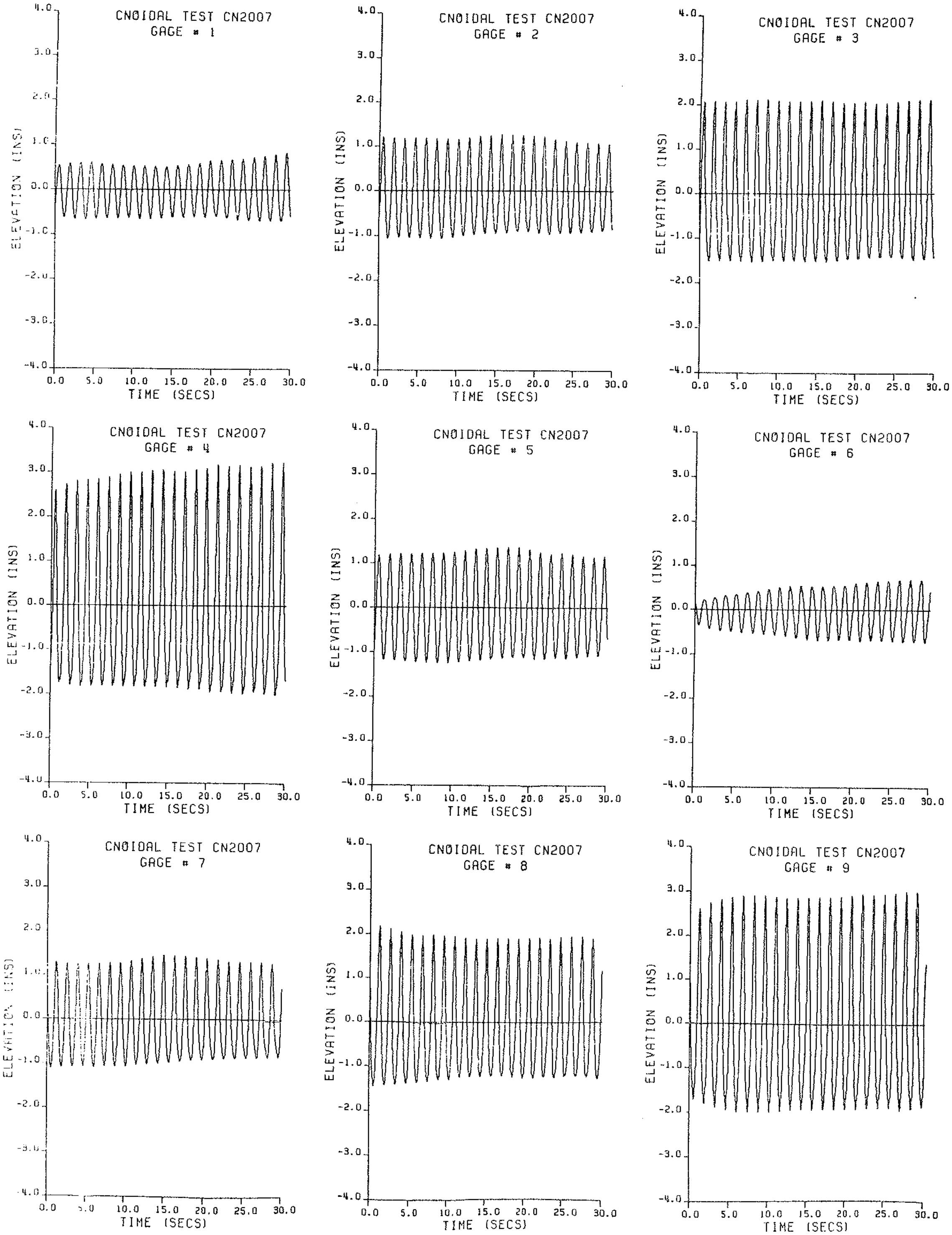

Figure B.2c Experiment CN2007

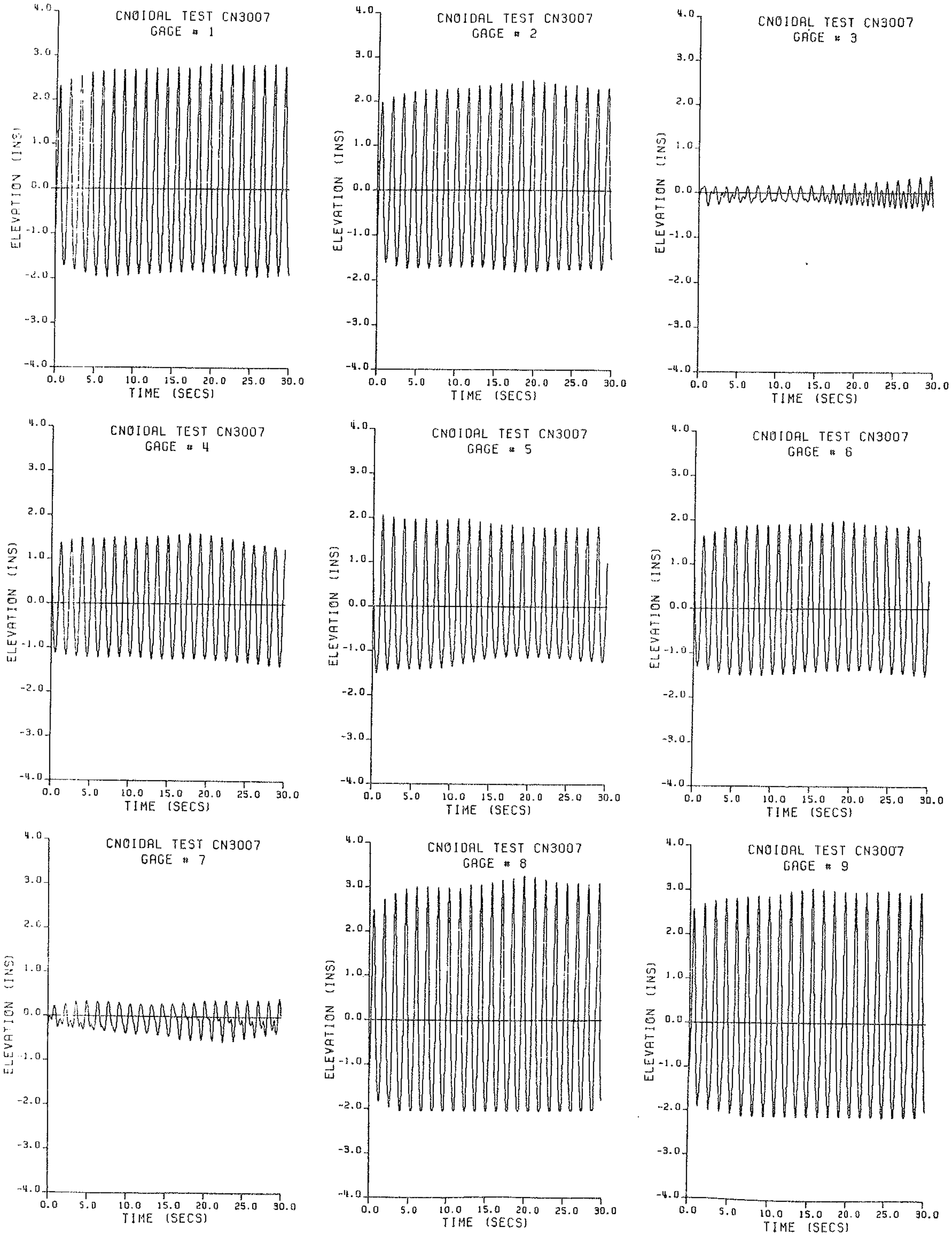

Figure B.2d Experiment CN3007

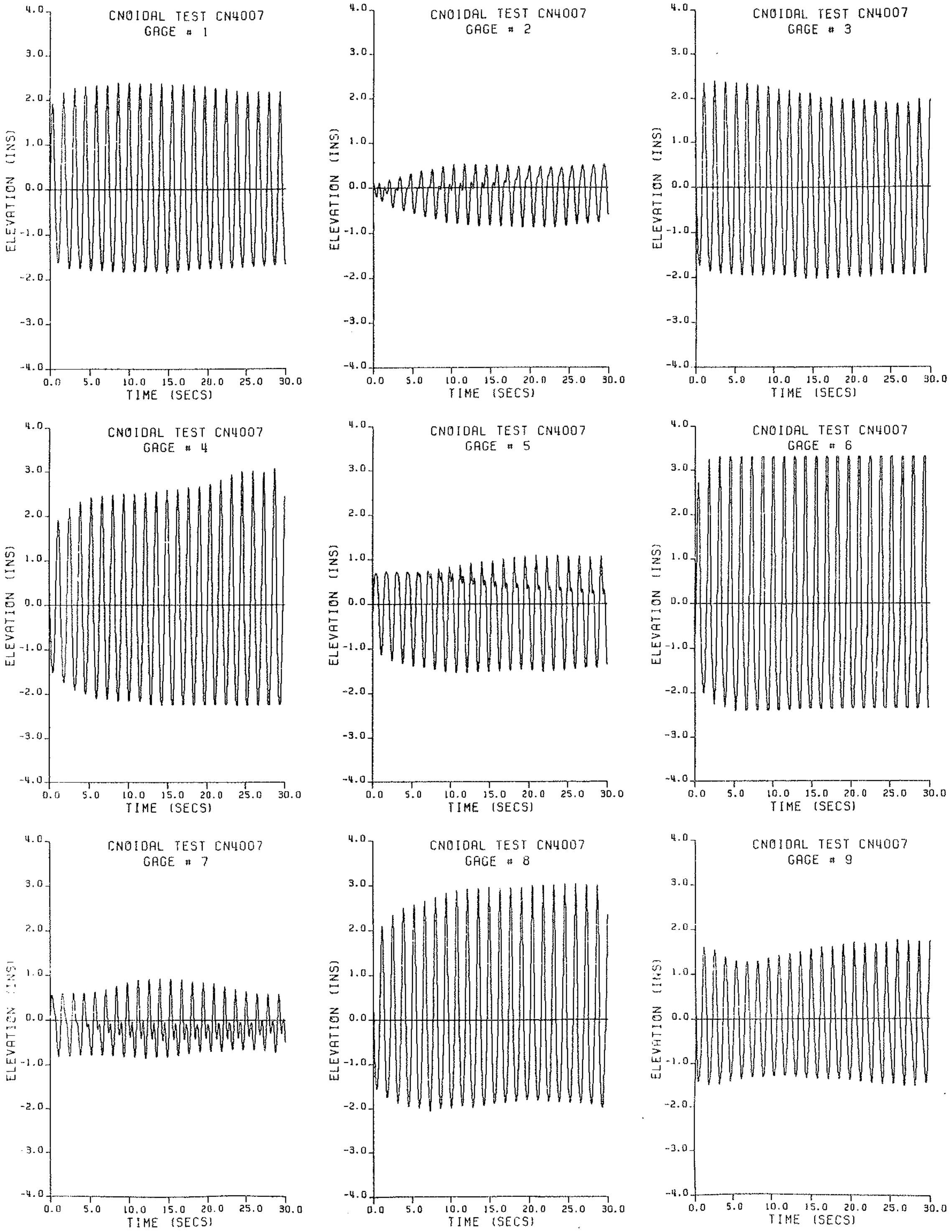

Figure B.2e Experiment CN4007

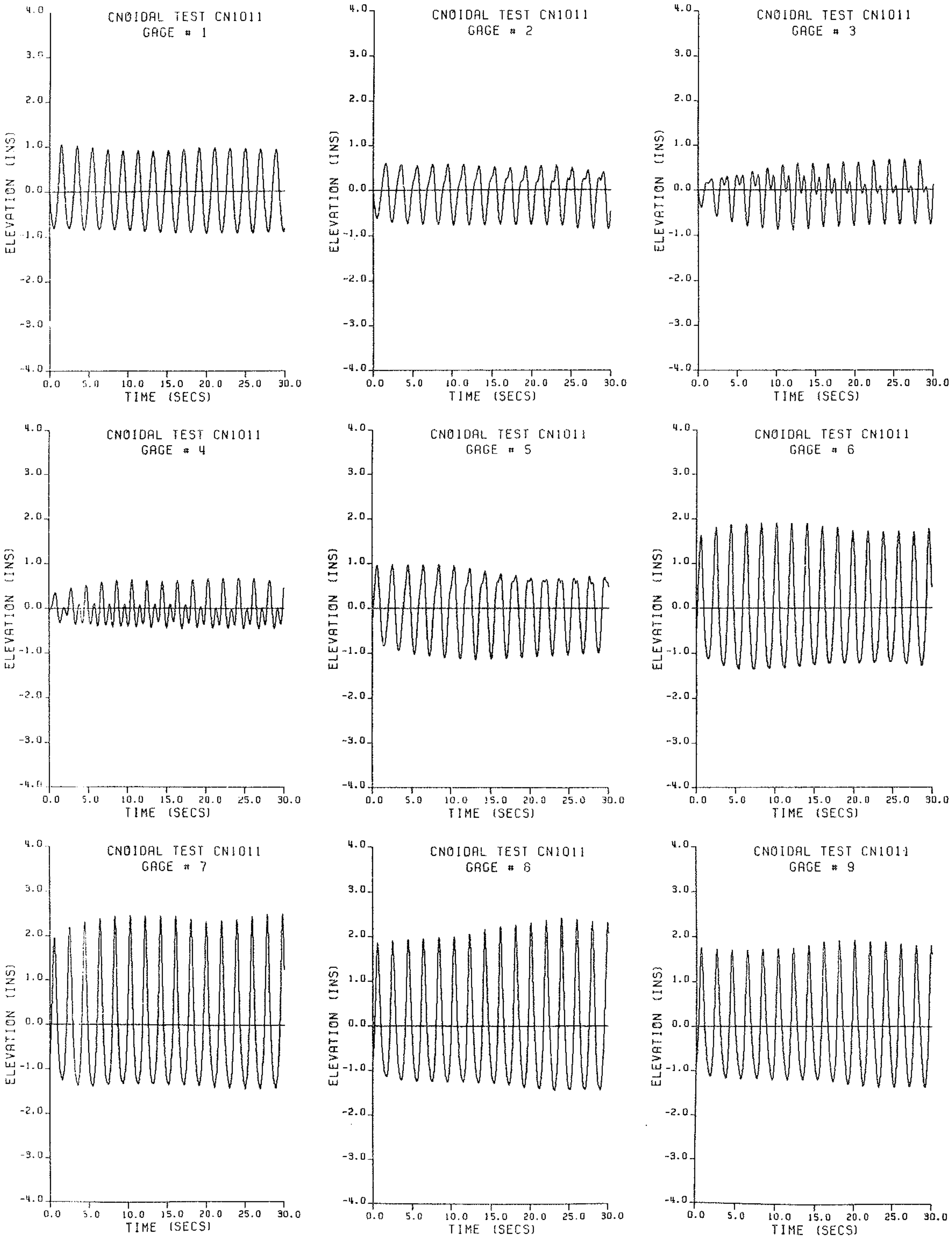

Figure B.2f Experiment CN1011

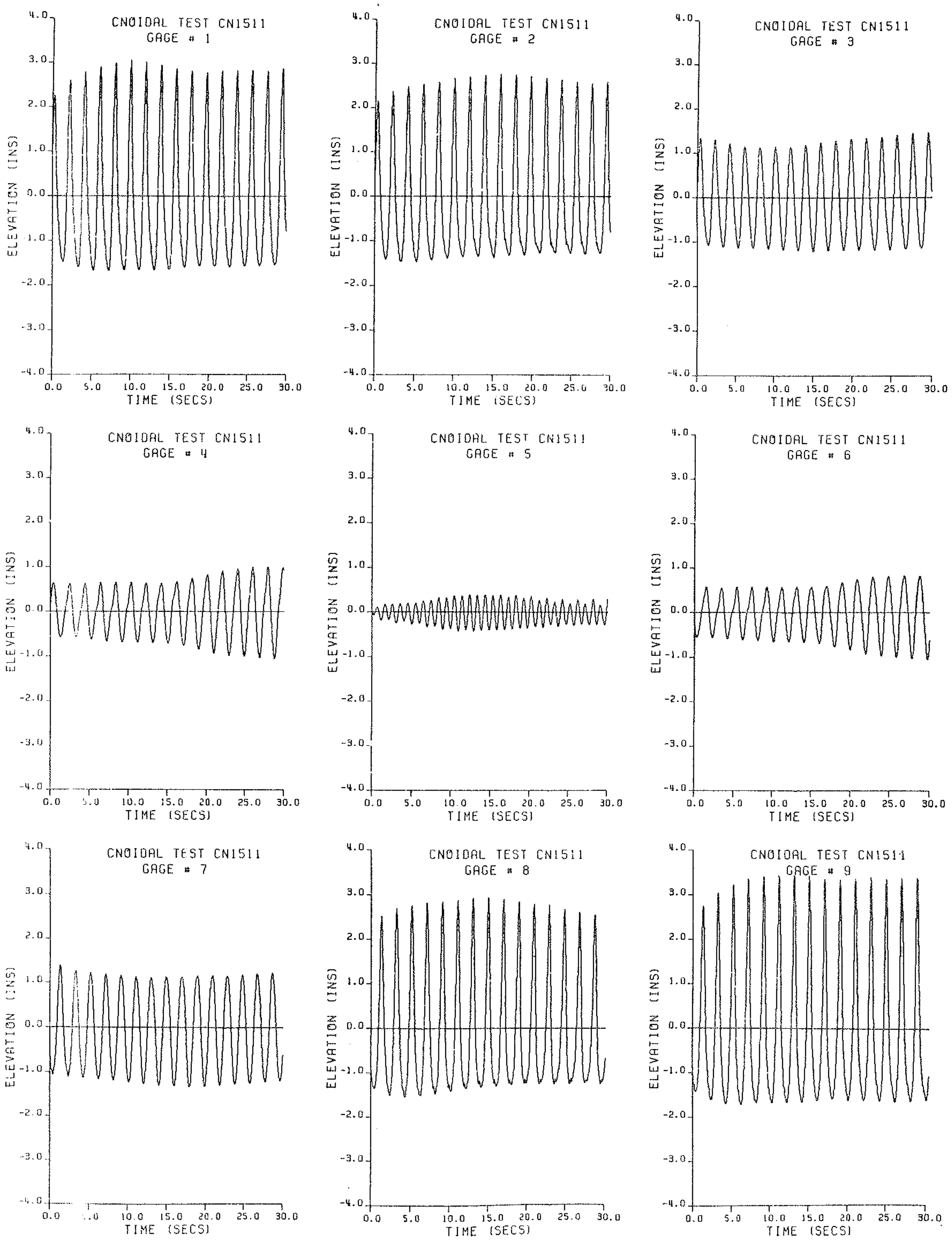

Figure B.2g Experiment CN1511

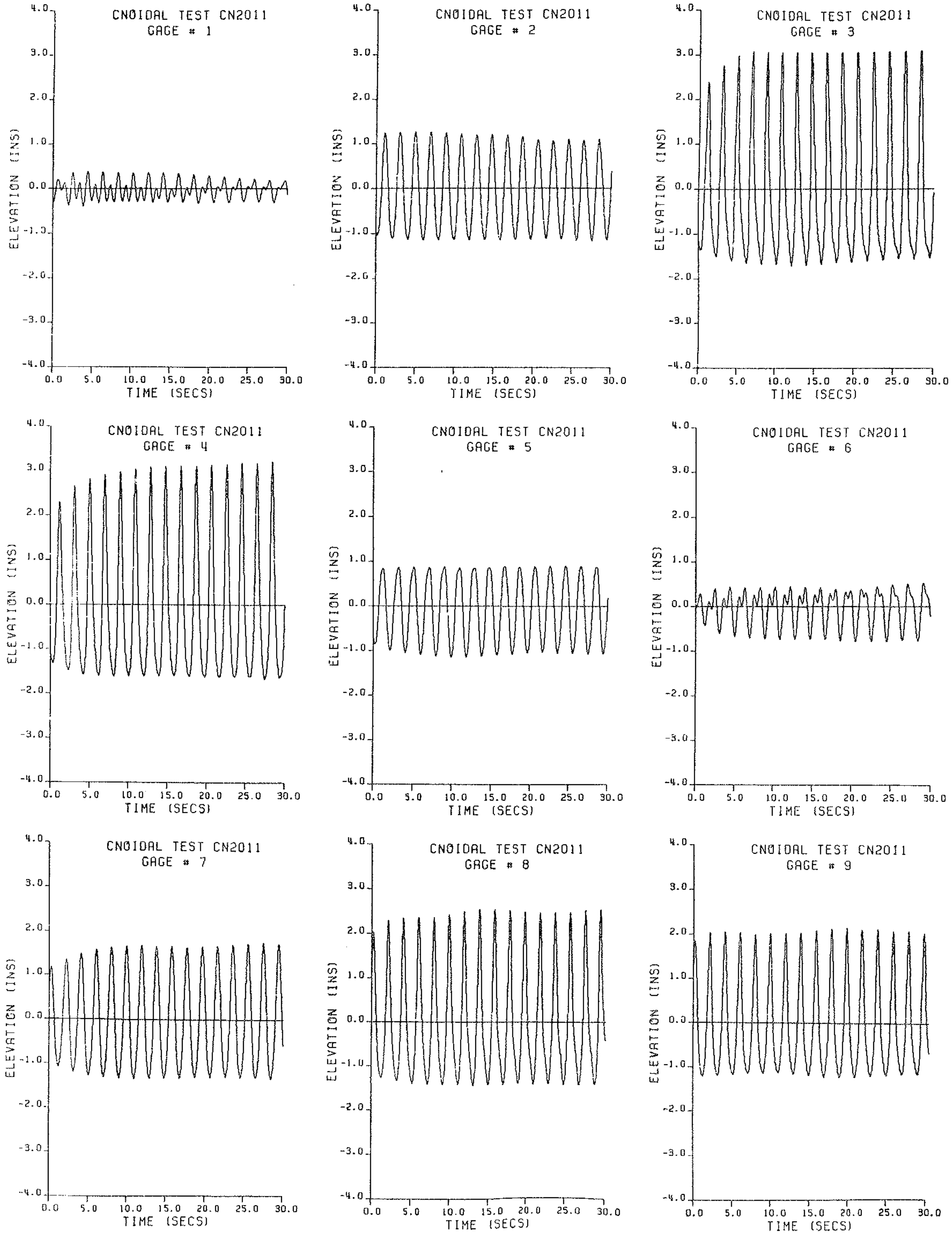

Figure B.2h Experiment CN2011

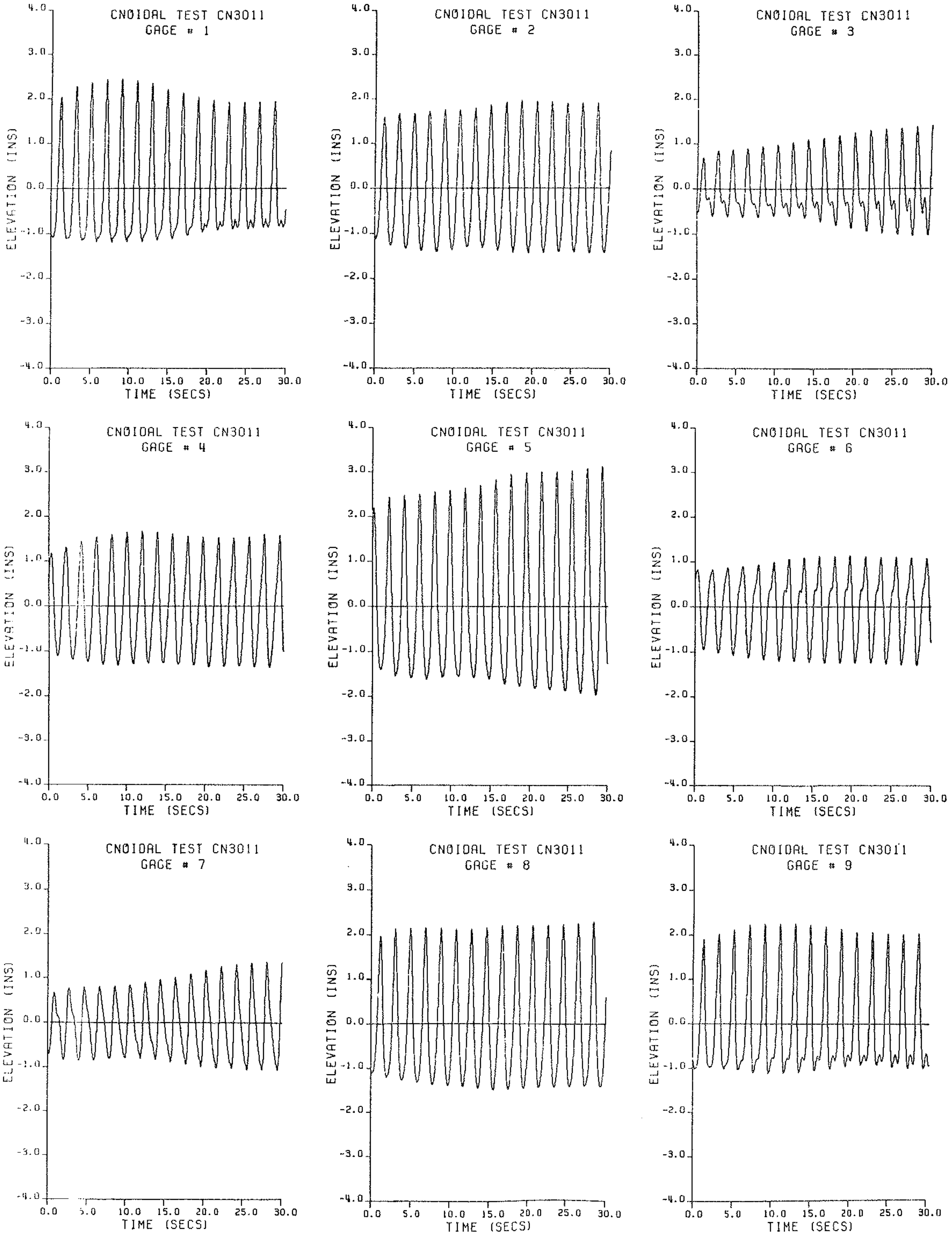

Figure B.2i Experiment CN3011

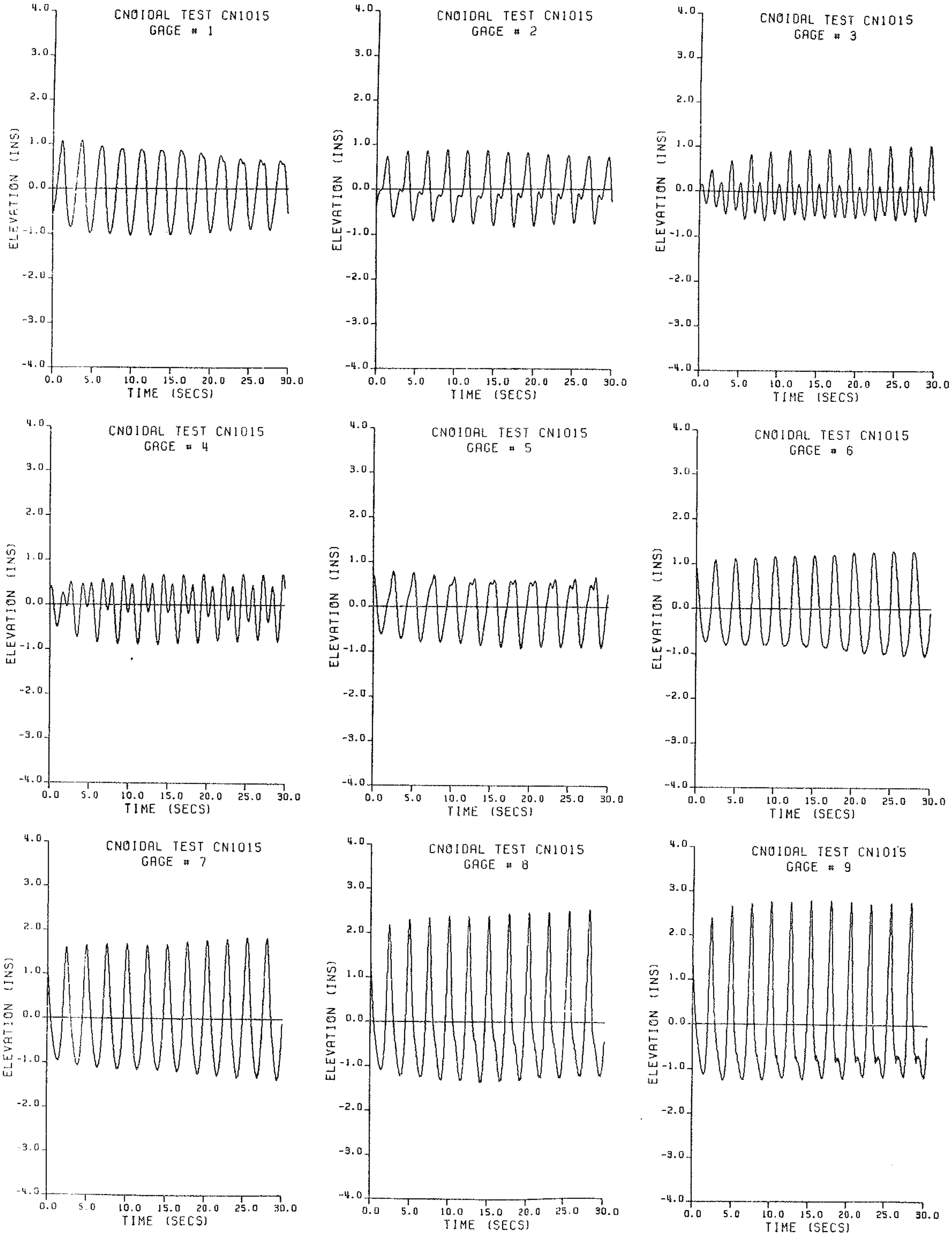

Figure B.2j Experiment CN1015

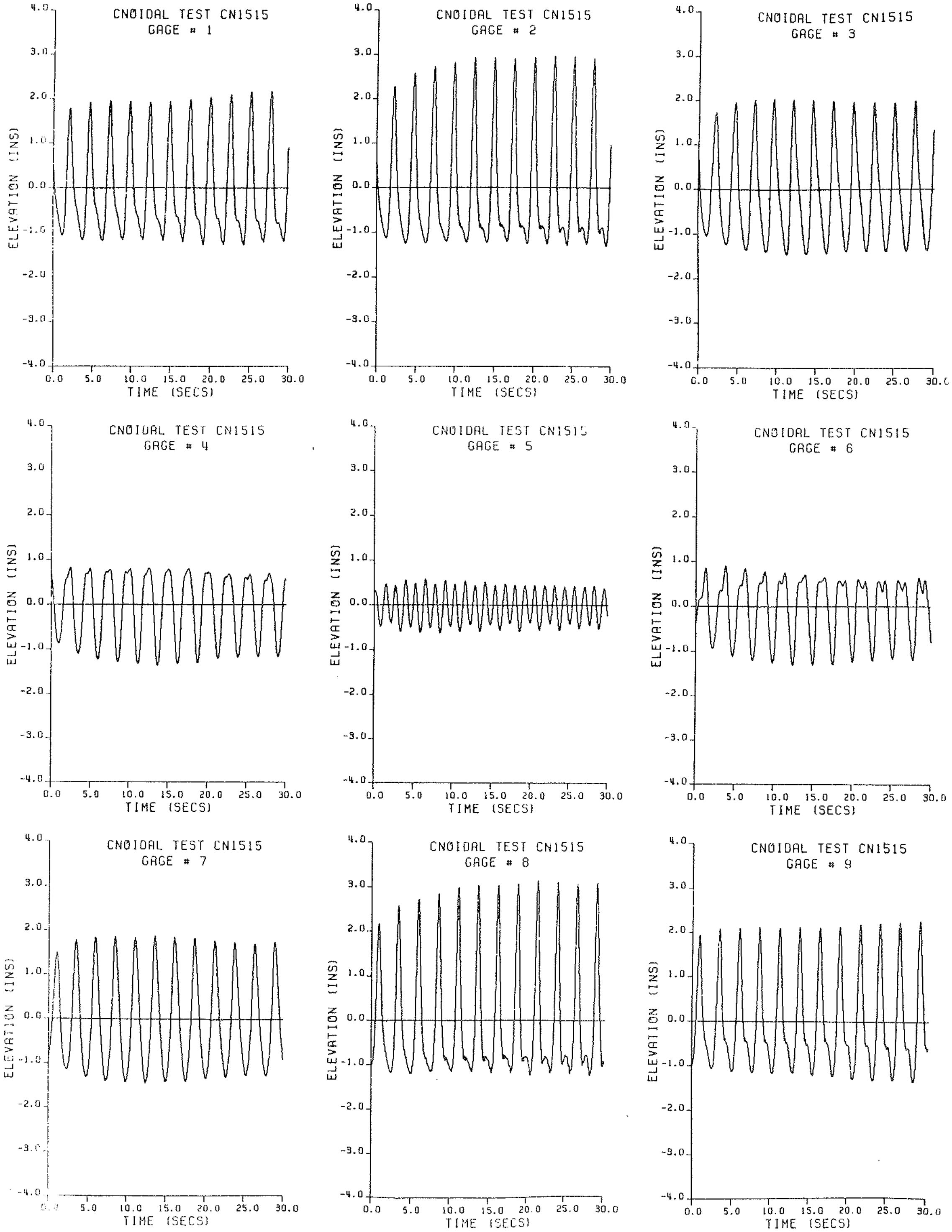

Figure B.2k Experiment CN1515

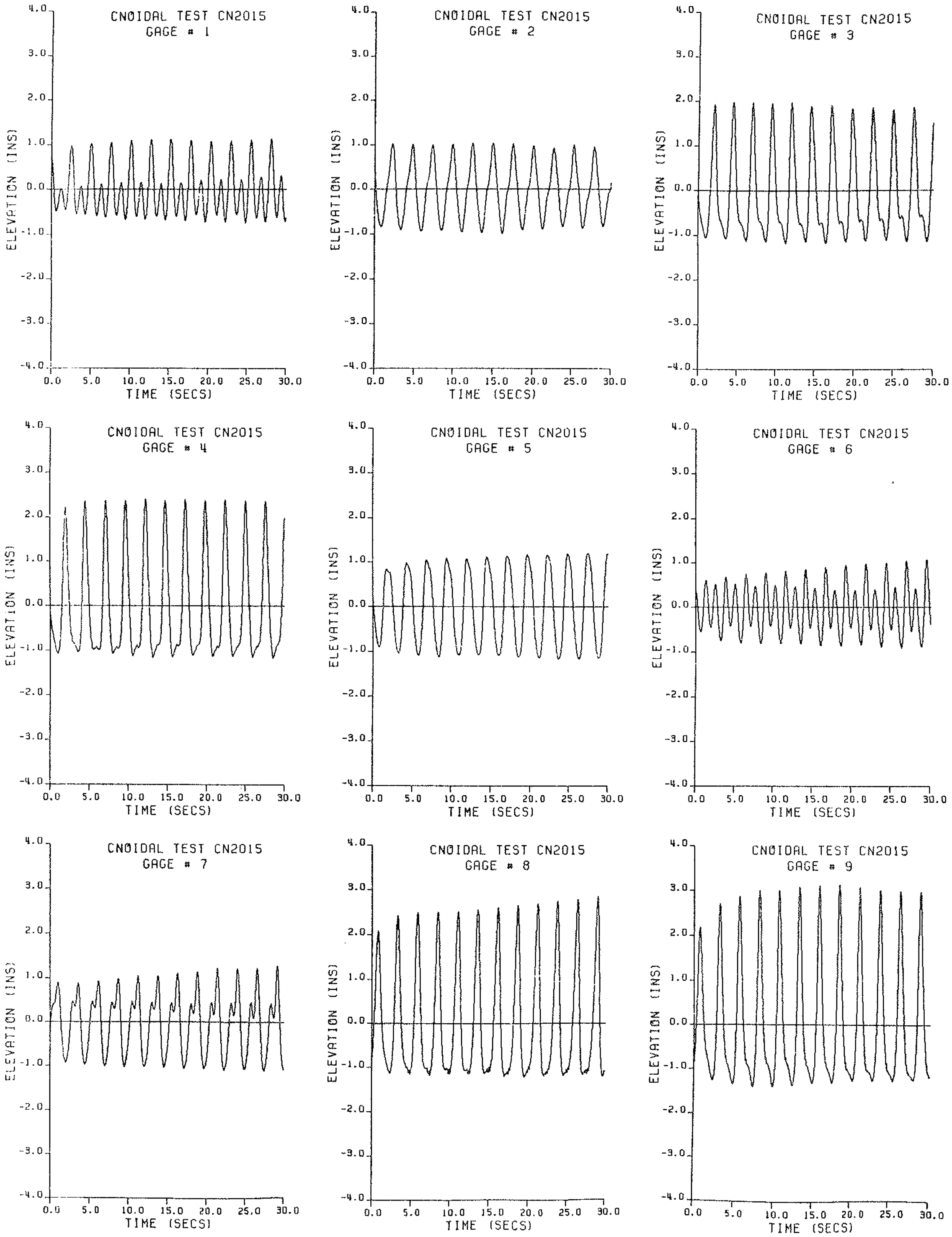

Figure B.21 Experiment CN2015

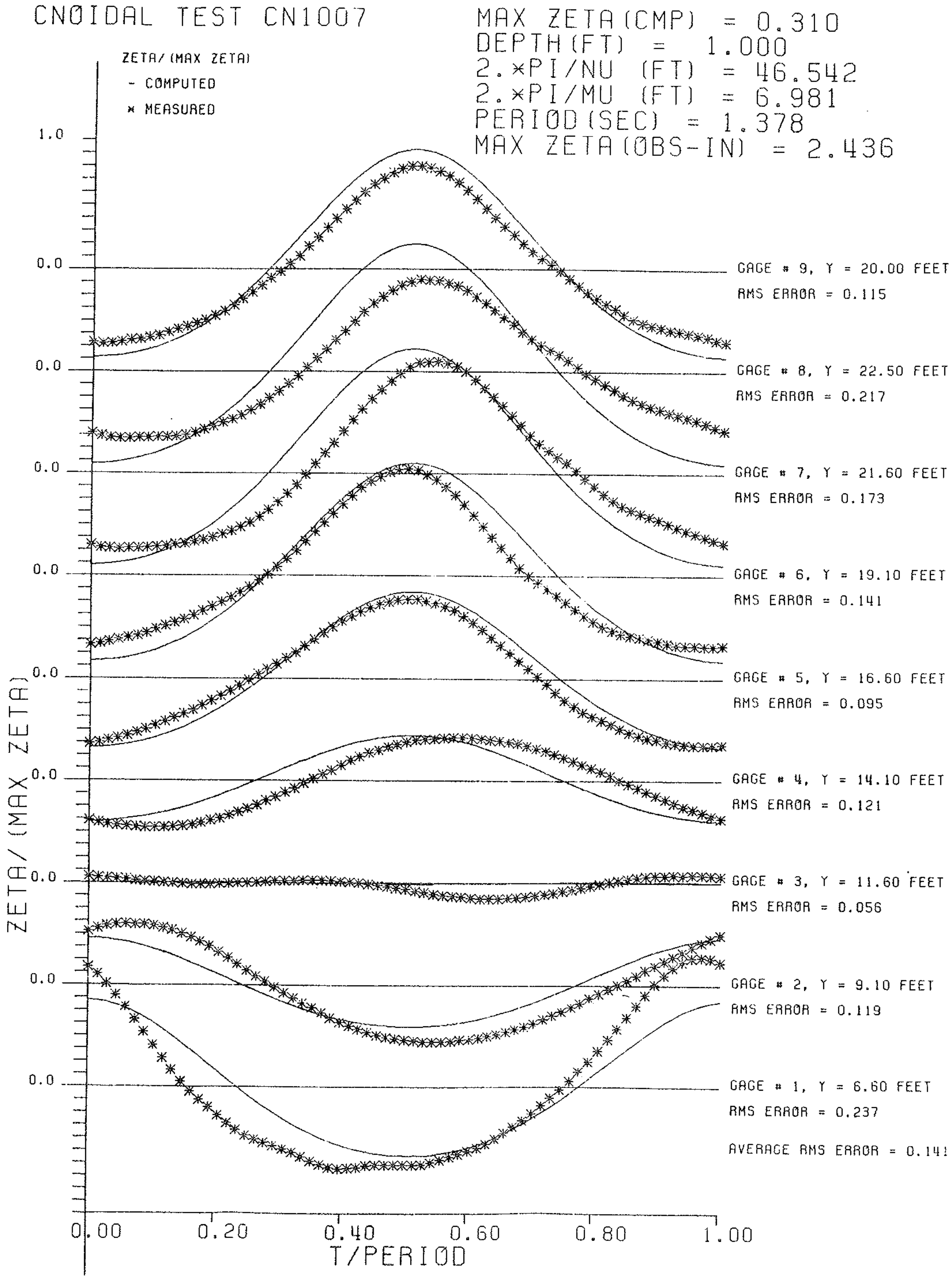

Figure B.3 Theoretical and experimental wave profiles.

a) Experiment CN1007

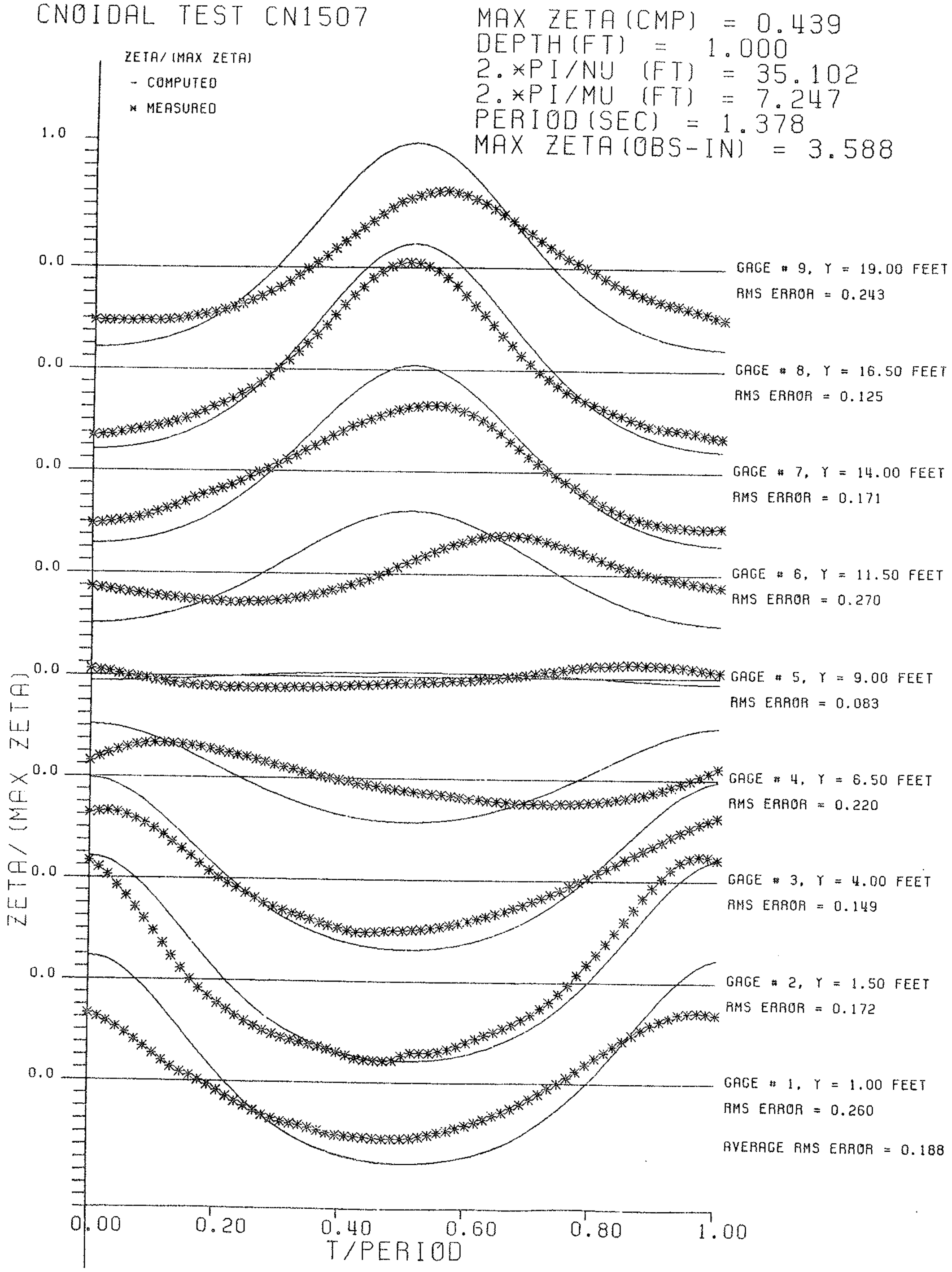

Figure B.3b Experiment CN1507

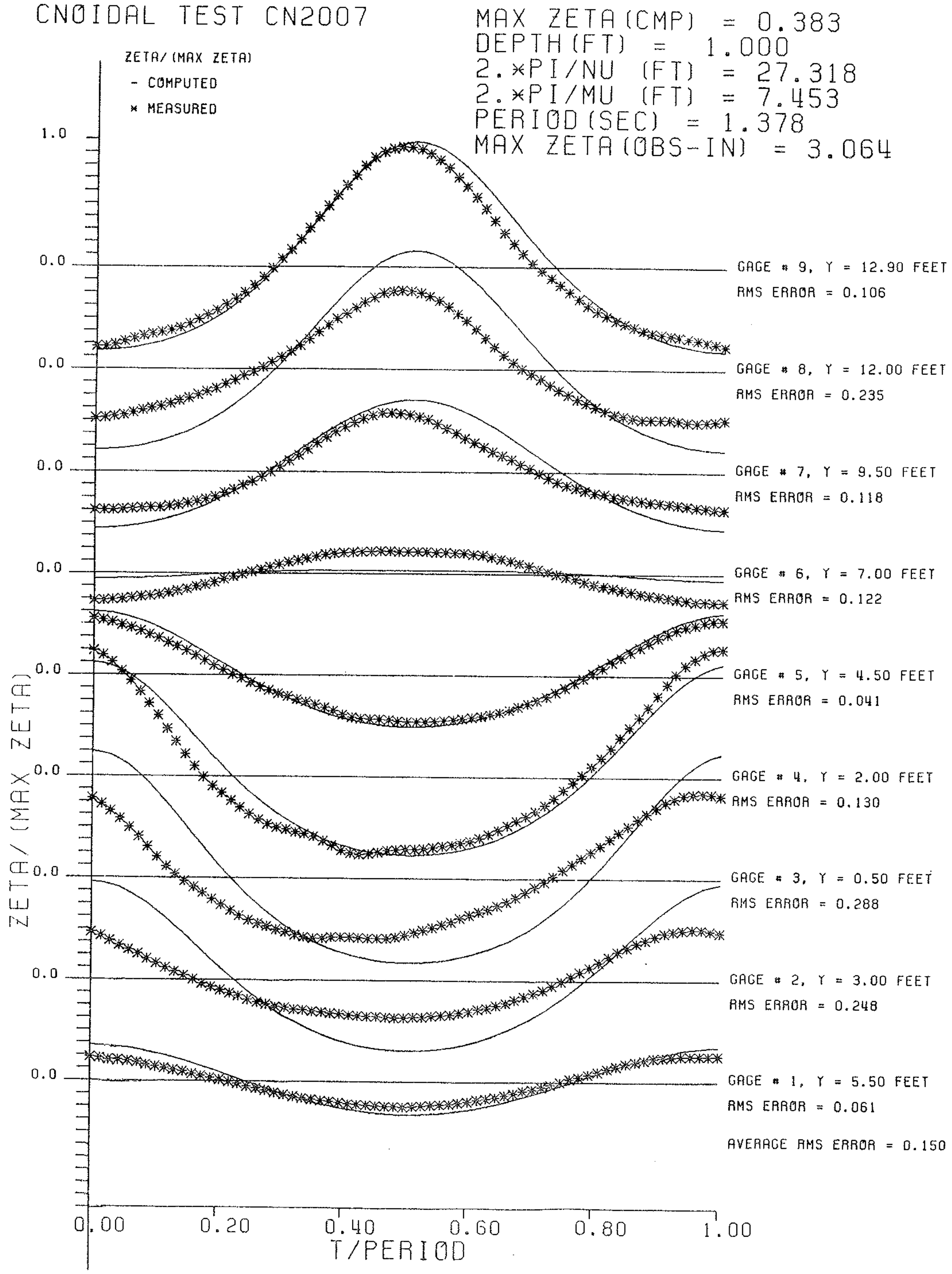

Figure B.3c Experiment CN2007

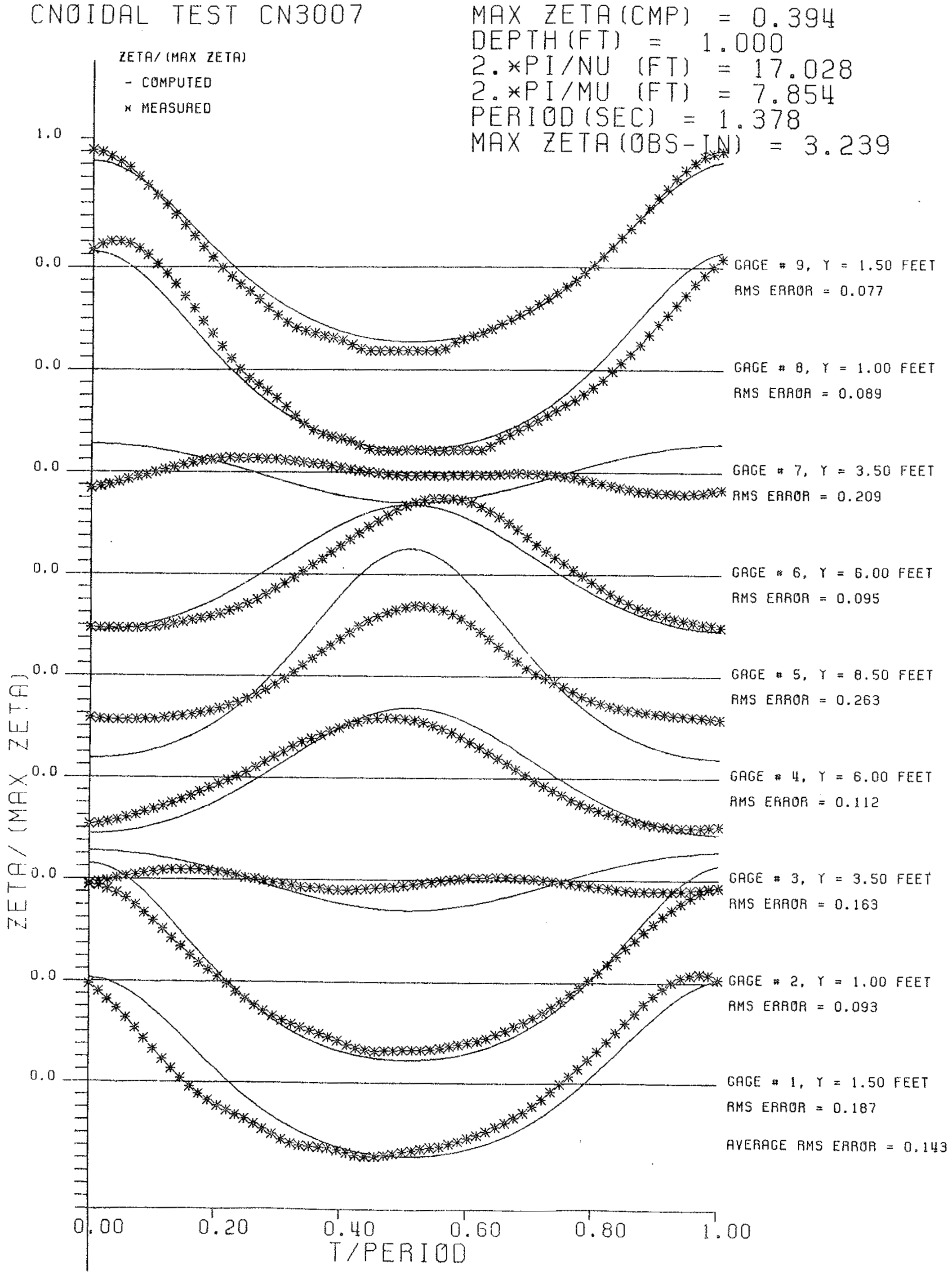

Figure B.3d Experiment CN3007

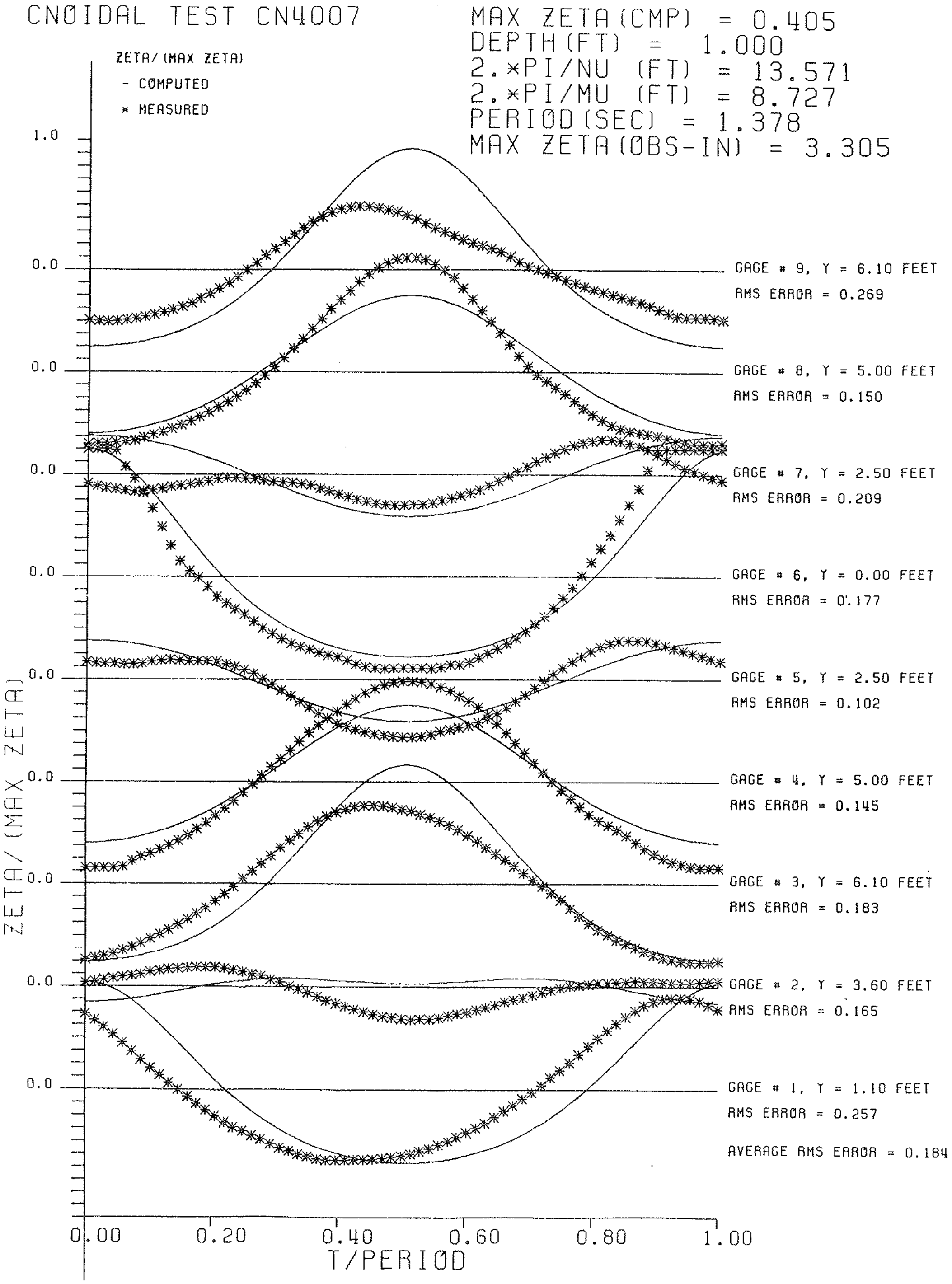

Figure B.3e Experiment CN4007

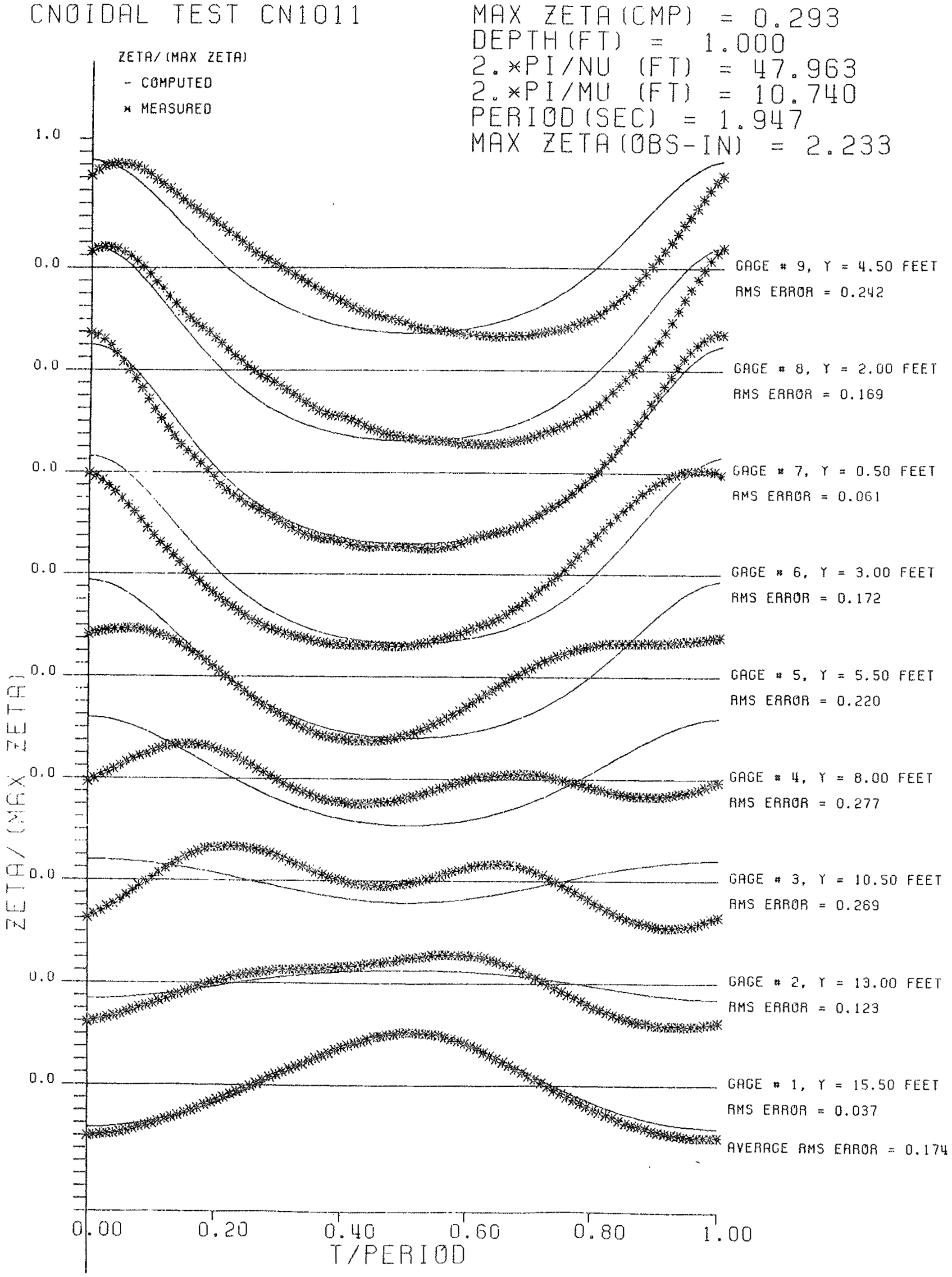

Figure B.3f Experiment CN1011

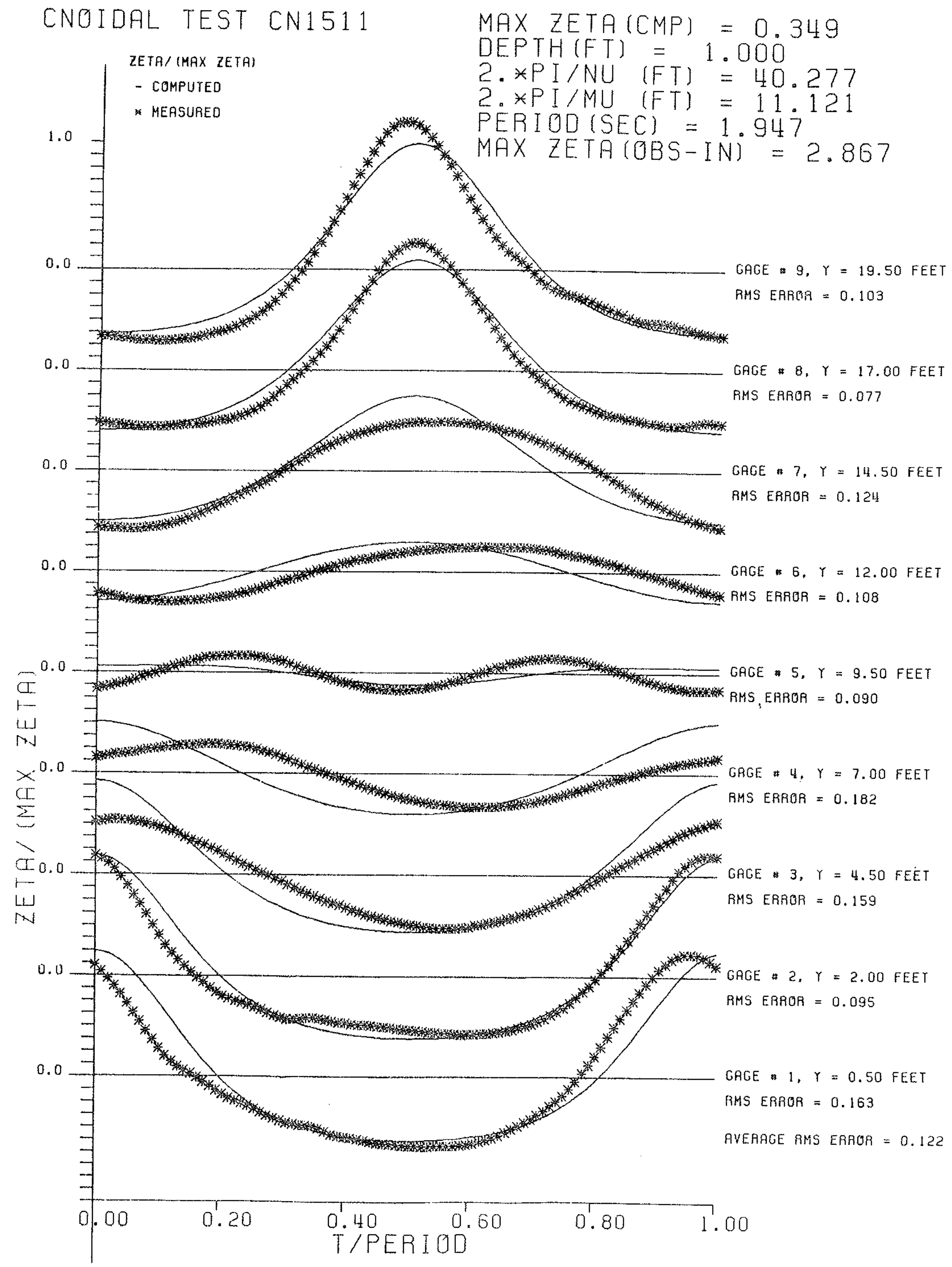

Figure B.3g Experiment CN1511

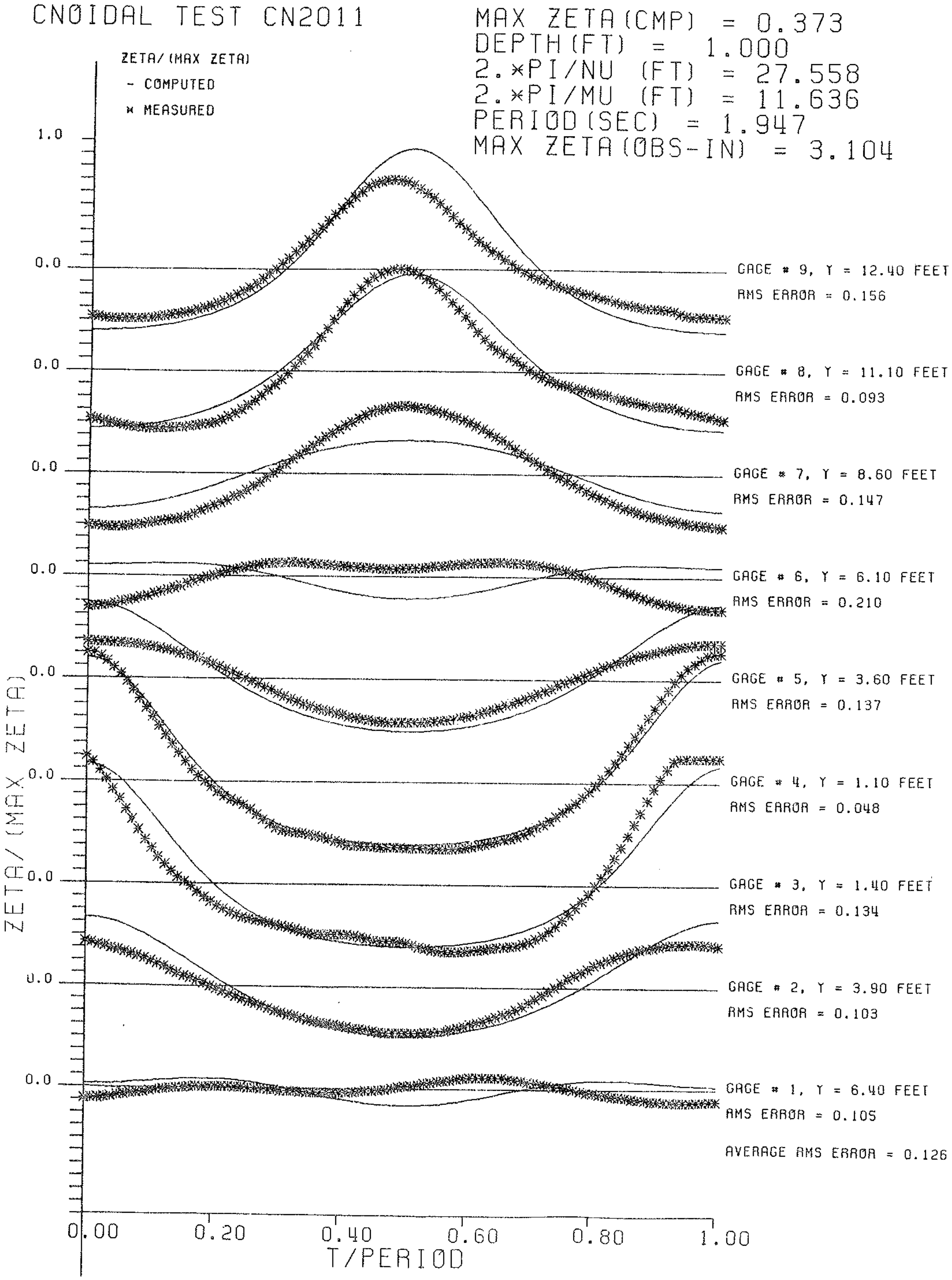

Figure B.3h Experiment CN2011

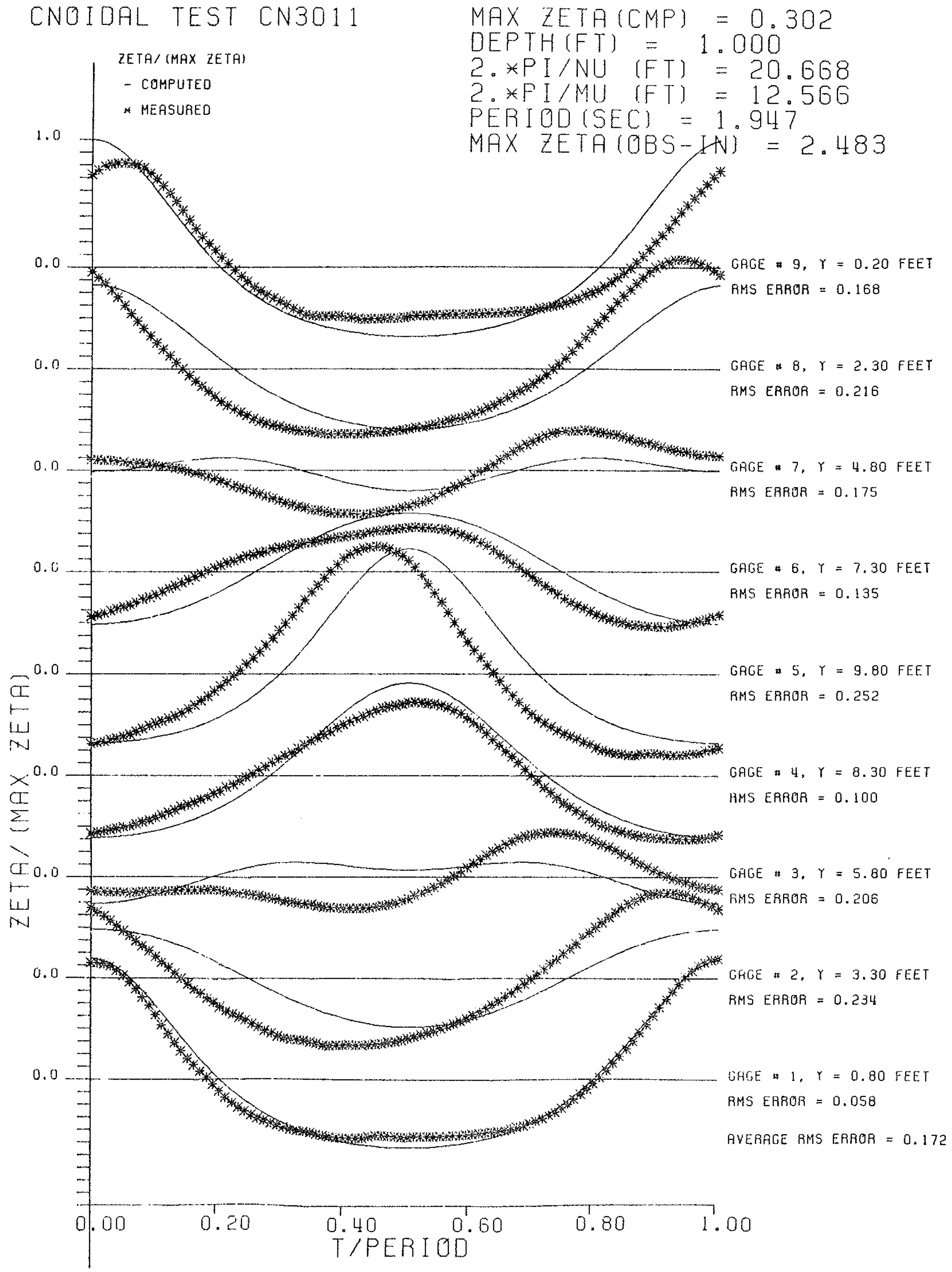

Figure B.3i Experiment CN3011

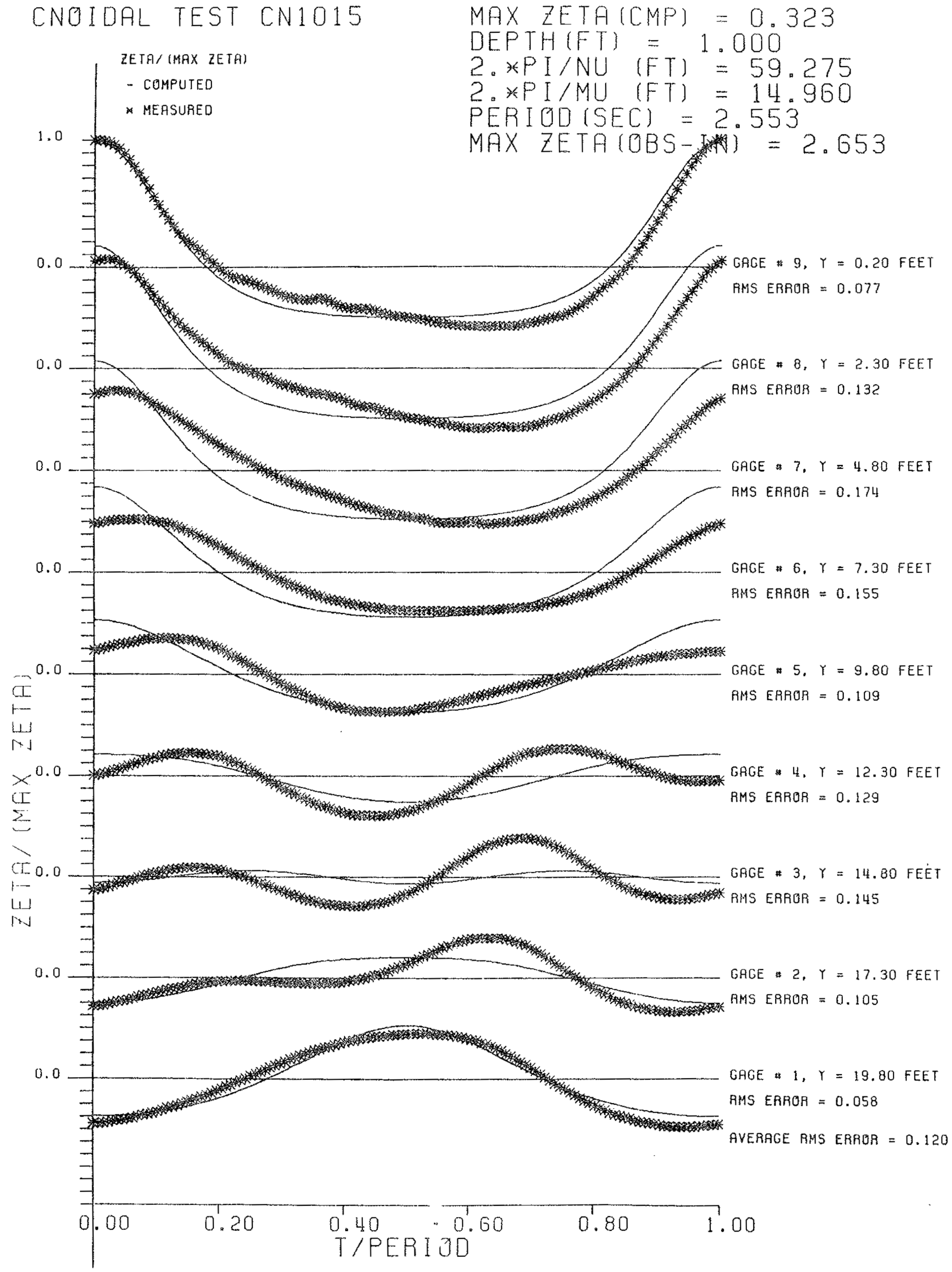

Figure B.3j Experiment CN1015

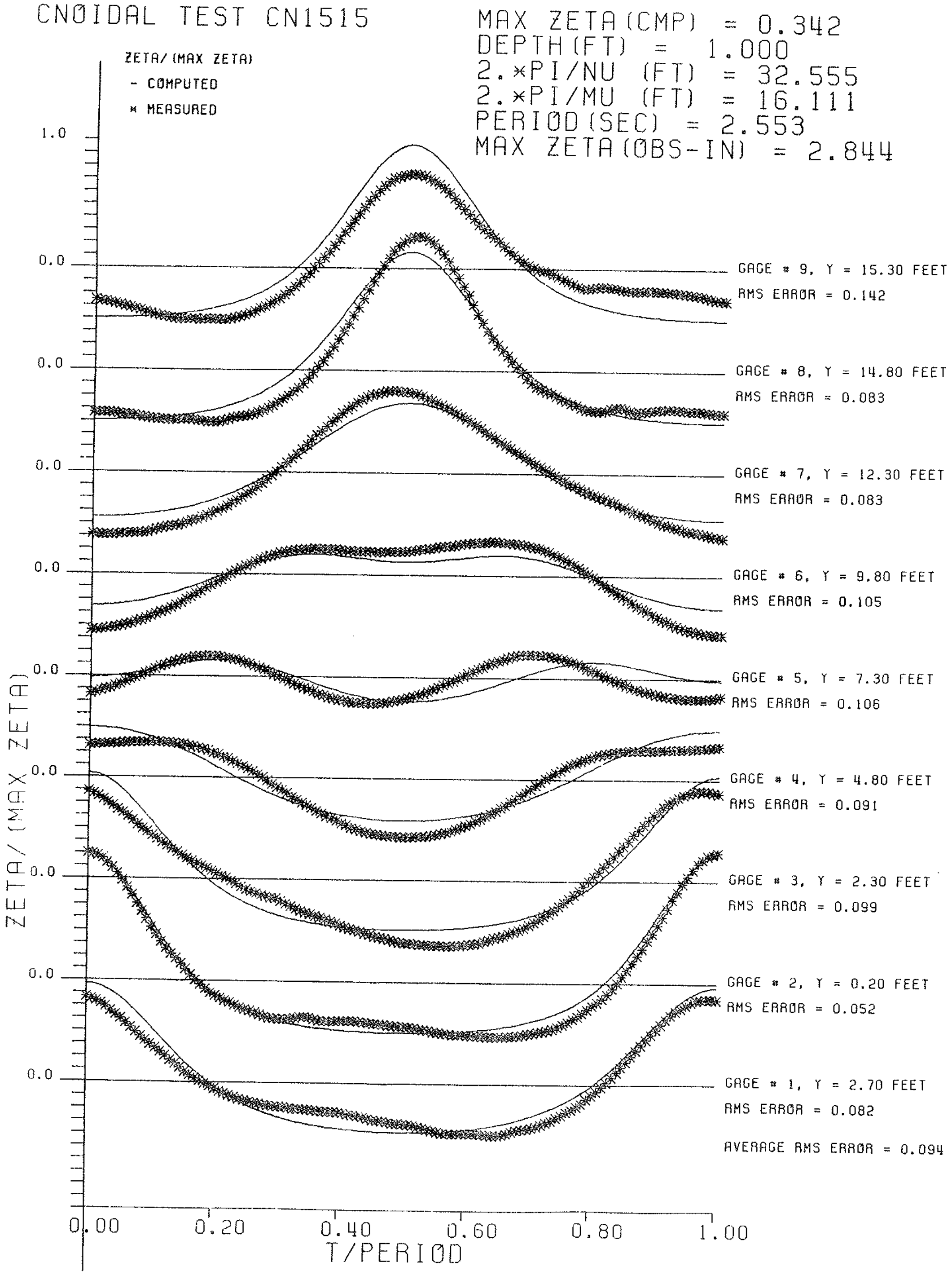

Figure B.3k Experiment CN1515

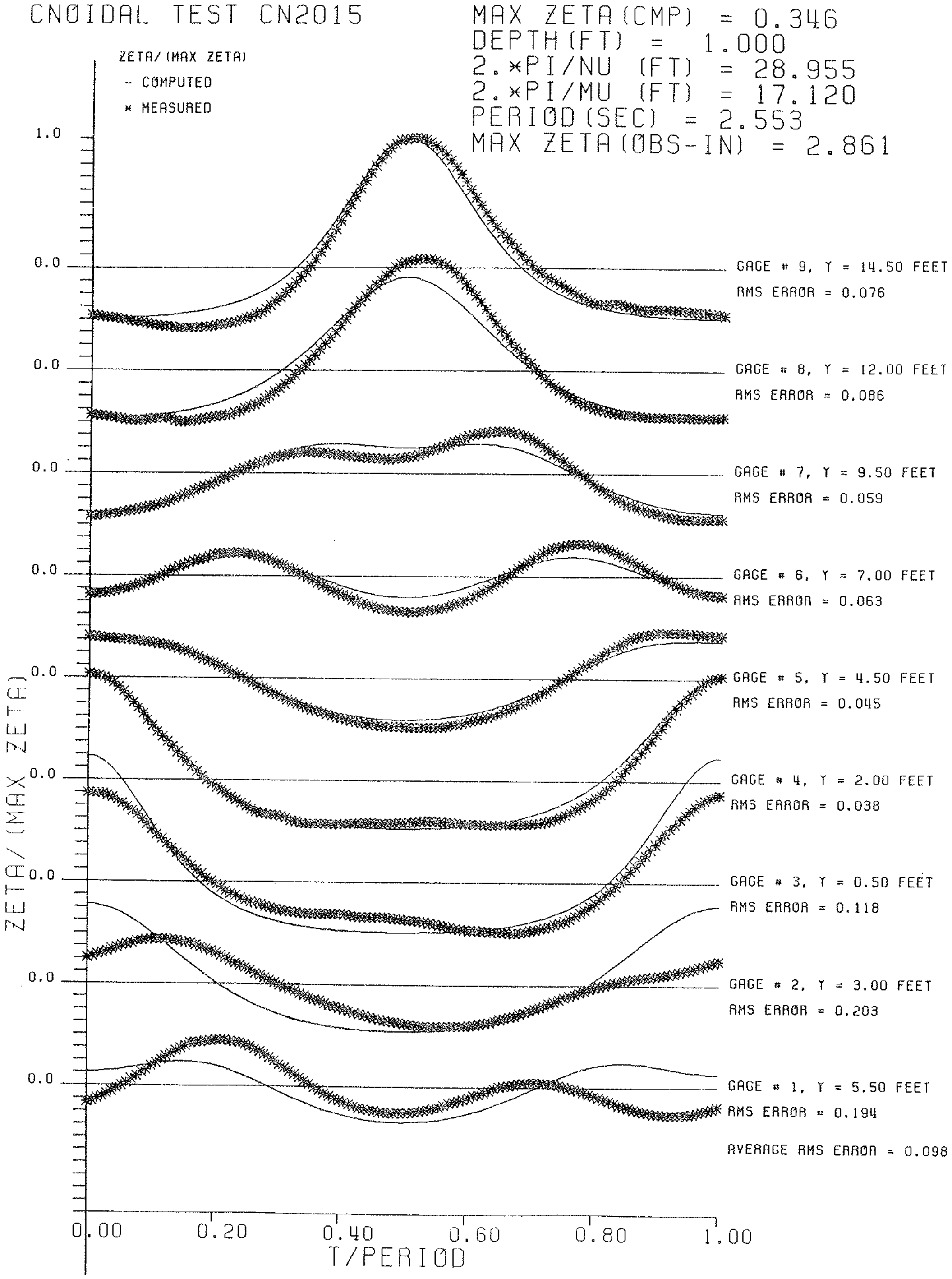

Figure B.31 Experiment CN2015

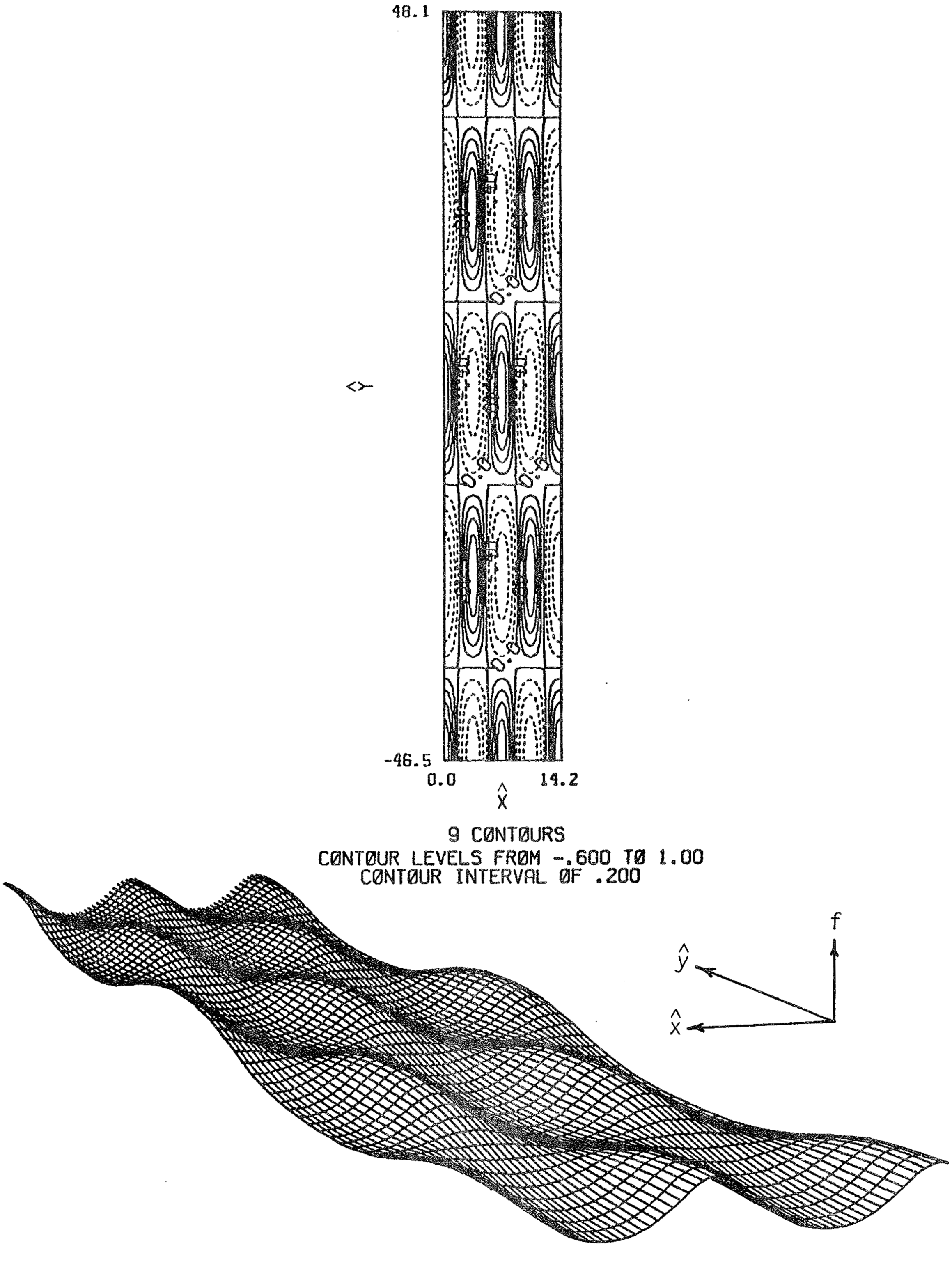

Figure B.4 Normalized contour map and three-dimensional view of the KP solutions for the experimental waves.

a) Experiment CN1007

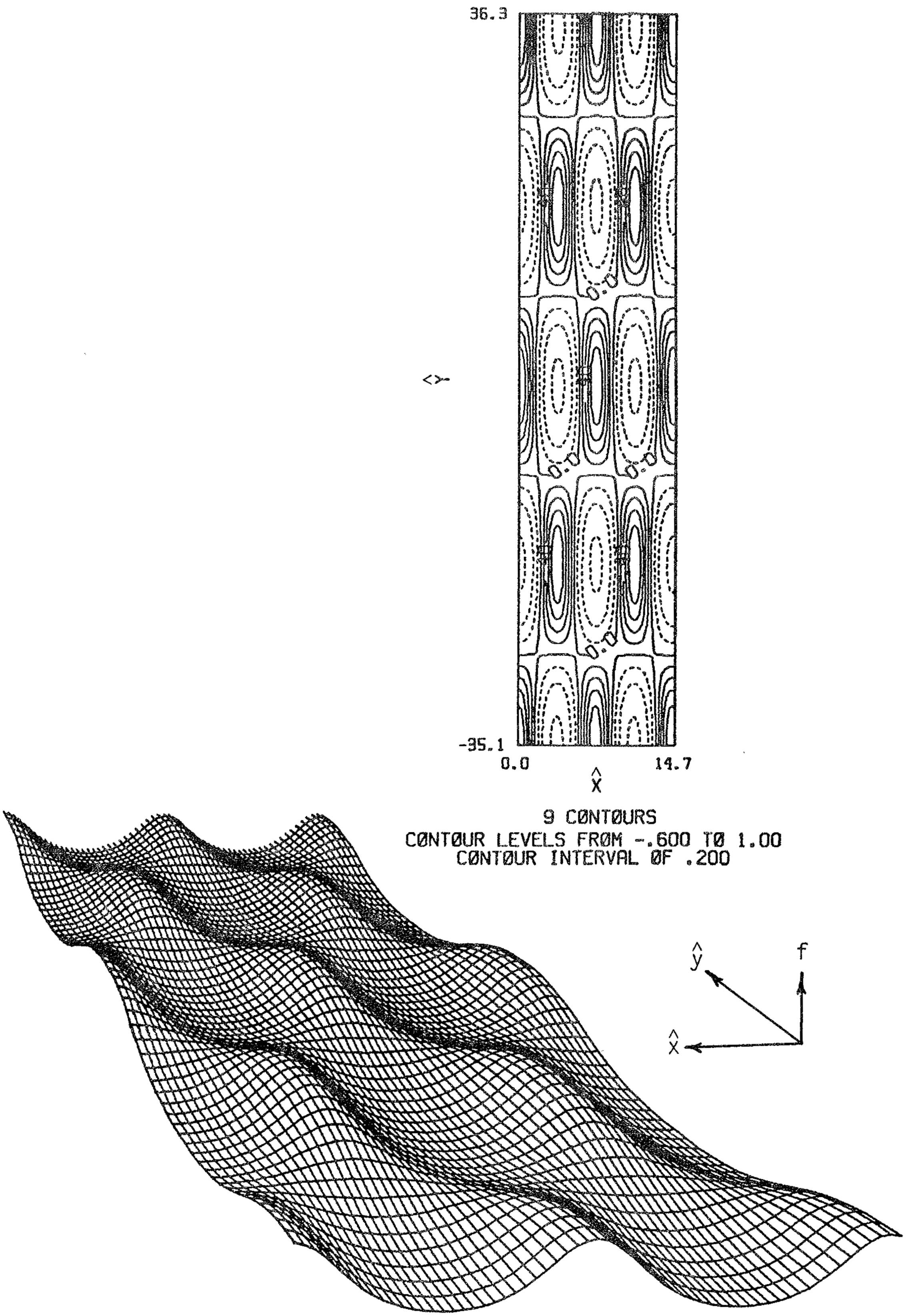

Figure B.4b Experiment CN1507

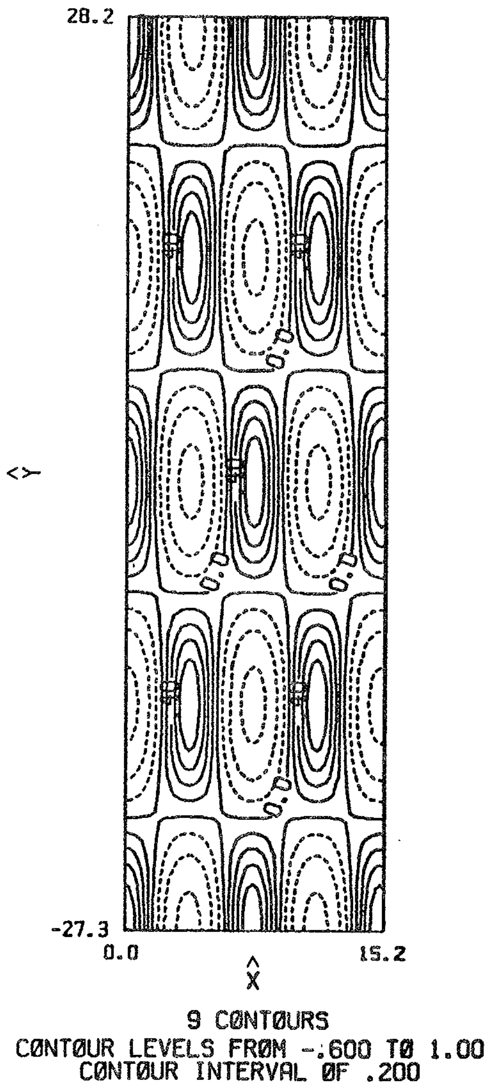

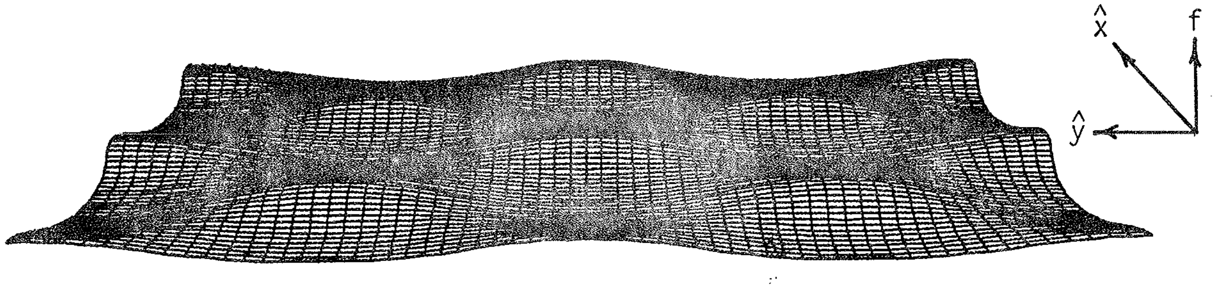

Figure B.4c Experiment CN2007

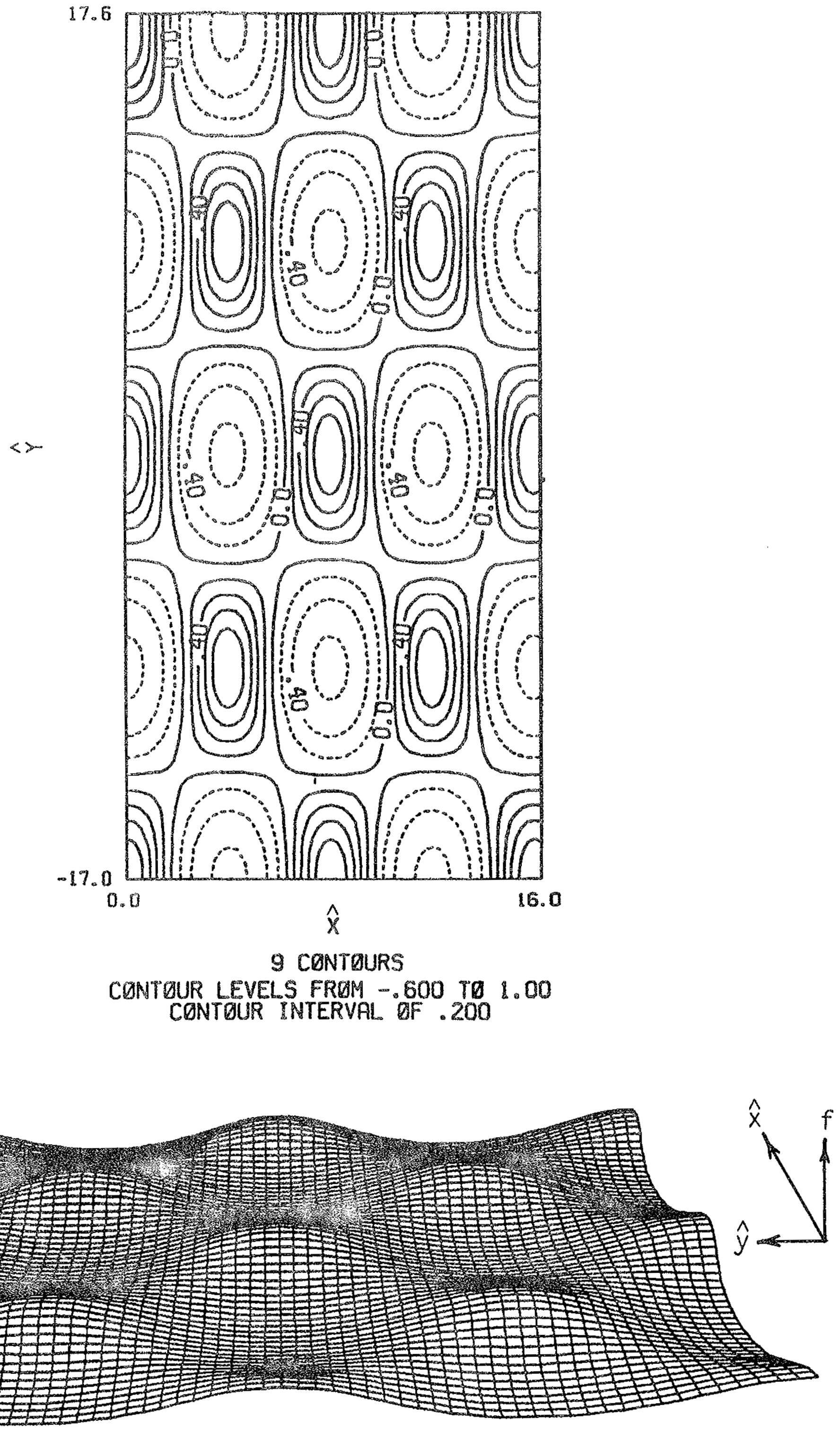

Figure B.4d Experiment CN3007

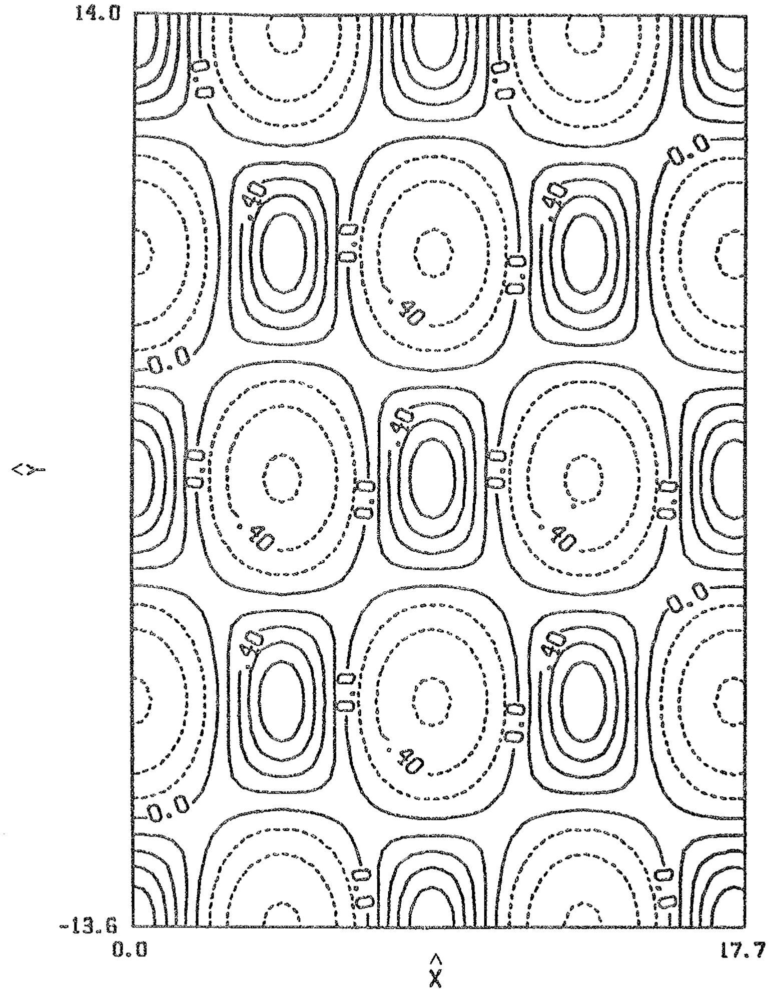

9 CONTOURS
CONTOUR LEVELS FROM -.600 TO 1.00
CONTOUR INTERVAL OF .200

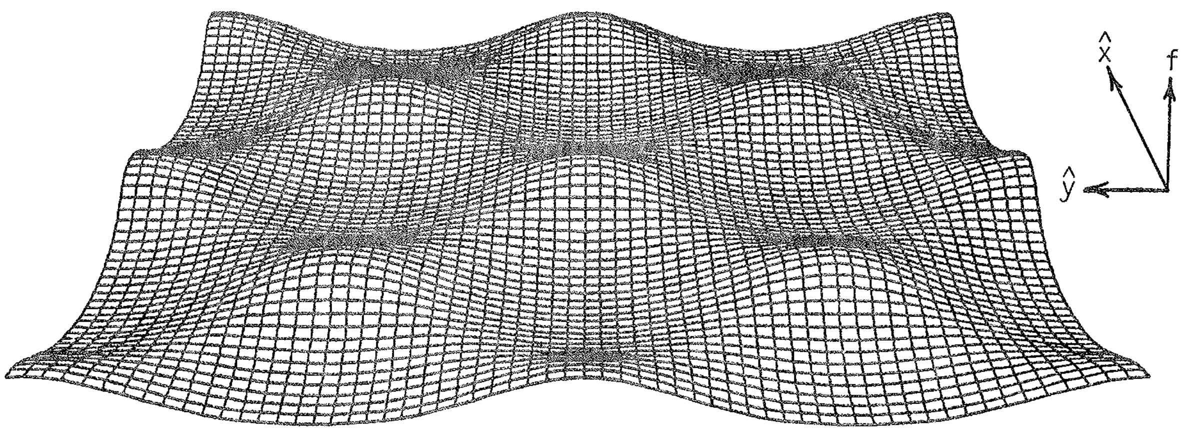

Figure B.4e Experiment CN4007

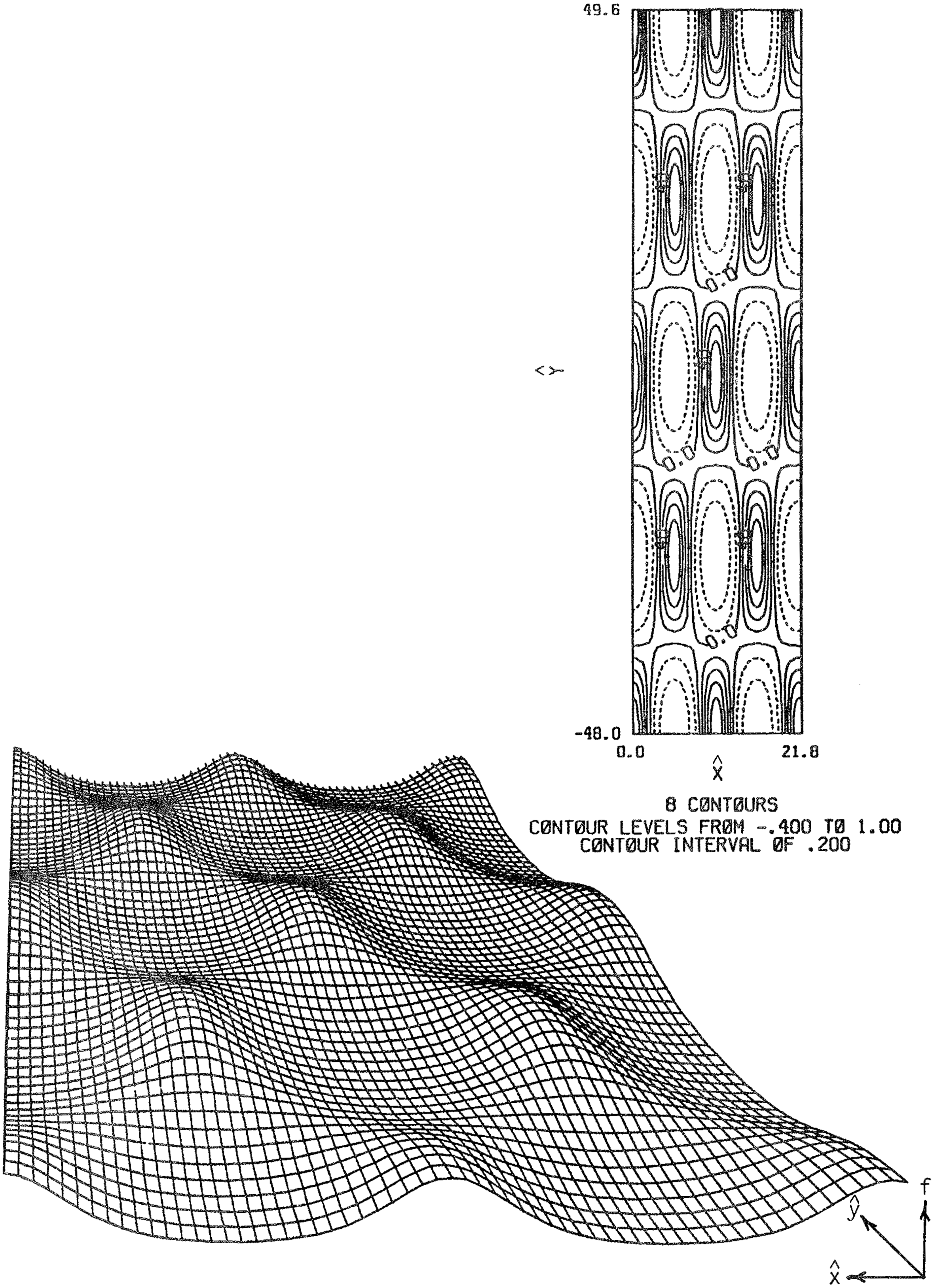

Figure B.4f Experiment CN1011

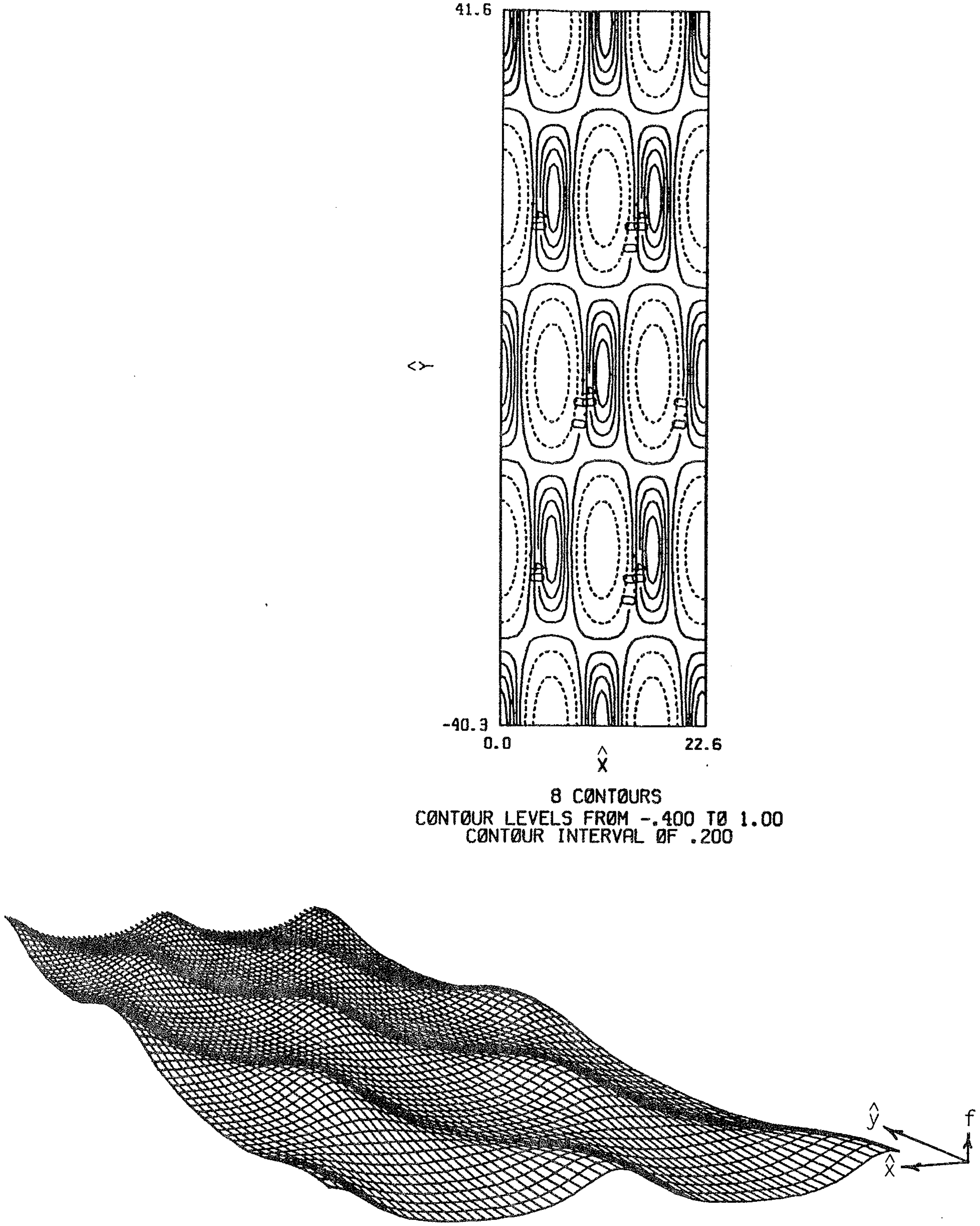

Figure B.4g Experiment CN1511

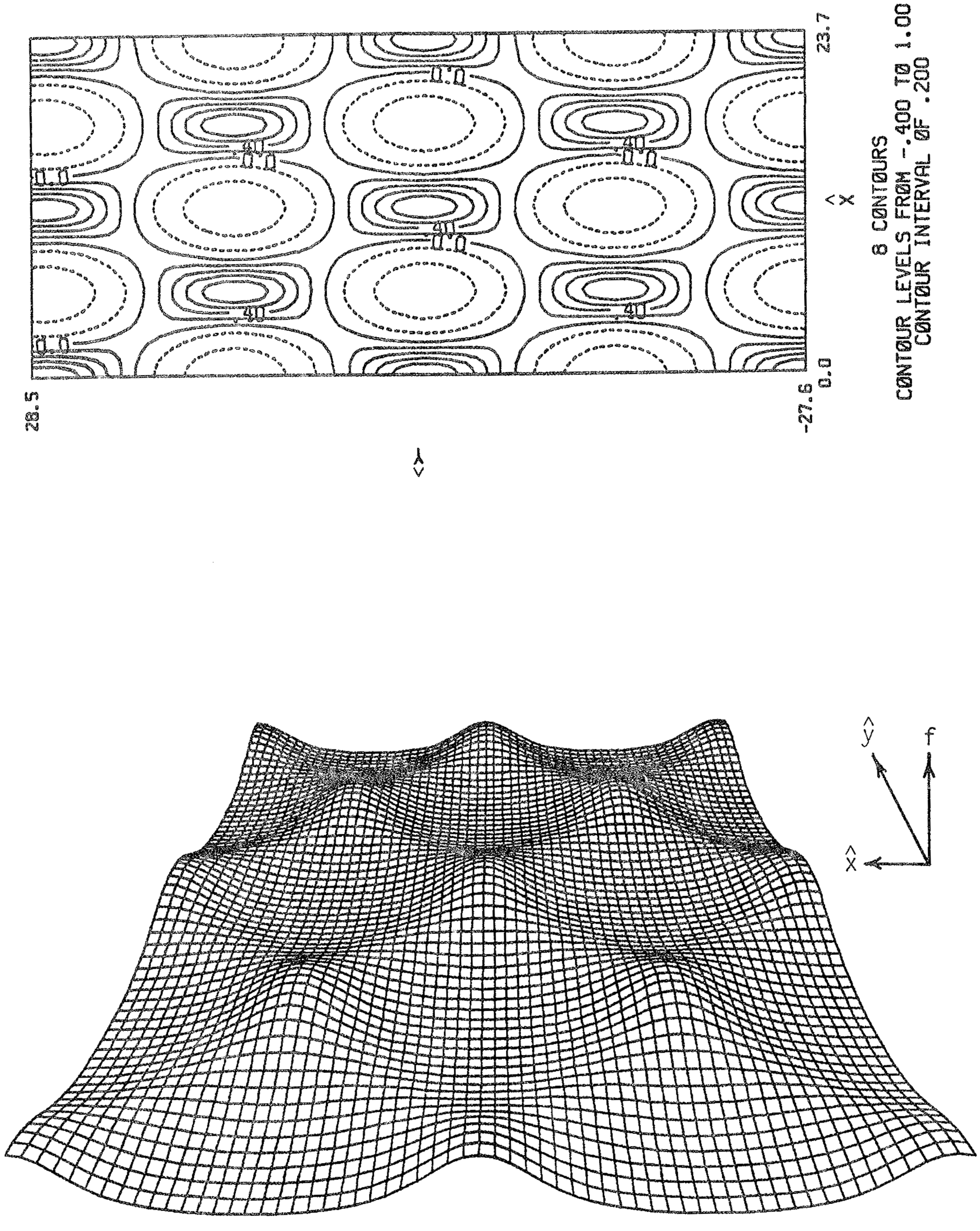

Figure B.4h Experiment CN2011

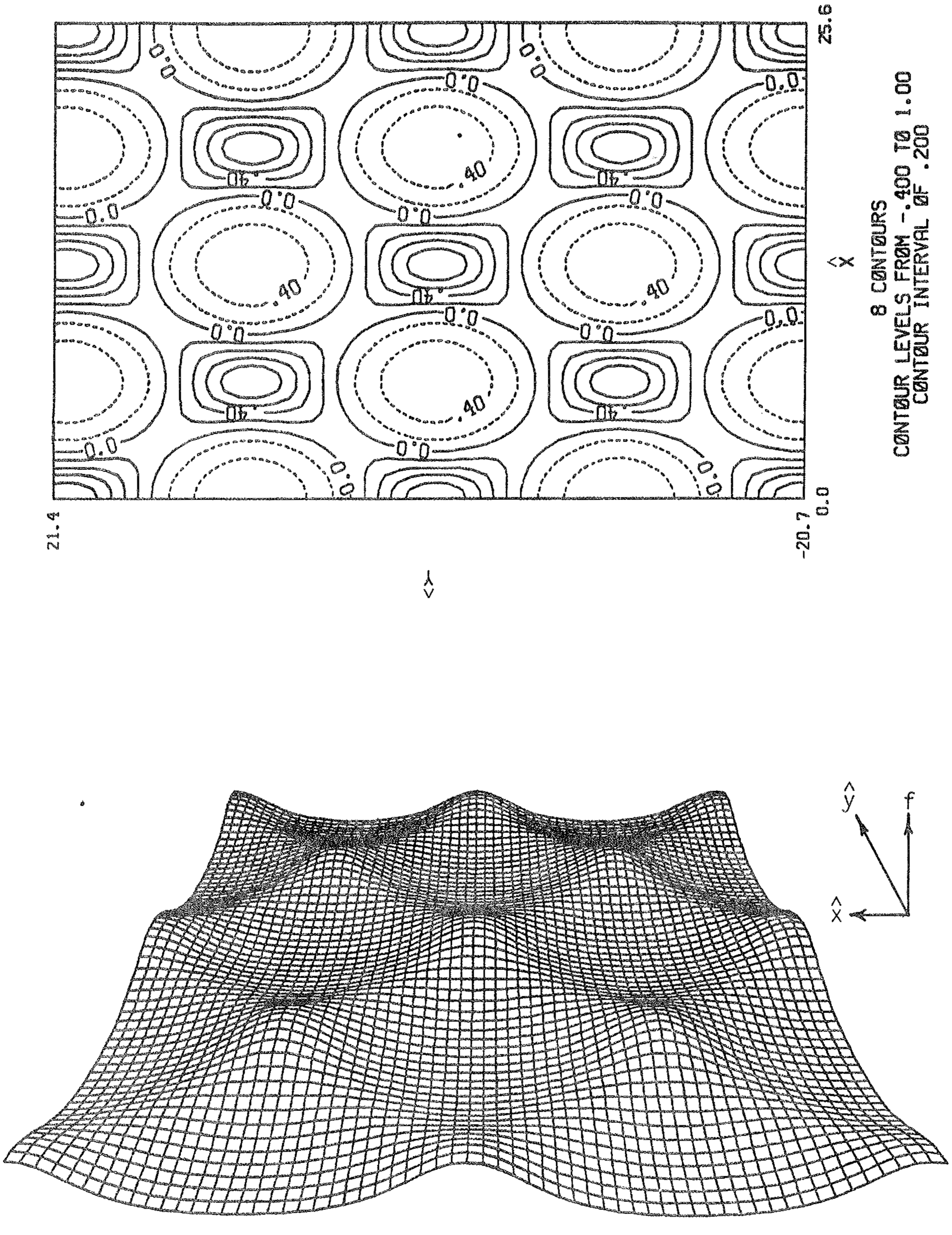

Figure B.4i Experiment CN3011

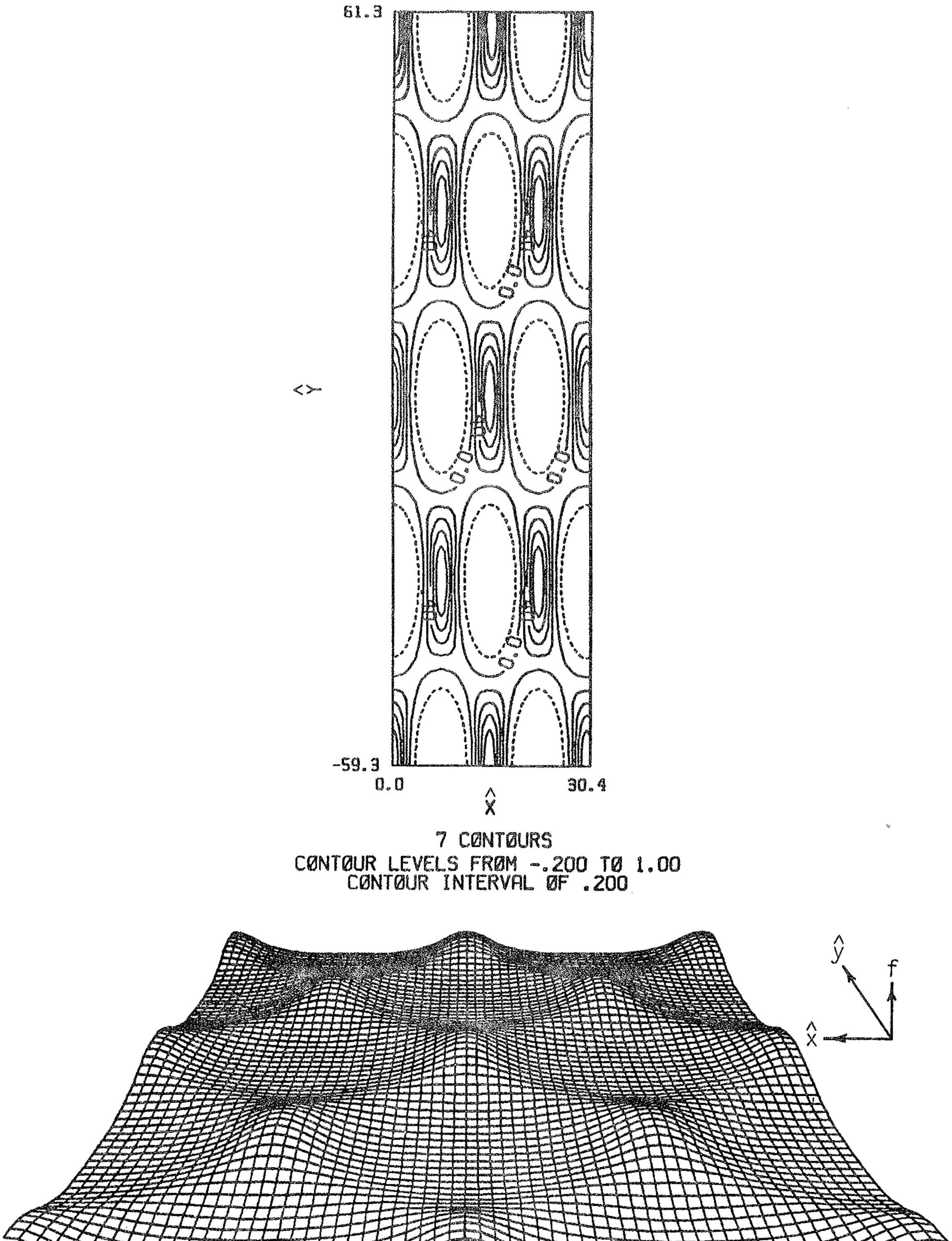

Figure B.4j Experiment CN1015

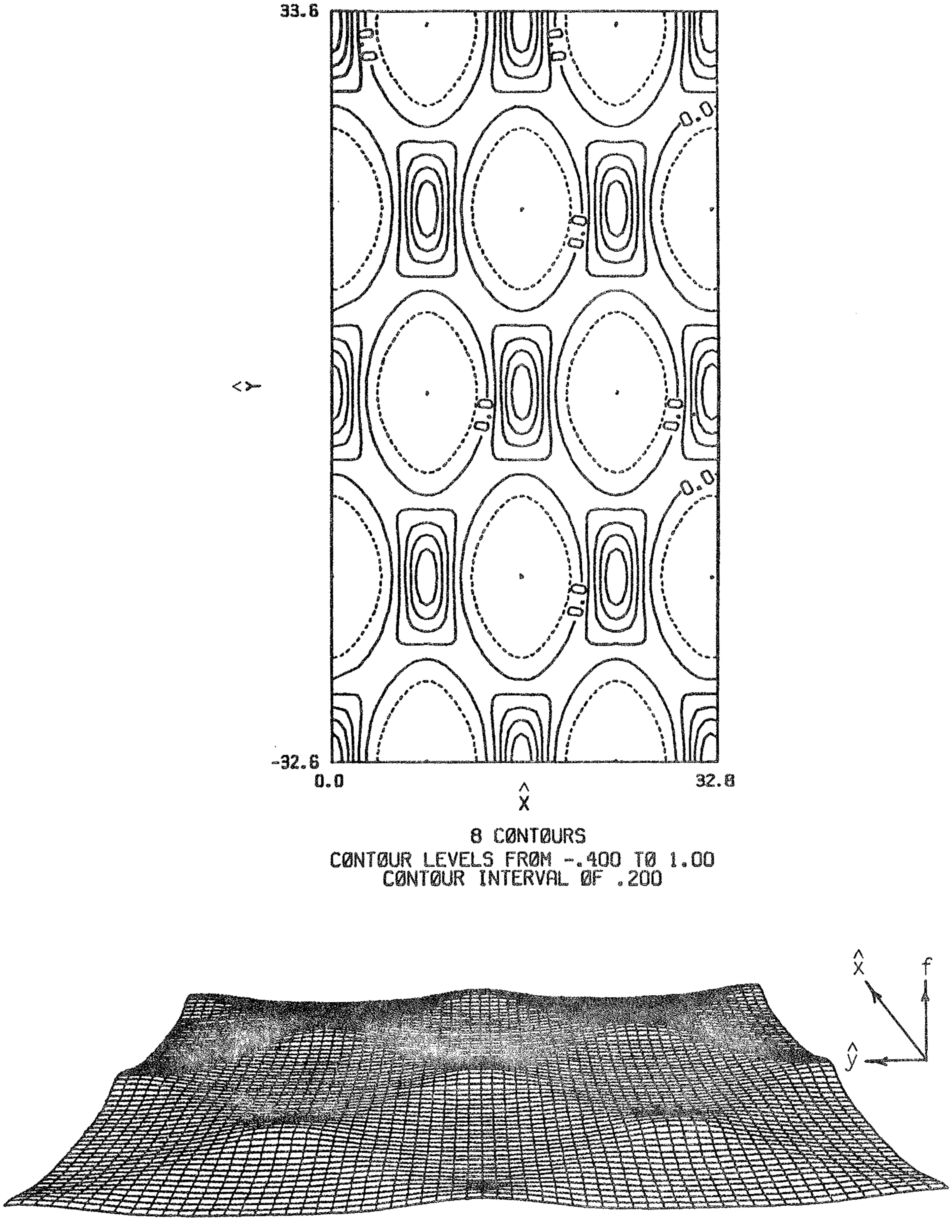

Figure B.4k Experiment CN1515

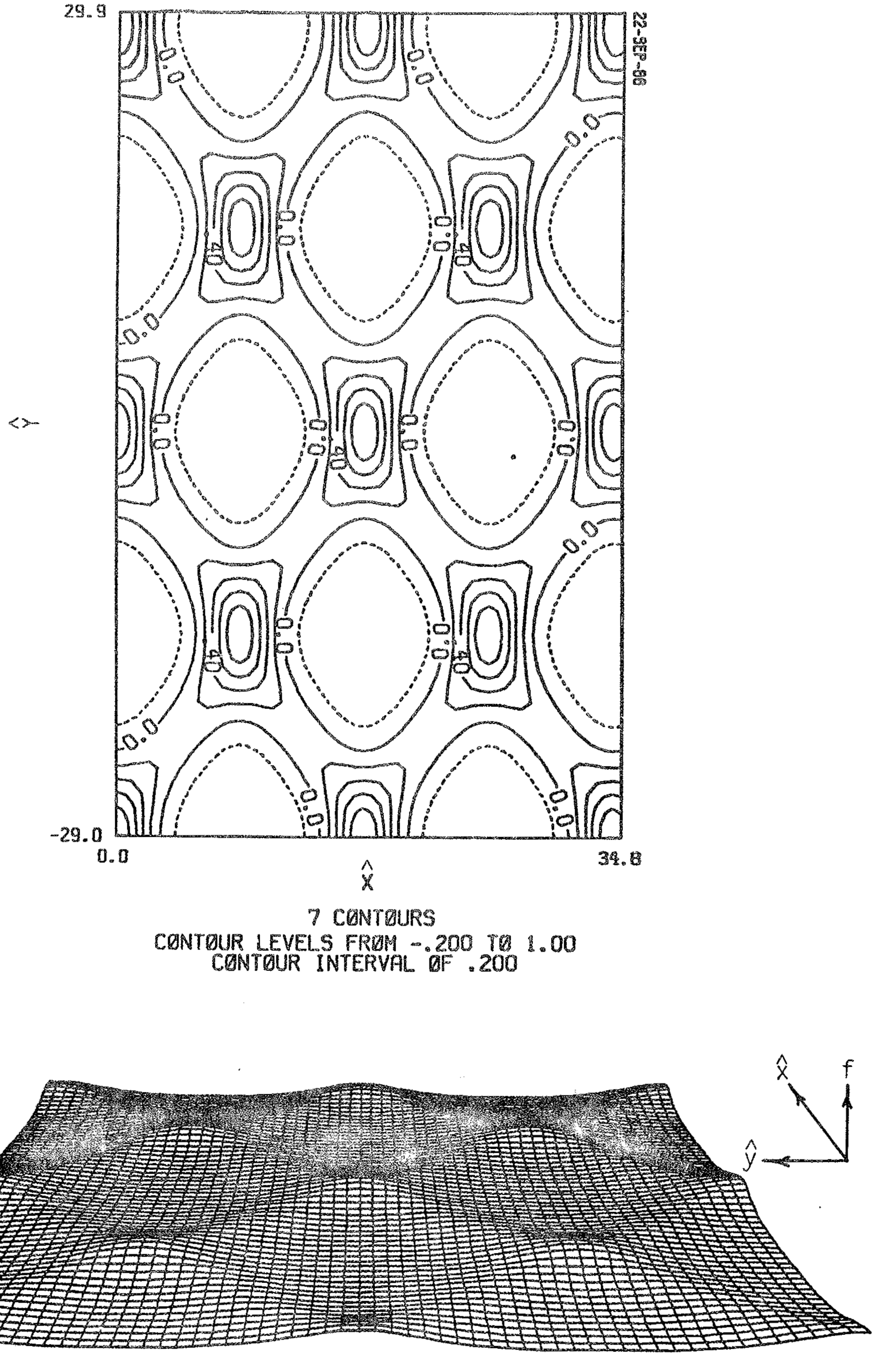

Figure B.41 Experiment CN2015

REFERENCES

Ablowitz, M.J., Kaup, D.J., Newell, A.C., and Segur, H. (1973), "Nonlinear Evolution Equations of Physical Significance," Phy. Rev. Lett., Vol 31, pp. 125-127.

_____(1974), "The Inverse Scattering Transform-Fourier Analysis for Nonlinear Problems," Stud. Appl. Math., Vol 53, pp. 249-315.

Abramowitz, M. and Stegun, I.A. (1970) "Handbook of Mathematical Functions," Applied Mathematics Series 55, National Bureau of Standards, Washington D.C.

Airy, G.B. (1845), "Tides and Waves," Encyclopedia Metropolitana, Vol 5, London.

Boussinesq, J. (1871), "Theorie de'Intumescence Liquide Appelee onde Solitarie ou de Translation se Propageant dans un Canal Rectangulaire," C.R. Acad. Sci., Vol 72, Paris.

Bryant, P.J. (1982), "Two-dimensional Periodic Permanent Waves in Shallow Water," Journal of Fluid Mechanics, Vol 115, pp. 525-532.

Chatham, C.E. (1984), "The Coastal Engineering Research Center's Portable Directional Spectral Wave Generator," Proc. of the 1984 Coastal Engineering Research Board, Vicksburg, Mississippi.

Dubrovin, B.A. (1981), "Theta Functions and Non-Linear Equations," Russian Math. Surveys, Vol 36, pp. 11-92.

Durham, D.L. and Greer, H.C. (1985) "Automated Data Aquisition and Control Systems for Hydraulic Wave Model," Proc. of the 1976 Army Numerical Analysis and Computers Conference, Army Reasarch Office (ARO) Report 76-3, Research Triangle Park, N. C.

Gardner, C.S., Greene, J.M., Kruskal, M.D., and Miura, R.M. (1967), "Method for Solving the Korteweg-deVries Equation," Phy. Rev. Lett., Vol 19, No. 19, pp. 1095-1097.

Gardner, C.S. and Morikawa, G.K. (1960), "Similarity in the Asymptotic Behavior of Collision Free Hydromagnetic Waves and Water Waves," Courant Inst. Math. Sci. Res. Rep. NYO-9082, New York University, New York.

Gel'Fand, I.M. and Levitan, B.M. (1955), "On The Determination of a Differential Equation from its Spectral Function," Amer. Math. Soc. Transl., Ser. 2, Vol 1, pp. 259-309.

Goring, D.G. (1978), "Tsunamis--The Propagation of Long Waves onto a Shelf," Report No. KH-R-38, W.M. Keck Laboratory of Hydraulics and Water Resourses, California Institute of Technology, Pasadena, California.

Hammack, J.L. (1980), (Unpublished Experiments on Nonlinear Wave Interaction), Dept. of Civil Engineering, University of California, Berkeley, California.

Hammack, J.L. (1985), (Unpublished Notes on Nonlinear Wave Theory), Dept. of Engineering Sciences, University of Florida, Gainesville, Florida.

Kadomtsev, B.B. and Petviashvili, V.I. (1970), "On the Stability of Solitary Waves in Weakly Dispersive Media," Soviet Physics Doklady, Vol 15, No 6, pp. 539-541.

Korteweg, D.J. and deVries, G. (1895), "On the Change of Form of Long Waves Advancing in a Rectangular Channel, and on a New Type of Long Stationary Waves," London, Edinburgh, and Dublin Philosophical Magazine, Series 5, Vol 39, pp. 422-443.

Krichever, I.M. (1976), "An Algebraic-Geometric Construction of the Zakharov-Shabat Equations and their Periodic Solutions," Dokl. Akad. Nauk. SSSR 227, MR54# 1298, pp. 291-294.

Kruskal, M.D. and Zabusky, N.J. (1963), Princeton Plasma Physics Laboratory Annual Report MATT-q-21, pp. 327-335, Princeton, N.J.

Lax, P.D. (1968), "Integrals of Nonlinear Equations of Evolution and Solitary Waves," Comm. Pure App. Math., Vol 7, pp. 159-193.

Madsen, O.S. and Mei, C.C. (1969), "Dispersive Long Waves of Finite Amplitude over an Uneven Bottom," Report No. 117, School of Engineering, Massachusetts Institute of Technology, Cambridge, Massachusetts.

Marchenko, V.A. (1977), "The Theory of Sturm-Liouville Operators," Naukova Dumka (in Russian), Kiev.

McKean, H.P. and van Moerbeke, P. (1975), "The Spectrum of Hill's Equation," Invent. Math., Vol 30, Mr53#936, pp. 217-274.

Melville, W.K. (1980), "On the Mach Reflection of a Solitary Wave," Journal of Fluid Mechanics, Vol 98, pp. 285-297.

Miles, J.W. (1977), "Obliquely Interacting Solitary Waves," Journal of Fluid Mechanics, Vol 79, part 1, pp. 157-169.

Milne-Thompson, L.M. (1950), "Jacobian Elliptic Function Tables," Dover Publications, Inc., New York

Outlaw, D.G. (1984), "A Portable Directional Irregular Wave Generator for Wave Basins Proceedings," Symposium on Description and Modeling of Directional Seas", Paper No. B-3, Technical University of Denmark, Lyngby.

Rayleigh, Lord (1876), "On Waves," London, Edinburg, and Dublin Philosophical Magazine, Vol 1, No. 4, pp. 257-279.

Roberts, A.J. and Schwartz, L.W. (1983), "The Calculation of Nonlinear Short-crested Gravity Waves," Physics of Fluids, Vol 29, No. 9, pp. 2388-2392.

Russell, J.S. (1844), "Report of Waves," Rep. 14th Meeting of the British Association for the Advancement of Science, John Murray, pp. 311-390 + 11 plates, London.

Segur, H. and Finkel, A. (1985), "An Analytical Model of Periodic Waves in Shallow Water," Stud. Appl. Math., Vol 73, pp. 183-220.

Stokes, G.G. (1849), "On the Theory of Oscillatory Waves," Transactions, Cambridge Philosophical Society, 8,449 (Mathematical and Physical Papers, Vol 1, p 210).

Svendsen, I.A. (1974), "Cnoidal Waves Over a Gently Sloping Bottom," Series Paper No. 6, Institute of Hydrodynamics and Hydraulic Engineering, Technical University of Denmark, Lyngby.

Turner, K.A. and Durham, D.C. (1984), "Documentation of Wave-Height and Tidal Analysis Programs for Automated Data Acquisition and Control Systems," Miscellaneous Paper HL-84-2, U.S. Army Engineer Waterways Experiment Station, Vicksburg, Mississippi.

Ursell, F. (1953), "The Long-Wave Paradox in the Theory of Gravity Waves," Proceedings, Cambridge Philosophical Society, Vol 49, pp. 775-694.

Whalin, R.W., Chatham, C.E., Durham, D.L., and Pickett, E.B. (1974), "A Case History of Los Angeles--Long Beach Harbors," A.S.C.E. Proc. International Symposium on Ocean Wave Measurement and Analysis, Copenhagen, Denmark, Vol 1., Sept 1974.

Wiegel, R.L. (1960), "A Presentation of Cnoidal Wave Theory for Practical Application," Journal of Fluid Mechanics, Vol 7. pp. 273-286.

Zakharov, V.E. and Shabat, P.B. (1972), "Exact Theory of Two-Dimensional Self-Focusing and One-Dimensional Self-Modulation of Waves in Nonlinear Media," Sov. Phys. JETP, Vol 34, pp. 62-69.